manos kaniolakis kaloudis

HIGH HARMONIC GENERATION WITH CHIRPED ULTRASHORT LASER PULSES

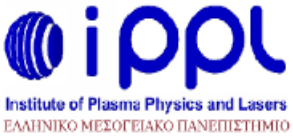

Master Program
Lasers, Plasma and Application (LaPLA)

Department of Electronic Engineering & Institute of Plasma Physics and Lasers (IPPL), Hellenic Mediterranean University (HMU)

"HIGH HARMONIC GENERATION (HHG) WITH CHIRPED ULTRASHORT LASER PULSES"

KANIOLAKIS KALOUDIS EMMANOUIL

MASTER THESIS

GRADUATION COMITEE

SUPERVISOR: Professor Nektarios Papadogiannis, HMU

MEMBERS: Professor Michalis Tatarakis, HMU

Professor Emmanouil Benis, UOI

PETHYMNO, 2021

CONTENTS

1. ABSTRACT 4

2. THEORETICAL INTRODUCTION 5

2.1 HIGH HARMONIC GENERATION 5

1.1.1 THREE STEP MODEL 6

1.1.2 PHASE MATCHING 14

1.1.3 SELPH PHASE MODULATION 17

1.2 GENERATION OF ULTRA SHORT LASER PULSES 18

1.2.1 CHIRP 19

1.2.2 CPA TECHNIQUE 21

1.2.3 AUTOCORRELATORS 24

1.4 HIGH HARMONIC GENERATION WITH CHIRPED PULSES 26

3. EXPERIMENTAL SETUP 32

4. EXPERIMENTAL RESULTS AND ANALYSIS 39

4.1 INTRODUCTION TO DATA ANALYSIS 39

4.2 ANALYSIS OF SPECTRAL SPLITING 50

4.3 DIVERGENCE OF LONG AND SHORT TRAJECTORIES 58

5. CONCLUSIONS 63

6. BIBLIOGRAPHY 64

ACKNOWLEDGEMENTS

In submitting my dissertation, I warmly thank my supervisor, Professor Nektarios Papadogiannis, for his substantial and restless guidance in undertaking this dissertation. His many years of work in the field of High Harmonic generation and his extensive experience and knowledge of the experimental processes involved, as well as his deep understanding of the physical principles in play, have been a valuable guide for me in my endeavor as a young researcher to understand the fundamentals of the femtosecond physics and XUV coherent radiation. His guidance allowed me to gain deep understanding and great experience in the execution of state-of-the-art experiments. I would like also to thank Professor Emmanouil Bennis, whose deep physical intuition and his important experimental and structural remarks were a key factor in the successful completion of my dissertation. Moreover, I would also like to thank Professor Michalis Tatarakis, as his experience in performing innovative physical experiments and writing state of the art dissertations was essential to my research effort. In addition, I thank the PhD candidate Mr. Stelios Petrakis whose daily guidance in performing the experiments and their subsequent analysis was very important to me, in terms of gaining experimental technical knowledge and experience. Finally, I would like to thank my other colleagues, especially Ioannis Tazes and Sophocles Nikolaou who tirelessly accompanied me in my scientific research. In closing, I thank my parents for their unwavering support and patience in this endeavor.

Emmanouil Kaniolakis Kaloudis

Rethymno 2021

1. ABSTRACT

In this master thesis we experimentally studied the effects of the induction of a linear chirp function into the electric field of a high-power laser. The scope of this study was to explore the different behavior of high harmonic radiation generated by the chirped pulses of the high-power laser. The experiments were conducted in the IPPL facility of the Mediterranean university of Crete. The experimental set up was centered around the probe beam of a high powered Ti:sa laser system with 0.9mJ peak energy, and allowed us to achieve pulse intensities of 10^{14} W/cm^2. The pulses utilized in the experiments were of the femtosecond order. In these experiments we tried to optimize the different parameters affecting the efficiency of the high harmonic generation, such as the iris diameter and the gas pressure. By this optimization we managed to isolate the chirp parameter of the laser pulse and focus on its control. Furthermore, a comprehensive experimental work was done in order to determine the effects of the chirped pulses on the generation of high harmonic radiation, this enabled us to study the mechanisms by which the chirp influences the behavior of high harmonic radiation. Consequently, we were able to observe the harmonic splitting, as well as the different divergence of the short and long trajectory, due to the interplay of the propagation effects and the single atom response. So, by tuning the chirp parameter, we were able to select a specific trajectory by controlling its splitting patterns and divergence. This selection is of the outmost importance, because it allows us to select the short trajectory and use it for various applications such as nano-imaging.

This thesis is structured as: in the first chapter a comprehensive presentation of the theoretical mechanisms behind the high harmonic generation, the chirp parameter and the various phenomena involved, is done. In the second chapter, the experimental set up used is presented. In the final chapter a detailed analysis of the collected data is presented.

1. THEORETICAL INTRODUCTION

1.1 HIGH HARMONIC GENERATION

The nonlinear optical process of high harmonic generation is one of the major topics of modern multiphoton physics. It is a technique for producing spatially and temporally coherent extreme ultraviolet or vacuum ultraviolet radiation, as well as short light pulses in the attoseconds regime. High harmonic radiation have a number of interesting properties, such as being a tunable table-top source of XUV/soft X-ray radiation, which is synchronized with the driving laser field and is produced with the same repetition rate.[1]

High harmonic generation occurs, when an intense laser pulse is focused into a noble gas or solid target, inducing a time dependent dipole moment to the atoms. [2] Then, the nonlinear atomic response leads to the emission of coherent radiation at frequencies that are multiples of the laser frequency. Thus, high harmonic generation is always a constant interplay between the single atom response to an electromagnetic field (distorted by its propagation effects) and the high harmonic field, which is affected by absorption phenomena and the phase matching conditions.

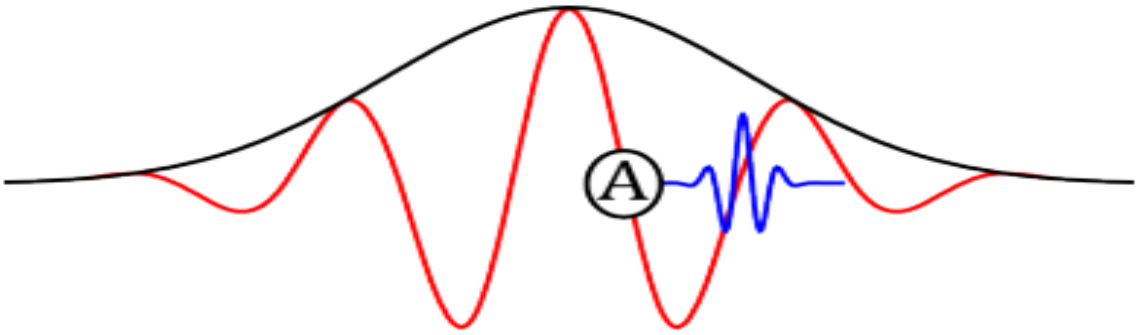

Figure 1: A phenomenological picture of high harmonic generation. An atom under the influence of a sufficiently strong electric field emites radiation with higher frequencies. The red line represents the electric field and the blue line the emitted radiation [1]

In order to generate high harmonic radiation, one should utilize low frequency ultrafast lasers (e.g. Ti: sapphire lasers or Nd: glass lasers or Erbium lasers) with laser pulse intensities such as those with corresponding electric field amplitudes comparable to the atomic electric field amplitude. In the latter case the generated high harmonic spectrum has a very characteristic and universal shape. [3] High harmonic generation strongly depends on the driving electromagnetic laser field and as result, the emitted harmonics have similar temporal and spatial coherence properties.

Electric fields of such high intensity are able to strongly excite atoms and detach electrons of them, by a quantum mechanical process known as tunneling ionization. Those electrons are accelerated in the continuum under the influence of the laser electric field, and by its sign reversal, have a significant propability to re-attach to the parent atom emitting radiation. This process is called “the three-step model” and is described in more detail in the next chapter. [3]

2.1.1 THREE STEP MODEL

The high harmonic spectra obtained from the experiments all have a standard shape, which consists of an initial high intensity part, which experience a gradual intensity fall, followed by an extended plateau region and finally a sharp cut off region.

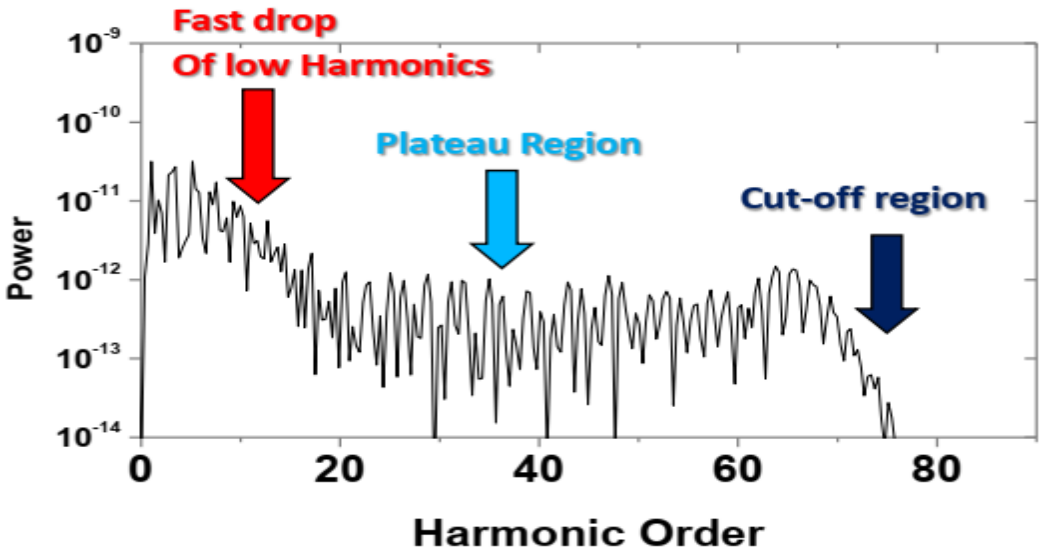

Figure 2: Typical high harmonic spectrum of the first 75 harmonic order, where the sharp drop of the power of the harmonic order from the low harmonics to the plateau region is shown. (Picture taken from N. Papadogiannis lectures on laser matter interaction, Msc, department of electronic engineering H.M.U.).

The most important phenomenon implicated in the generation of high harmonics are the process of ionization, which leads to the unbounding of the electron from the parent atom.

There are three regimes of ionization of an atom by an optical electromagnetic field. We consider here only electromagnetic fields of frequency ω such that $\hbar\omega$ < Ip therefore photoionization by a single photon is impossible. [4]

The first process of ionization is the multiphoton ionization, in which several photons of energy below the ionization threshold may actually combine their energies to ionize an atom. This probability decreases rapidly with the number of photons required. This is the dominant regime for weak electromagnetic fields, which correspond to large Keldysh parameter (eq.1). It is characterized by a power law dependence of the ionization rate on the laser intensity, where the exponential is the minimal number of photons required for ionization (Fig. 3). This regime is of less importance to HHG. The multiphoton regime takes place when the laser electric field is E<<1 in atomic units and U_p <<I_p. [3]

$$\gamma = \left(\frac{2I_p}{U}\right)^{\frac{1}{2}} > 1 \qquad (1)$$

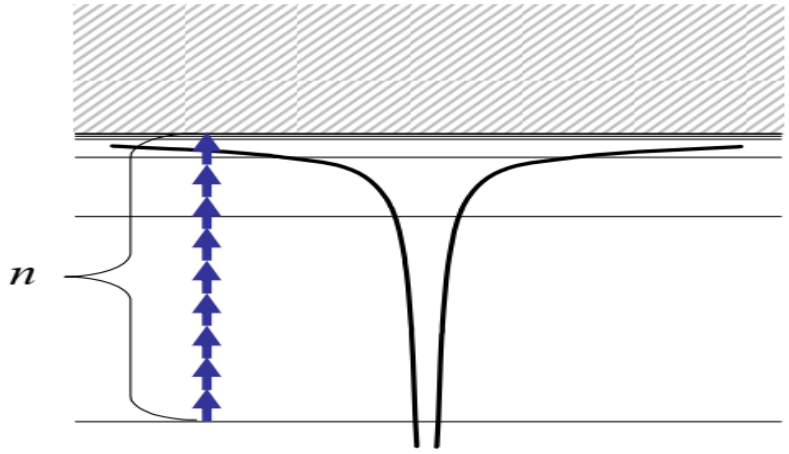

Figure 3: Multiphoton ionization process, where n is the number of absorbed photons, the black line represents the atomic potential well, the horizontal lines represent the excited states. [3]

Tunneling is the dominant regime when $U_p > I_p$ with the Keldysh parameter being $\gamma < 1$, but E is small enough such that the barrier-suppression regime is not yet reached. In this regime the electron is released in the continuum through this tunneling process, which is when electrons in an atomic potential well pass through the potential barrier and escape from the atom. In an intense electric field, the potential barrier of an atom (molecule) is distorted drastically. Therefore, as the length of the barrier that electrons have to pass decreases, the electrons can escape from the atom's potential more easily. Tunnelling Ionization is a quantum mechanical phenomenon, since in the classical picture an electron does not have sufficient energy to overcome the potential barrier of the atom and therefore ionization is forbidden. This regime is characterized by an exponential dependence of the ionization rate on the instantaneous electric field. [3]

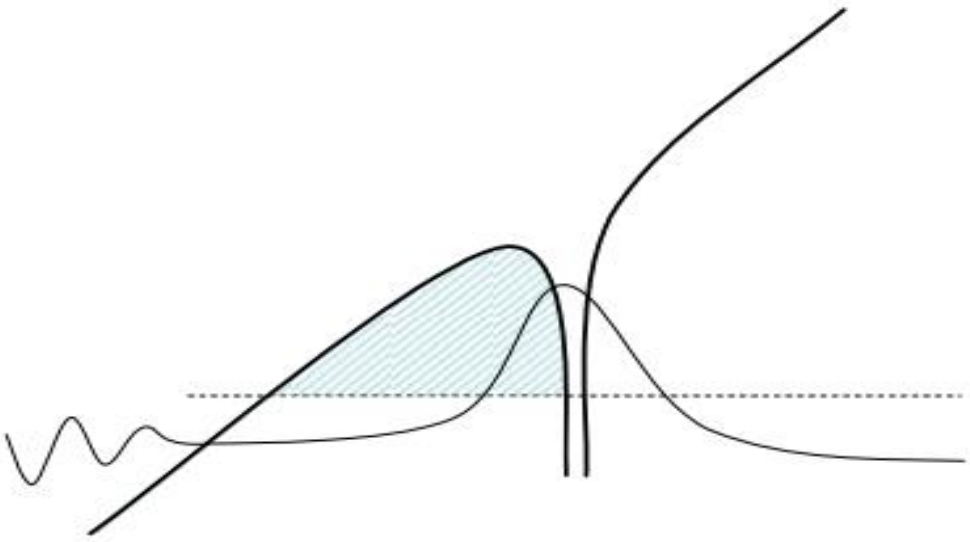

Figure 4: Ionization by tunneling. The black line represents the atomic potential and the red line represents the electric field potential. The shaded area is the barrier, the classically forbidden region. The rate of tunnel ionization is exponential in the area under the barrier [3].

Barrier-suppression regime is reached when the field is strong enough, such that the there is no energy barrier separating the electron from the free space. The barrier suppression regime is characterized by a nearly linear dependence of the ionization rate on the incident electric field. [3] this over the barrier ionization process plays a significant role in HHG.

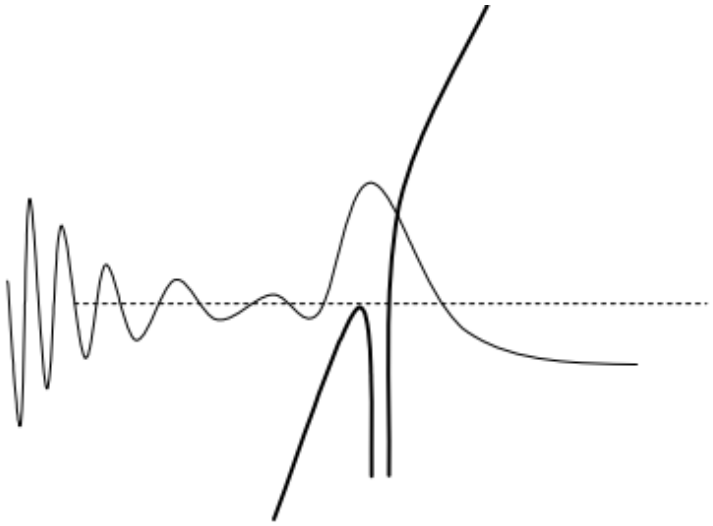

Figure 5*:* Ionization in the barrier-suppression regime, where the black line represents the atomic potential and the red line represents the electric field potential [3]

Finally, since tunnel ionization is the most important process of electron excitation at these laser intensities, meaning it has the highest propability amplitude, a more detailed analysis is appropriate. The most important factor to be calculated is the expression for the probability of tunnel ionization, in an alternating field, of a complex atom that is in an arbitrary state. First, let us set some approximations that allows for analytical expressions to be obtained: [7]

a) In tunneling ionization only, the initial and the final state are significant, while all the intermediate states can be neglected.

b) When the electromagnetic field strength is lower than that of the atomic field, we may use the quasi classical approximation.

c) The results for an alternating electromagnetic field are easily obtained from those for a constant field by substituting *E*- *E* cos***ωt*** and integrating over the period T of the field.

Assuming that the external electromagnetic field is linearly polarized, the probability of ionization per unit time from a state with energy E, orbital quantum number I, and its projection m, is described by the equations: [7]

$$w = C_{nl}^2 \left(\frac{3E}{\pi E_0}\right)^{\frac{1}{2}} E \frac{(2l+1)(l+|m|)!}{2^{|m|}(|m|)!(l-|m|)!} \left(\frac{2E_0}{E}\right)^{2n^*-|m|-1} \times e^{\left(-\frac{2E_0}{3E}\right)} \quad (2)$$

$$n^* = Z(2E)^{-1/2} \quad (3)$$

$$E_0 = (2E) \quad (4)$$

$$C_{nl} = \left(\frac{2e}{n^*}\right)^{n^*} \left(\frac{1}{(2\pi n^*)^2}\right) \quad (5)$$

The quantity C_{nl} in (eq.2) is determined for arbitrary states of the hydrogen atom from numerical calculations. [7]

Z is the charge of the atomic residue. We use the atomic system of units, *fi* = *m*, = *e* = 1.

It should be noted that the probability of detachment of an electron with magnetic quantum number *m* = 0 exceeds substantially the probability of detachment of an electron with *m* = 1. [7]

In the case of an arbitrary quantum number 1 and for *n #n** we must use the effective value *I** of the orbital number. [7]

So, for an arbitrary orbital quantum number the propability of tunnel ionization is given by the expression (6), where *Z* is the charge of the atomic residue: [7]

$$w = \left(\frac{3}{\pi^3}\right)^{\frac{1}{2}} \frac{(2l+1)(l+|m|)!}{(|m|)!(l-|m|)!} \times \left(\frac{e}{(n^{*2}-l^{*2})^{\frac{1}{2}}}\right)^{|m|+\frac{1}{2}} \left(\frac{n^*+l^*}{n^*-l^*}\right)^{l+\frac{1}{2}} \times \frac{Z^2}{n^{*3}} \left(\frac{4eZ^2}{E(n^{*3}(n^{*2}-l^{*2})^{\frac{1}{2}}}\right)^{2n^*-|m|-1/2} e^{-\left(\frac{2Z^3}{3En^{*4}}\right)} \quad (6)$$

Where l is the orbital quantum number, m is the magnetic quantum number and E is the amplitude of the electromagnetic field.

Since we were able to describe the basic ionization process, which allows the emition of the electron from a parent atom, we can discuss the semi classical model which allows the generation of high harmonics.

The semi-classical three step model, is used to describe the generation of high harmonics and states, that the process of generating high-order harmonic radiation by a single external atomic electron can be divided into three distinct steps:

1. Initially the bound electron is emitted via the tunneling ionization process by the exciting laser electric field and appears with zero velocity in the continuum, from the parent ion.
2. The electron is then accelerated by the laser electromagnetic field in the continuum, which exerts a classical force on it.
3. A scattering process, when the recombination occurs with the parent atom, creates an oscillating electric dipole that emits radiation.

It is necessary to consider the electron in a quantum-mechanical context and distinguish between several different regimes of ionization, depending on how strong is the electromagnetic field compared to the atomic potential static field. It is safely assumed that the electron can appear in the continuum at several different times with respect to the external electromagnetic field and that the probability of the various ionization processes can be scaled in a strongly nonlinear way with the intensity. Once it is subjected to the external electric field, the motion of the electron can be described classically by the forces acting on it due to the classical electromagnetic field of the laser.

The next step of the model, takes place after the ejection of the excited electron in the continuum. Considering the correspondence principle, which states that at high energies quantum

mechanics should resemble classical mechanics. Indeed, it turns out that the propagation of the ejected electron can be very well described classically. Since the Coulomb force exerted on the electron by the ion is negligible compared to the laser field during most of the electron propagation, the motion of the electron is well described by a free electron acceleration in the presence of the classical electromagnetic field of the laser pulse. Since we expect that the electrons do not reach relativistic speeds, we can neglect the Lorentz Force. It also turns out that right after the tunneling, the velocity of the electron vanishes, and therefore the electron starts with zero velocity in the external field. This holds true because the electron is a quantum particle. So it is released at all possible times t_0 simultaneously, so each moment there is a real probability amplitude for the electron to be released, depending on the electric field at that moment. So the quasi static approximation can be applied (quasi static approximation refers to differential equations that keep a static form, that is they do not involve time derivatives even if some quantities are allowed to vary slowly with time). [3] [6]

$$\ddot{x}(t) = E_0 \cos(\omega t) \tag{7}$$

$$\dot{x}(t) = \frac{E_0 \sin(\omega t)}{\omega} - \frac{E_0}{\omega} \sin(\omega t_0) \tag{8}$$

$$x(t) = -\frac{E_0 \cos(\omega t)}{\omega^2} - (t - t_0)\frac{E_0 \sin(\omega t_o)}{\omega} + \frac{E_0}{\omega^2} \cos(\omega t_0) \tag{9}$$

Eq. (7,8,9) are deduced by solving the newtons classical equations of motion of an electron under the influence of a classical electromagnetic force.

By solving this set of equation, we can calculate the trajectories of the electron, as well as its kinetic energy (it must be equal to Up/2), here t_0 is the time the electron is born in the continuum. [5]

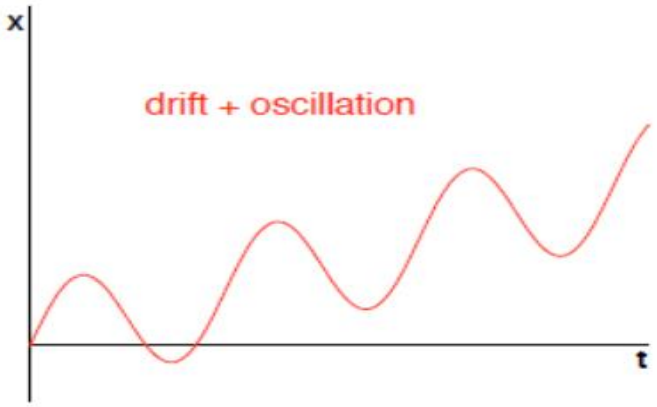

Figure 6: Typical electron trajectory in the continuum, under the influence of a classical AC laser electric field, the y axis noted with X represents the distance between the electron and the atomic core and x axis denoted with t, represents time. (Picture taken from N. Papadogiannis lectures on laser matter interaction, Msc, department of electronic engineering H.M.U.).

Also, it should be mentioned that the high harmonic radiation in gases is emitted as odd multiples of the laser electromagnetic field frequency. This is due to the inversion symmetry of the

gas atoms (meaning that they are spherically symmetric) and holds true only for atoms of such symmetry. Different geometry may lead to even harmonics, as it is in HHG in solids. [5]

This postulate is deduced by some trivial symmetry properties using the polarization function. Polarization tensor refers to the displacement of the electron cloud from the equilibrium position by the vector of the electromagnetic field of the laser. In nonlinear optics the polarization is often written in a power expansion of the electric field (eq.11). In a spherically symmetrical system, we can require *P* (*E*) = -*P* (-*E*)**,** meaning that the electron cloud displacement is independent of the direction of the electric field (up to a sign change). This implies automatically that for all *m* belonging *to* N, χ^{2m} has to be zero. If we take an initial electrical field of the form (eq.9) it follows directly, that the absence of even order χ also implies an absence of even harmonics. Therefore, in the overall spectrum that was predicted in the previous section no even harmonic peaks will be seen as long as a spherical symmetry is maintained. [1]

$$\boldsymbol{P(t)} = \varepsilon_0[x^{(1)} \otimes \boldsymbol{E(t)} + x^{(2)} \otimes \boldsymbol{E(t)} \otimes \boldsymbol{E(t)} + \dots] \tag{10}$$

$$E(t) = E_0 e^{(i\omega t)} \tag{11}$$

Under certain circumstances the electron will then recombine with the atom, after the field changes sign, emitting its kinetic energy (accumulated by its propagation in the continuum), plus the binding energy in the form of electromagnetic radiation. It is shown qualitevly that the maximal photon energy of the emitted radiation cannot exceed the electron energy at impact plus the ionization potential of the atom, due to the necessity the conservation of energy to be valid. [3] [1]

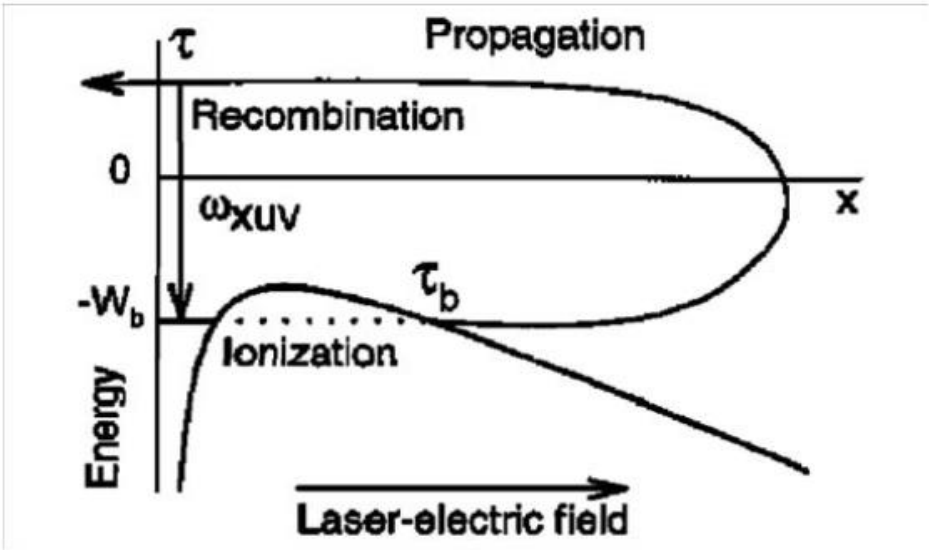

Figure 7: The three-step model, describes how the electron unbounds from the atomic potential through tunnel ionization and the after changing direction, under the influence of the laser electromagnetic field, recombines with the parent atom emitting photons. The t axis represents time, x axis space and W_b is the ionization energy [3]

Equation (12) yields the cut off energy of the harmonic radiation, which is the maximum achievable energy of the harmonic radiation photons. It is the sum of the ionization potential of the

atom (I_p), which corresponds to the binding energy of the recombining electron and a quantity (U_p) known as ponderomotive energy, that corresponds to the kinetic energy acquired in the continuum by the electron. [3] [1]

$$E_{harmonic} = I_p + 3.17U_p \tag{12}$$

The energy that is acquired from the electron in the continuum is easily calculated, considering a freely moving electron in a classical electromagnetic field with amplitude E and angular frequency ω.

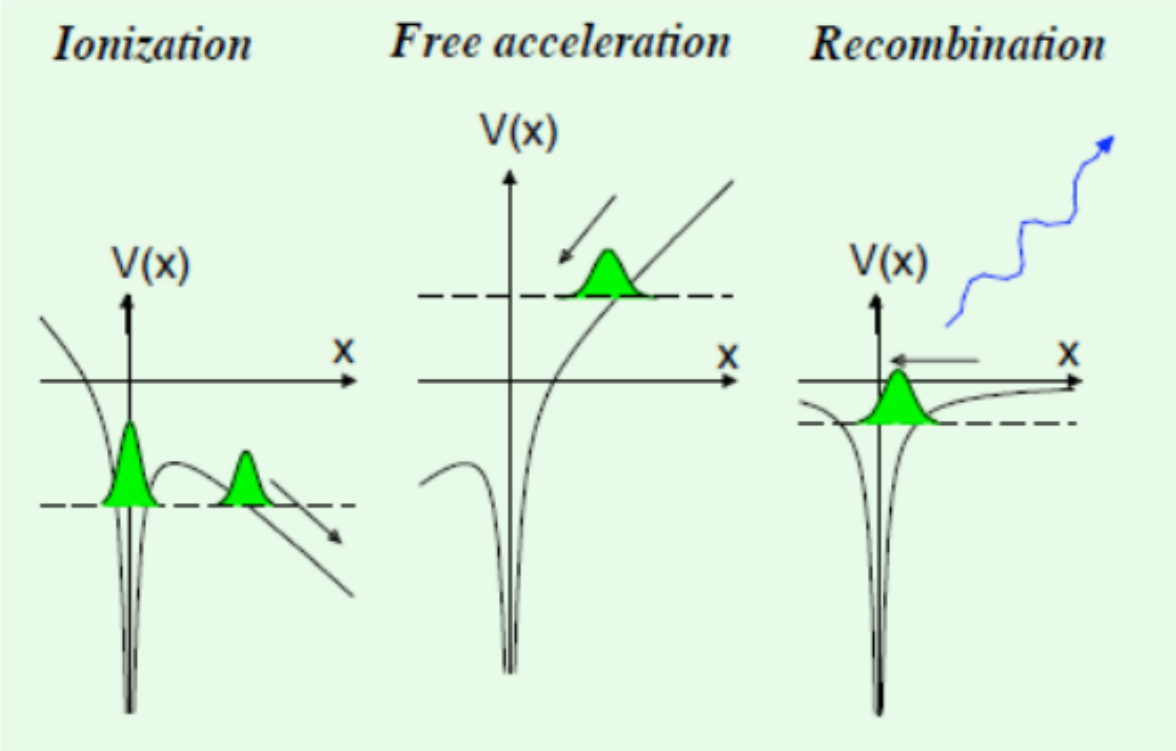

Figure 8: The three step model. Where, the green shape represents the laser pulse, the continuous line the atomic potential and the blue arrow is the harmonic radiation We observe the ejection of the electron, its classical propagation in the continuum and the final recombination, which lead to the emission of a high harmonic photons. (Picture taken from N. Papadogiannis lectures on laser matter interaction, Msc, department of electronic engineering H.M.U.)

The ponderomotive energy is given by the following equation, where E is the driving electric field, n is the electron mass, q the electron charge and ω is the laser frequency: [3]

$$U_p = (\frac{qE}{2\omega m})^2 \tag{13}$$

The parameter 3.17 which appears in the equation (13) is not easily calculated, and even though we may obtain an approximate calculation through classical mechanics a deeper quantum

mechanical explanation is required, which was done by Lewestein et al. In their publication they solved the time dependent Schrodinger equation. They consider an atom (or an ion) in a single-electron approximation under the influence of the laser electromagnetic field of the form E cos (ωt), of linear polarization in the x direction. In the length gauge, the Schrodinger equation takes the form: [4]

$$i\frac{\partial}{\partial t}\left|\Psi(x,t)>=\left[-\frac{1}{2}\nabla^2+V(x)-Ecos(\omega t)x\right]\right|\Psi(x,t)> \quad (14)$$

The difference between sine and cosine pulse can be expressed by their different behavior under time reversal t to -t, where the field of a cosine pulse remains invariant, while the field of a sine pulse changes sign. The cosine pulse therefore has a preferred orientation of the electric field, which is the orientation of the maximal field peak, which breaks the symmetry of field orientations usually assumed in optics. The violation of symmetry has a striking manifestation in the high harmonic spectrum of a cosine pulse: the rule that harmonic peaks appear only at odd multiples of the fundamental frequency may be violated. [4]

Initially the system is in the bound state, which in general has a spherical symmetry. Equation (14) is solved under the assumptions, that the contribution to the evolution of the system of all bound states except the ground state can be neglected. The depletion of the ground state can be neglected (Up <Usat). In the continuum, the electron can be treated as a free particle moving into the electric field with no effect of V(x). Therefore, calculating the x component of the dipole moment, which is the only one that survives and by taking the appropriate component of the Fourier transform we get (eq. 15). Those assumptions are valid for Keldysh parameter smaller than 1, very high laser intensities and we have no intermediate resonances, hence is valid only for tunnel ionization and over the barrier ionization processes. Having a Keldysh parameter smaller than one implies that the electron appears in the continuum under a strong electric field hence the influence of the V(x) is negligible. [4]

$$x_{2k+1}=i\sum_{M=0}^{\infty}\int_0^{\infty}\mathrm{d}\tau\,\left(\frac{\pi}{\varepsilon+\frac{i\tau}{2}}\right)^{\frac{3}{2}}\;\mathrm{e}^{-\mathrm{i}F_0(\tau)}\mathrm{b}_{\mathrm{k}-\mathrm{M}(\tau)}\mathrm{J}_{\mathrm{M}}(\mathrm{U}_{\mathrm{p}}\mathrm{C}(\tau))(\mathrm{i}^{\mathrm{M}})\mathrm{e}^{\mathrm{i}\mathrm{M}\tau} \quad (15)$$

The integration over eq.15 is complicated and can be performed either numerically or by using a saddle-point method. But we can deduce a lot of information by the $C(\tau)$ function, which determines the variation of action (eq.16), the integral of which yields the kinetic energy of the electron. Therefore, the maxima of $C(\tau)$ correspond to the maxima of the kinetic energy. T. he first maximum appears at around 3.17 further maxima are invalidated because the Bessel functions becomes very small [4]

The following equation yields the semi classical action S, as a function of the ponderomotive energy, laser intensity and time.

$$\mathrm{S}_{\mathrm{st}}(\mathrm{t},\tau)=\frac{1}{2}\int_{\mathrm{t}-\tau}^{\mathrm{t}}\mathrm{d}\mathrm{t}''(\mathrm{p}_{\mathrm{st}}-\mathrm{A}(\mathrm{t}''))^2=\left(\mathrm{I}_{\mathrm{p}}+\mathrm{U}_{\mathrm{p}}\right)\tau-\frac{2}{\tau}\mathrm{U}_{\mathrm{p}}[1-\cos(\tau)]-\mathrm{U}_{\mathrm{p}}\mathrm{C}(\tau)\times\cos(2\mathrm{t}-\tau) \quad (16)$$

Determination of the semi-classical action allows us to calculate the different propability amplitudes of the HHG process.

2.1.2 PHASE MATCHING

As we have already described in high harmonic generation, the output of a tabletop femtosecond laser is up converted into the extreme-UV and soft X-ray regions of the spectrum, via the three-step model process. In this highly nonlinear frequency up conversion process, the energy scale, time-scale and spatial scale all represent physical extremes for a controlled, fully coherent process. However, in experiments and in most applications of high harmonic sources, relatively low-energy photons were utilized. This is because, although each atom emits harmonics over a broad range of photon energies, to generate a bright output beam, the emission of photons from a large number of atoms over an extended region of the nonlinear medium must add in phase. This phase matching condition is achieved when the driving laser pulse and the generated high harmonic radiation propagate at the same phase velocity in the nonlinear medium. The process of phase matching is described via the coherent length (equation 17) which relates the phase difference of the high harmonic radiation and the driving field, with the length in which those phases add, thus generating coherent radiation. [13]

$$L_{coh}=\frac{\pi}{\Delta\kappa_q} \tag{17}$$

$$\Delta\kappa_q= qk(\omega) - k(q\omega) = 0 \tag{18}$$

The high harmonic output is given by the relation (19) which relates the intensity with the coherent length and the phase difference: [9]

$$I_q \propto L^2 \frac{(\sin(\frac{L\Delta kq}{2}))^2}{(\frac{L\Delta kq}{2})^2} \tag{19}$$

The phase mismatch between the fundamental laser and the harmonic radiation is given by the equation (13), which relates the geometrical contributions as well as the plasma and neutral atoms contributions to the dispersion: [13] [16]

$$\Delta\kappa_q=\Delta\kappa_{q,geo} + \Delta\kappa_{q,plasma} + \Delta\kappa_{q,neutral} - \Delta\kappa_{q,dip} \tag{20}$$

The geometric contribution to the dispersion is described by the Gouy phase, which is a phase shift a Gaussian beam acquires along its propagation path, equation (21) yields the geometric phase shift and equation (22) the gouy phase:

$$\Delta\kappa_{q,geo} = q\kappa_{geo}(\omega) - \kappa_{geo}(q\omega) \tag{21}$$

$$\varphi_g(z) = -arctan\frac{Z}{Z_R} \tag{22}$$

Where z_R is the Rayleigh length and $z = 0$ corresponds to the position of the beam waist. In the literature, this formula is also found with a positive sign, but in any case, the phase shift of a Gaussian beam is reduced (rather than increased) with respect to that of a plane wave. This results in a slightly increased distance between wave fronts, compared with the wavelength as defined for a plane wave of the same frequency. This also means that the phase fronts have to propagate somewhat faster, leading to an effectively increased local phase velocity.[10]

$$\kappa_{\mathrm{geo}}(\mathrm{z}) = \frac{\mathrm{d}\varphi_{\mathrm{Gouy\ (z)}}}{\mathrm{dz}} = \frac{\mathrm{dtan}^{-1}\left(\frac{\mathrm{z}}{\mathrm{z_R}}\right)}{\mathrm{dz}} \tag{23}$$

Substituting equation (23) to equation (21) we yield the final expression for the geometrical contribution the following equation:

$$\Delta\kappa_{q,geo} = \frac{q-1}{z_R\ [1+\left(\frac{z}{z_R}\right)^2]} \tag{24}$$

The second term in the phase difference vector (eq. 20), is due to the plasma dispersion. When a high-intensity laser field interacts with a medium, partial ionization of atoms and emission of electrons is observed. Most of the electrons do not reconnect to the nuclei. The plasma that is created consists of free electrons and the positively charged nuclei. The contribution of the plasma to the total dispersion is almost exclusively to the electrons, because of their much smaller mass compared to that of the nuclei. Those electrons absorb incoming light and make group oscillations, which result in a change in the refractive index. The induced refractive index is given by the formula: [14] where ω_p is the plasma frequency and ω the laser frequency.

$$n_p = \sqrt{1 - \frac{{\omega_p}^2}{\omega^2}} \tag{25}$$

And the plasma dispersion is given by the following equation, where q is the plasma charge, c is the plasma charge, ω_p is the plasma frequency and ω the laser frequency:

$$\Delta\kappa_q\ , \mathrm{plasma} = \frac{\omega_p(1-q^2)}{2qc\omega} \tag{26}$$

Another contribution to the phase matching condition is the dispersion due to neutral atoms. This dispersion is due to the dependence of the wavelength on the refractive index. More specifically, the fundamental frequency of the laser and the harmonics produced have different refractive indices. The following expression yields the dispersion of the neutral atoms as a function of pressure (p) in STP, the percentage of ionization of atoms (η) and the difference in the refractive indices (δn). [15]

$$\Delta\kappa_q\,, neutral = \frac{2\pi q}{\lambda_0}\frac{p}{p_0}\delta n(1-\eta) \tag{27}$$

Finally, the contribution to the dispersion relation due to the atomic dipole is given by the expression: [8]

$$\Delta\kappa_{q,dip} = \nabla\varphi_{q,dip} \tag{28}$$

The intensity dependence of dipole phase is different for "short" and "long" trajectories, so good phase-matching conditions are consequently different for these two trajectories. This dipole phase is also responsible for the spectral broadening of high harmonics because the intensity variation *I(t)* in time causes a frequency chirp and it is going to play a crucial role in our analysis. [11] [16]

When a perfect phase matching is achieved between a high harmonic order q and the fundamental frequency of the driving laser field, the total emitted electric field *E* of the secondary harmonic radiation must be increased by the number of atoms N, which radiate. This is in turn proportional to the pressure (p) at which the atoms of the active medium are induced to. Because the number of photons (proportional to the light intensity) emitted in a given direction is proportional to the square of the electric field, we obtain for the harmonic intensity: [15]

$$I_q \sim p^2 \tag{29}$$

$$I_q(P) = \frac{{\omega_q}^2}{n_q(P)(n_0(P))^q c^4 {\varepsilon_0}^2}\left|x^{(3)}(P)\right|^2 {I_1}^q \frac{sin^2\left(\frac{L_q \Delta k_q(P)}{2}\right)}{\left(\frac{L_q \Delta k_q(P)}{2}\right)^2} \tag{30}$$

The Eq (29) is true for perfect phase matching, meanwhile equation (30) (where Δk_q is the dispersion, L_q is the coherence length and n_q the refractive index) holds true for imperfect phase matching.

For low photon energies, high harmonic radiation can be perfectly phase matched by balancing the neutral atom dispersion with the dispersion of the free-electron plasma that is created as the medium is ionized by the electromagnetic field of the laser including any geometric contributions. Under these conditions, phase-matched conversion efficiency over centimeter lengths can be achieved. However, the higher photon energies that are generated at higher laser field intensities that strongly ionize the gas medium. Therefore, the dispersion of the resulting plasma increases the phase velocity of the driving laser and induces a phase mis match relative to that of the harmonic field. Thus, for photon energies >130 eV, conventional phase matching of the HHG process is not possible and coherent addition of the harmonic field is limited to very short distances in the medium. Therefore, the HHG output could be enhanced by orders of magnitude if a scheme could be found to correct for this phase mis match. To solve the phase-matching problem for high harmonic fields at high photon energies, quasiphase-matching (QPM) are introduced and can either adjust the phase or eliminate the emission of harmonics from regions of the medium that would otherwise contribute destructively, through destructive interference to the high harmonic signal. [12] [13] although other techniques also exist like birefringent phase matching, where one exploits birefringence to cancel the phase mismatch, this technique comes in many variations. [12]

2.1.3 SELPH PHASE MODULATION

Self-phase modulation and self-focusing are two very important physical phenomena, affecting the shape of high intensity laser pulse. Leading most of the times to the pulses broadening.

Both phenomena are generated by the Kerr effect, in which high optical intensity in a medium causes a nonlinear phase delay which has the same temporal shape as the optical intensity, it can be described as a nonlinear change in the refractive index, as a response to an applied electromagnetic field, described by the relation: [17]

$$\Delta n = n_2 I \tag{31}$$

With the nonlinear index n_2 and the optical intensity I. In the context of self-phase modulation that we are interested in, the emphasis is on the temporal dependence of the phase shift on the intensity, whereas the transverse dependence for some beam spatial profile leads to the phenomenon of self-focusing. [19] If an optical pulse is transmitted through a medium, the Kerr effect causes a time-dependent phase shift according to the time-dependent pulse intensity. In this way, an initial unchirped optical pulse acquires a positive chirp. For a Gaussian beam with beam radius w in a medium with length L, the phase change per unit optical power is described by the proportionality constant: [18] [19]

$$y_{spm} = \frac{4n_2 L}{\lambda w^2} \tag{32}$$

The time-dependent phase change achieved by the SPM is then associated with the modification and broadening of the optical spectrum. If the laser pulse is initially unchirped or positive-chirped, SPM leads to a visible spectral broadening, whereas spectral compression will be realized, if the initial pulse is negative-chirped. For case of strong SPM, the optical spectrum can exhibit strong oscillations.

Self-focusing is a non-linear optical process induced by the change in refractive index of materials exposed to intense electromagnetic radiation. A medium whose refractive index increases with the electric field intensity acts as a focusing lens for an electromagnetic wave characterized by an initial transverse intensity gradient, as in a laser beam. The peak intensity of the self-focused region keeps increasing as the wave travels through the medium, until defocusing effects or medium damage interrupt this process. Self-focusing is often observed when radiation generated by femtosecond lasers propagates through many solids, liquids and gases. Depending on the type of material and on the intensity of the radiation, several mechanisms produce variations in the refractive index which result in self-focusing: the main cases are Kerr-induced self-focusing and plasma self-focusing.

2.2 GENERATION OF ULTRA SHORT LASER PULSES

A laser E-field pulse can be defined as a perturbation in a constant background. The shape of this pulse is the shape of this perturbation. Intuitively, the pulse shape can be represented by a bell-shaped function, such as a Gaussian function. It is known that the Fourier transform of a Gaussian function is also a Gaussian function. The general time and frequency Fourier transform of a pulse can be written as: [20] [24]

$$E(t) = \frac{1}{2\pi}\int_{-\infty}^{\infty} E(\omega)e^{-i\omega t}d\omega \tag{33}$$

$$E(\omega) = \int_{-\infty}^{\infty} E(t)e^{i\omega t}dt \tag{34}$$

Where $E(\omega)$ and $E(t)$ represent the frequency and time evolution of the electric field of the pulse, respectively. Additionally, since half-maximum quantities are experimentally easier to measure, the relationship that represents the uncertainty principle between the duration and spectral bandwidth of the laser pulse can be written as:

$$\Delta\nu\Delta t \geq K \tag{35}$$

In optics, an ultrashort pulse of light is an electromagnetic pulse whose time duration is of the order of a picosecond (10^{-12} second) or less. Such pulses have a broadband optical spectrum, and can be created by mode-locked laser oscillators. They are characterized by a high peak that usually leads to nonlinear interactions in various materials, including air and thus are very important for many nonlinear phenomena. [20]

A special ultra-short pulse, that is the main interest and the main tool of our research, is the femtosecond ultrashort laser pulse (a pulse that falls in time regimes of 10^{-15} second). The generation of such short (sub-picosecond) light pulses is nearly always achieved with the technique of passive mode locking. Thus, in order to generate a laser pulse within femtosecond time domain one needs to use a broad spectral bandwidth. That leads to pulses with moderate pulse energies (often in the nanojoule region) and high pulse repetition rates in the megahertz or gigahertz region. The spectral bandwidth is substantial for such short pulse durations.

A laser ultrashort pulse, contains all frequencies. In some cases, the higher frequencies are in the leading edge of the pulse and in some others in the trailing part. The importance of this characteristic will be unveiled in the next chapter.

The development of femtosecond laser pulse sources has opened the way to the investigation of ultrafast processes in many fields of science, giving birth to the attosecond physics. The introduction of the chirped-pulse amplification technique allowed the amplification of ultrashort pulses to extremely high-power levels. [21] Finally the femtosecond ultrashort laser pulses are the extremely important for the execution of high harmonic generation experiments.

2.2.1 CHIRP

The chirp parameter, is a function of time induced to the laser pulse, which forces the alteration of the temporal or spatial characteristics of a lasers electromagnetic field pulse. In this study, the focus is on the temporal chirp. There are several types of functions for the chirp parameter, such as the linear function chirp (eq. 30) and the geometrical function chirp (eq. 31). [22] Although, the experiments conducted in this study, were facilitated with linear chirp function. These equations are the following, where ϕ_0 is the phase, t the time and f_0 the frequency:

$$E(t) = \sin\left[\varphi_0 + 2\pi\left(\frac{ct^2}{2} + f_0 t\right)\right] \tag{36}$$

$$E(t) = \sin\left[\varphi_0 + 2\pi f_0\left(\frac{k-1}{\ln k}\right)\right] \tag{37}$$

In our case we define the chirp parameter as the Taylor expansion of the phase θ(ω) in equation [51]:

$$E(\omega) = E_0 e^{-i\theta(\omega)} \tag{38}$$

Where E is the electric field amplitude.

If we take into account that the instantaneous frequency ω(t) relates to the phase via the equation [51]:

$$\omega(t) = \frac{d\theta(t)}{dt} \tag{39}$$

The Taylor expansion yields:

$$\theta(t) = \theta_0 + \omega t + t^n \frac{d^n\theta(t)}{dt} \tag{40}$$

Where the first term represents the constant initial phase, the second term represents the frequency at t and the third term the n-th order chirp [51].

The chirp parameters then is defined as:

$$a = \frac{d\theta(t)^2}{dt^2} \tag{41}$$

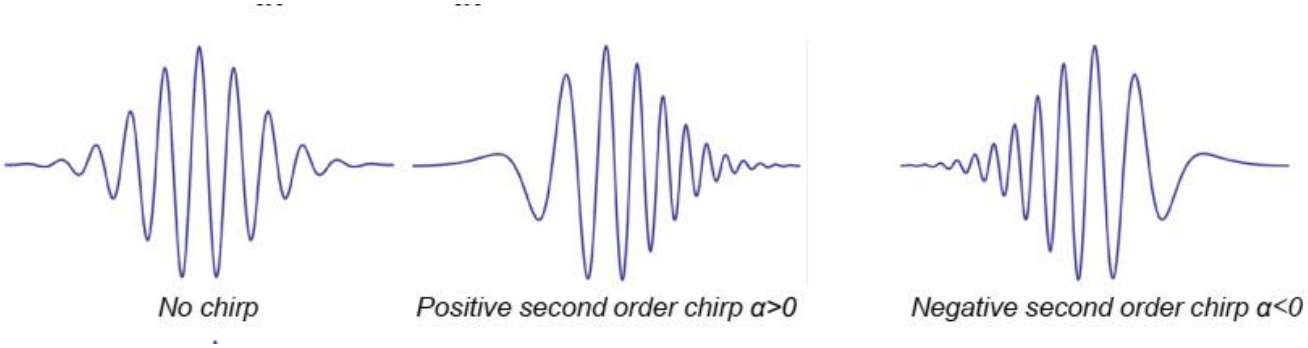

Figure 9: shape of ultrashort laser pulses for different chirps, where the broader line represents larger wavelengths. For negative chirp the larger (red) wavelengths is in the leading edge of the pulse, whereas in positive chirp smaller (blue) wavelengths are in the leading edge [picture taken from N. Papadogiannis lectures on laser matter interaction, Msc, department of electronic engineering H.M.U.).[51]

A pulse can acquire a chirp either during its propagation in a transparent medium due to the effects of chromatic dispersion and nonlinearities (for example self-phase modulation arising from the Kerr effect). In semiconductor lasers and amplifiers, chirped pulses can also result from refractive index changes associated with changes in the carrier (electron) density. The chirp of a pulse can be removed or reversed by propagating it through optical components with the suitable chromatic dispersion. For a given pulse spectrum, the minimum pulse duration is obtained when there is no chirp ("unchirped pulses"). This condition is equivalent to a constant instantaneous frequency, and (nearly) equivalent to a constant spectral phase.

There are different ways of quantifying the chirp of a pulse:

(a) The magnitude of a chirp can be considered to be the rate of change in the instantaneous frequency, in units of Hz/*s*. In the case of nonlinear chirps, this quantity is time-dependent, which means it's not a constant number for one pulse. [22]

(b) It is also possible to specify the amount of group delay dispersion (in units of seconds squared) required to compress a pulse dispersively. More precisely, this may be the second-order dispersion which leads to the smallest pulse duration, or to the highest peak power.[22]

Such definitions are not related to each other in a simple way. For example, an increasing amount of normal chromatic dispersion applied to an initially unchirped (transform-limited) pulse will obviously increase the amount of dispersion required for compression. On the other hand, the chirp in terms of the rate of change of the instantaneous frequency will initially increase, but later decrease. The latter results from the fact that the same change in instantaneous frequency will occur within a larger and larger time interval, as the pulse duration increases. furthermore, an initially unchirped pulse subject to self-phase modulation via a Kerr nonlinearity will exhibit an increasing optical bandwidth. For increasingly strong spectral broadening, the rate of change of the instantaneous frequency increases, whereas the amount of dispersion as required for maximum compression can decrease. [22]

The characteristics of the chirp parameter are extremely important because the distribution of the frequencies inside the temporal shape of the pulse affect the generation of high harmonics in various ways. So, in order to understand the effects of the chirp upon the high harmonic generation we need to understand the chirp parameter itself.

2.2.2 CPA TECHNIQUE

A typical femtosecond laser set-up comprises of several autonomous units, the oscillator which produces low-energy ultra-short pulses at regular intervals, a stretcher which converts the femtosecond pulse into a 50-200 ps chirped pulse, one or more amplifier stages to increase the pulse energy by a factor of 10^7-10^9 and finally a compressor, performing the exact optical inverse process of the stretcher, in order to deliver an amplified pulse of the same duration as the oscillator.

The most important technique in the generation of ultra-short pulses is chirped-pulse amplification (CPA) [23] and is now exploited by nearly all existing high-power, femtosecond laser systems. The importance of the CPA technique rests into the fact that the most of the optical components will be overheated and damaged if the fluence exceeds a saturation level.

Therefore, the pulse length throughout the amplifier chain has to be at least 40 ps (typical values are 100-200 ps) so that the components have time to cool by thermal conduction. The stretcher-compressor combination separates the pulse generation and amplification stages, permitting standard techniques to be used for the amplifier chain, and furthermore leaving room for more advanced phase compensation devices at either end. [24]

The first step of the CPA technique is the conversion of a continuous-wave (CW) pump laser beam into a repeated train of short laser pulses. This is achieved by exploiting a property of the Ti: sapphire crystal, which is that it may also act as a nonlinear focusing lens. This is the so-called nonlinear Kerr effect which is an optical nonlinearity in the index of refraction that occurs, when the intensity inside the crystal exceeds 10^{11} W/cm^2, so that by blocking the unfocused CW mode with a slit, one ends up with a single, short pulse bouncing to-and-from in the oscillator. This arrangement is unstable because dispersion will cause the pulse to spread out longitudinally (red wavelengths are faster than blue ones), so to compensate this, a set of prisms are inserted between the crystal and back mirror, which imposes an equal but opposite dispersion on the pulse (blue faster than red). The combination of cavity plus dispersion-correction constitutes a highly stable and reliable femtosecond laser. [24] The fs pulse from the oscillator typically contains just a few nJ of energy, but for cutting edge experiments an increase of the pulse power to the TW level and beyond is needed. As already mentioned, to avoid damaging optical elements, the pulse must first be stretched by a factor of 10^3-10^4 or so. This is usually done with a pair of diffraction gratings, which impose a positive chirp on the pulse, so that longer wavelengths emerge before shorter wavelength. The stretched pulse can now be amplified via a process which is usually split into two or more stages, depending on the final beam energy required.

A multipass configuration is typical of modern tabletop-TW systems, producing gains of 10^2-10^3.The amplified, long chirped pulse is then recompressed using a grating pair, ideally reducing the pulse length back down to a value slightly above the one originally emitted by the oscillator. Some pulse lengthening is inevitable due to a combination of nonlinear dispersion effects and gain-narrowing. The latter arises because the amplifier medium preferentially enhances central wavelengths over peripheral ones, leading to a reduction in bandwidth and hence lengthening of pulse duration Due to the high-quality beam profile which can be produced by Ti: sapphire amplifier systems, the pulses can be focused to an almost transform-limited spot containing most of the laser energy. An important feature of the generation of ultra-short pulses from a laser system is the mode locking. In general, a laser transition has a finite Iinewidth over which it can provide optical gain and so laser emission has a finite spectral bandwidth δv. In a laser cavity, the radiation is confined to discrete frequencies or 'modes', $v_{n,,}$ which are separated by δv, the mode-spacing (eq.32). [24]

$$\delta\nu = \frac{1}{T_{Rt}} = \frac{c}{2L} \tag{42}$$

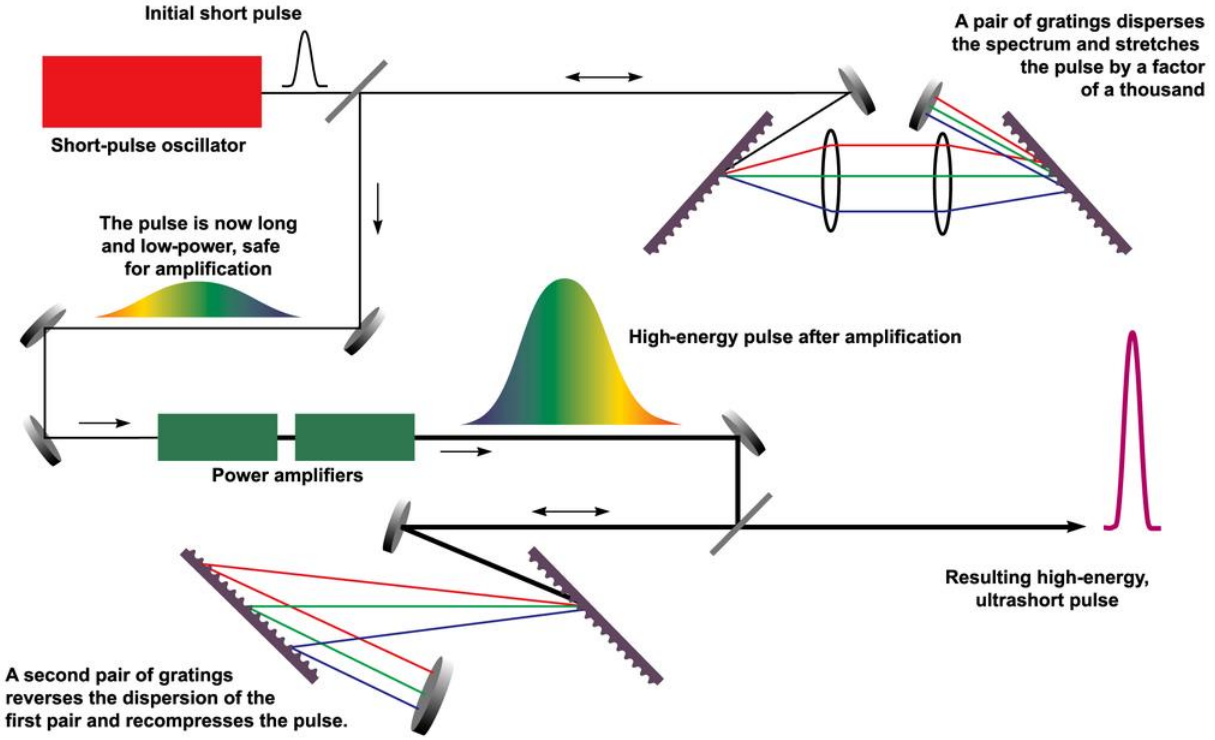

Figure 10: schematic of the CPA technique, where the different stages of laser pulse compression and decompression are demonstrated (Taken from Wikipedia and LLNL S&TR of September 1995)

When no attempt is made to control the laser spectrum, the "free-running" laser modes oscillate independently with random phases. The resulting laser output is noisy and incoherent with no regular temporal structure. On a very short timescale, given by the inverse of the optical bandwidth, some or all of the modes can radiate in phase and this will produce a sharp feature in the laser output described as a 'coherence spike'. The duration of these spikes or the 'coherence time' of the laser, can thus be as short as $1/\delta\nu$. The coherence length of the laser is given by $c\, t_{coh.}$ If all the modes of the laser can be made to oscillate in phase, which means they can be locked together, then the laser output becomes temporally well defined, with a period corresponding to the cavity round-trip time (T_{RT}) (eq. 33). The temporal profile is the Fourier transform of the spectral profile and so, if complete mode-locking is achieved, the duration of the pulses, which is related to the full gain line width by Heisenberg's uncertainty principle. [25]

$$\mathrm{T_{Rt}} = \frac{\mathrm{c}}{\mathrm{2L}} \tag{43}$$

When all the modes in the cavity are oscillating either in phase or with a constant phase difference between the modes, then the laser pulse output is described as transformed-limited. Finally, although the temporal field profile $E(t)$ is always the Fourier transform of the spectral field

profile $E(v)$, only in the special case of transform-limited pulses can the pulse shape be determined from the optical spectrum alone, in all other cases it is necessary to know the phase profile of the pulses in order to calculate the temporal profile from the spectral profile. [25]

Techniques for mode-locking lasers fall into two broad categories, active and passive mode-locking. In the first approach the radiation in the laser cavity is modulated by a signal derived from an external clock source which is matched to the cavity round Trip time. In the latter case, the laser radiation itself generates a modulation through the action of a non-linear device i n the laser cavity. This modulation is thus automatically synchronized to the cavity round-trip frequency and requires no external clock signal. Passive mode-locking is often referred to as self-mod locking. [25]

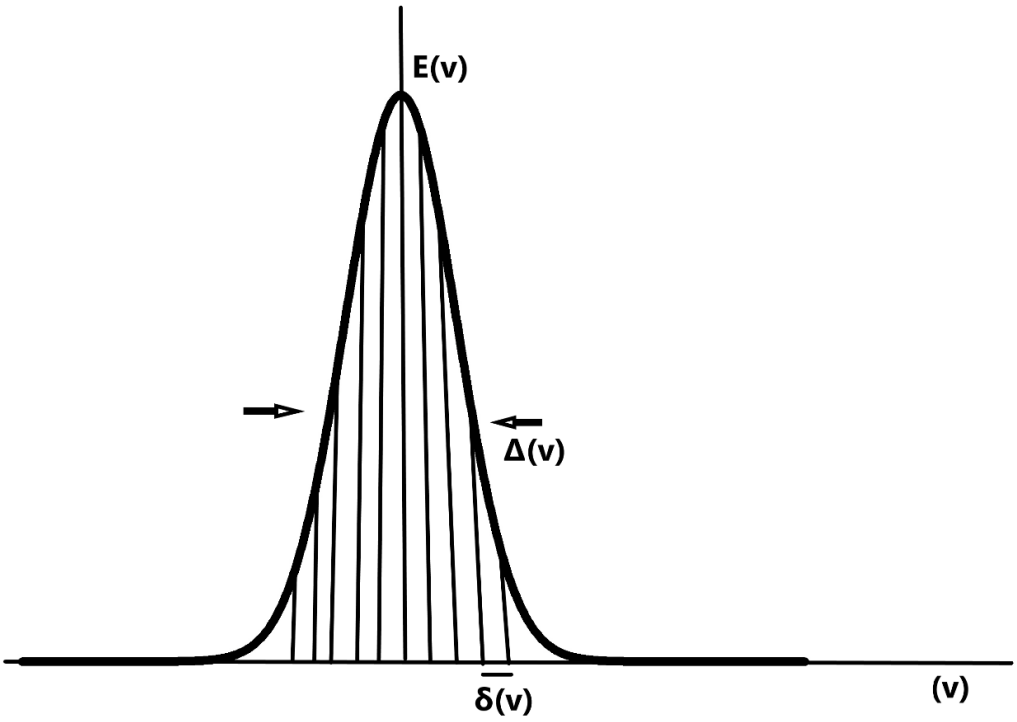

Figure 11: schematic of mode locked laser emission.

Active mode-locking is realized into the frequency domain. It is executed by letting the laser radiation signal interact with a signal derived from an external oscillator. An 'active' modulator periodically changes the loss or gain experienced by the intracavity laser radiation and generates sidebands on the laser radiation modes at a frequency corresponding to the modulation frequency. If this gain or loss is set equal to the laser cavity mode-spacing, then energy is transferred between adjacent laser modes, which then become coupled together in time and so oscillate in phase. [25]

The simplest model of a passively mode-locked laser system, is constituted by just an amplifier and a saturable absorber providing an intensity dependent loss in a laser cavity. Amplitude modulation is provided by the interaction of the laser pulse itself with the intracavity elements and no external modulation is required. [25]The Passive mode-locking process exploits a phenomenon called the optical Kerr effect (The Kerr effect, is a change in the refractive index of a material in response to an applied electromagnetic field), This refractive index variation is responsible for the nonlinear optical effects of self-focusing, and self-phase modulation.[17]

2.2.3 AUTOCORRELATORS

Optical autocorrelators are used for various purposes, in particular for the detailed analysis of light, in particular for the measurement of the duration of ultrashort pulses with picosecond or femtosecond durations, where an electronic apparatus would be too slow.

The basic principle of operation of an autocorrelator for a pulse duration measurement is to check the correlation of the temporal pulse trace with itself. A beam splitter creates two copies of the incoming pulses. These copies are superimposed in a nonlinear medium, where they interact on the basis of some nonlinearity, provided that they overlap temporarily.

An intensity autocorrelator consists of, a beam splitter, which splits an incoming pulse into two pulses, which are then focused and sent into a crystal with a $\chi^{(2)}$ nonlinearity. The arm length difference and thus the relative timing of the pulses can be mechanically adjusted via the variable optical delay line. (Different kinds of delay lines are used, e.g. using rotating glass blocks or mirrors mounted on loudspeakers.) If the arm length difference is made small, so that the pulses meet in the nonlinear crystal, the process of sum frequency generation occurs, leading to an output with a shorter wavelength. If the relative time delay is increased, so that the overlap of the two pulses in the crystal is reduced, the mixing product becomes weaker. Obviously, that overlap is lost sooner if the pulses are rather short. For measuring the pulse duration, the power of the mixing product is recorded as a function of the arm length difference. This can be done under computer control. [26]

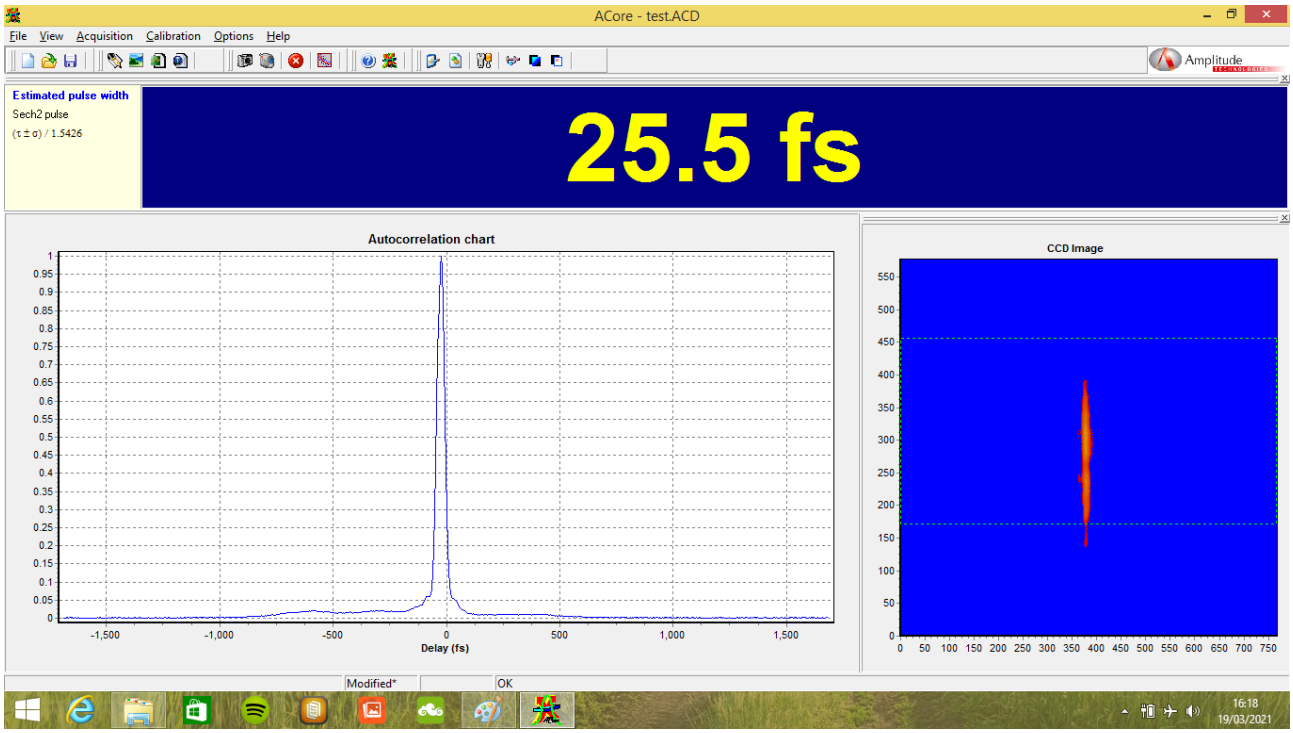

Figure 12: Typical intensity autocorrelator signal, where the pulse is demonstrated as well as the resulted signal in the CCD camera, the imaged pulse has 25.5fs duration and it is referred to the FTL pulse (taken from the bonzai autocorrelator used in the high harmonic generation experiments)

An interferometric autocorrelator contains a Michelson interferometer with a variable arm length difference. The superimposed copies of the pulse are collinearly propagating into the nonlinear crystal (after focusing with a lens or curved laser mirror) and have the same polarization. This kind of autocorrelation trace exhibits a fast oscillation with a period of half the optical wavelength. The maximum signal is obtained when the two pulses after the beam splitter undergo perfect constructive interference, leading to twice the amplitude compared with a single pulse, and thus four times the intensity, and after frequency doubling 16 times the intensity. For a large arm length difference, the pulses do not overlap in the nonlinear crystal, and the intensity is only twice that generated by a single pulse. Hence the peak signal is always eight times higher than the background, provided that the interferometer is properly aligned. The interferometric autocorrelation is sensitive to chirps and thus in principle makes it possible to extract more information on the pulses.[26]

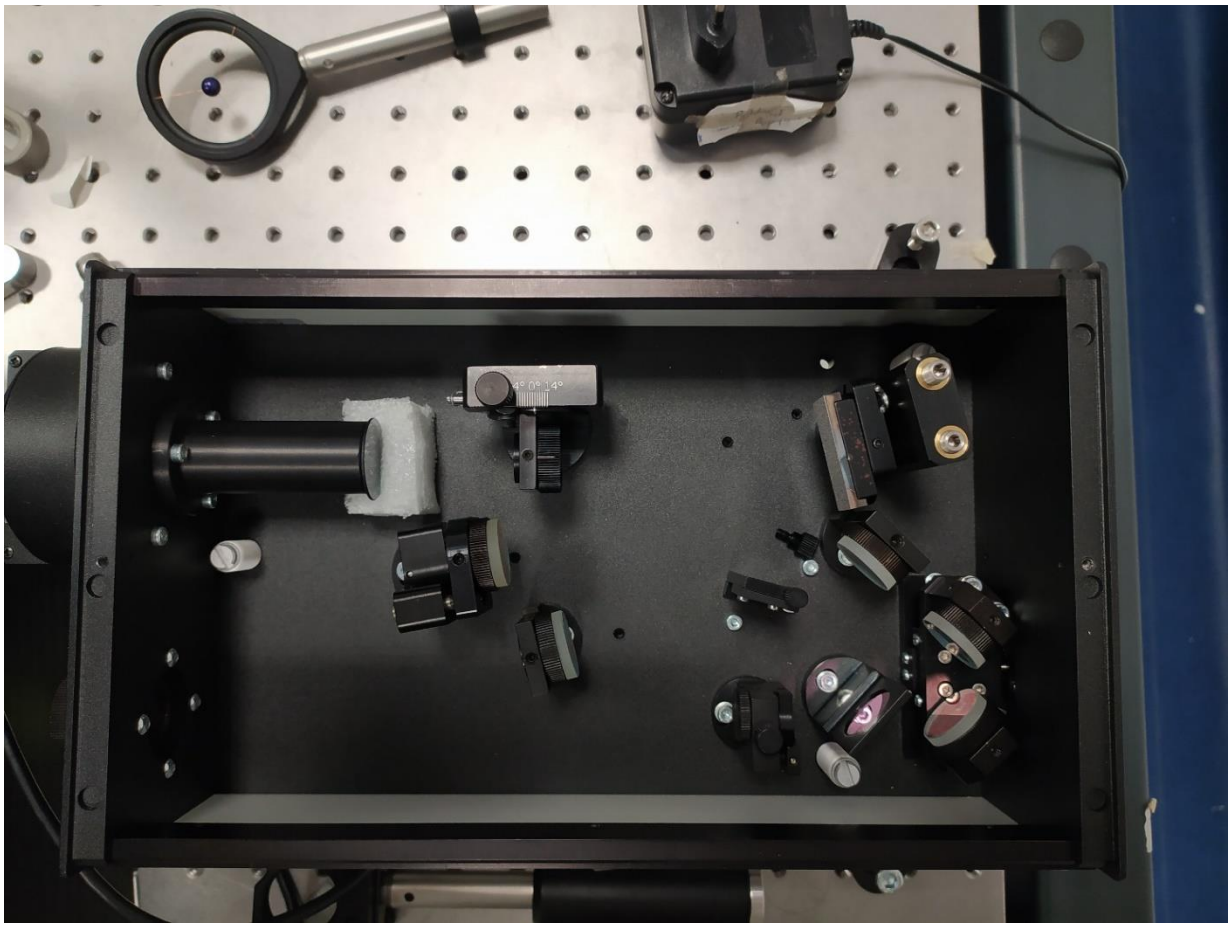

Figure 13: the interferometric autocorrelator used in the experiments conducted, in IPPL for the study of high harmonic generation. Inside the box, various mirrors and beam splitters facilitate the splitting of the laser beam. This procedure allows us to make correlation measures of the pulse though the process of constructive and destructive interference.

2.4 HIGH HARMONIC GENERATION WITH CHIRPED PULSES

The scope of this chapter is to present in some detail, the current level of research that has been done until now, regarding the use of chirped laser pulses in the process of high harmonic generation. The extremely important applications of High harmonic radiation in various advanced areas of modern physics, such as plasma physics and attoseconds physics, as well as their contribution in the medical and technological field, guides the effort for the optimization of their generation and the optimization of their efficiency. The utilization of chirped laser pulses is an important method to influence the factors that determine the success of this enhancement and optimization process.

One of the first attempts to explore the physics of the chirped high harmonic generation was made by Zhou et.al in their article about the enhancement of high harmonic generation by means of wavelength tuning from chirp sign adjustment (J. Zhou et al physical review letters vol. 76, *5*, (1996)). In their article they used a 3TW Ti: sapphire laser to experimentally produce high harmonic radiation from noble gas (argon) targets and demonstrate that the wavelength of the harmonics can be tuned by adjusting the sign of the chirp of the excitation pulse, manifesting a tunable ultra-short pulse with duration of less than 25fs. The results not only succeed in demonstrating the expected tunability but also showed, that the observed harmonic radiation energies and the harmonic orders are unexpectedly high when compared with experimental and theoretical results yet achieved but for longer excitation pulses. They also observed that the efficiency of harmonic production is highest for shorter pulses, as well as shift in the harmonic spectra.

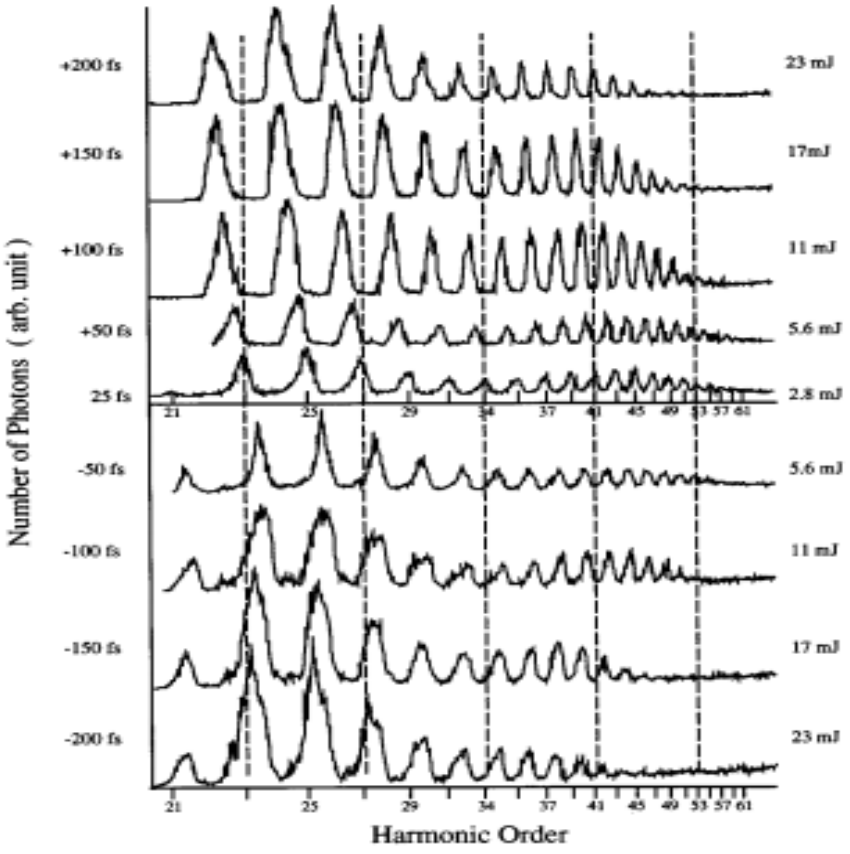

Figure 14: This figure demonstrates the relative harmonic intensities corresponding to various chirps (picture taken from J. Zhou et al [27])

Afterwards in 1998, Z. Chang et al, showed in their article about the temporal phase control of soft x ray emission (Z. Chang et al. [28]) a strong dependence of the soft-x-ray high harmonic spectra generated by the high harmonic emission, on the chirp of the excitation laser pulse. This behavior is explained in the article by simulations, which combine the chirp of the laser with the intrinsic phase shift of the harmonics. For identical pulse durations, distinct harmonic peaks can be observed for positively chirped excitation pulses, while for negatively chirped pulses, the harmonic peaks become irregular merging into the continuum. Thus, their results conclusively demonstrated that the high harmonic generation is very sensitive to the chirp of the excitation pulse.

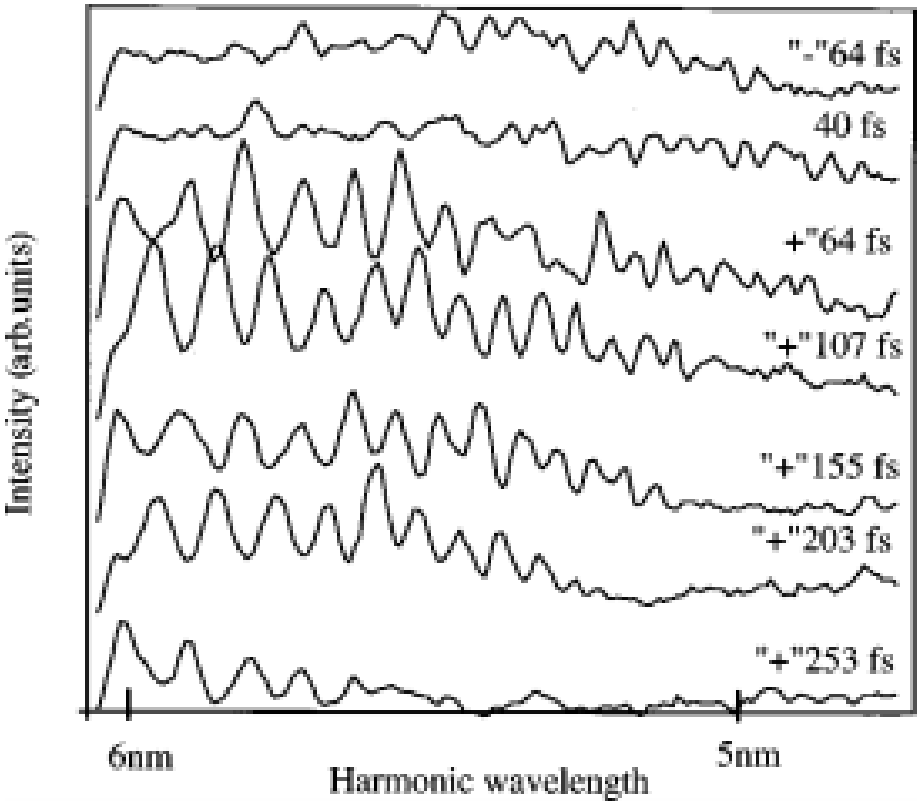

Figure 15: Demonstration of the distinct harmonic peaks for the positive chirp (picture taken from Z. Chang et [28])

Further work on the tunability and the enhancement of high harmonic generation produced by chirped laser pulses was done by Kim et.al. [29]. in their article about continuous tunable high harmonic generation from atoms under the influence of an intense femtosecond laser (Hyung taek Kim et al. [29]). A Ti: sapphire laser was used and was focused on a helium jet positioned after the laser beam's focal spot to generate a single peak harmonic. By the utilization of the property of the high harmonic blue shift the chirped control of harmonics achieved, from chirped femtosecond laser pulses. This continuous control of laser energy and chirp allowed the tuning of high-order harmonics. This process, opened a new pathway for the construction of a continuously tunable, coherent, femtosecond x-ray radiation source, which allowed new applications to be explored. This versality in applicability of this method rests in the fact, that this wavelength-tuning requires only the rotation of the half-wave plate in the compressor for laser-energy control and the adjustment of the grating separation in the pulse compressor for chirp control, with both modifications being easily automated.

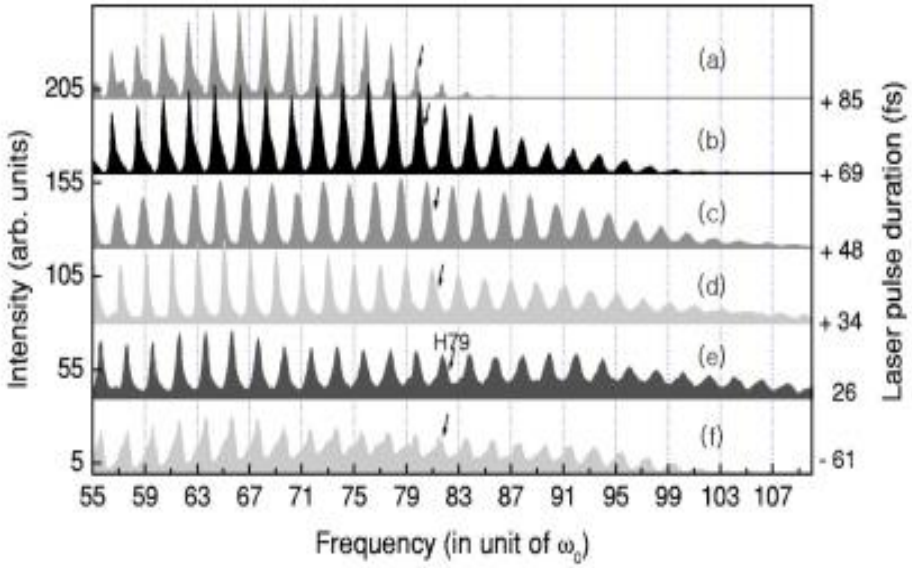

Figure 16: Blue shift of the H79 harmonic (picture taken from Hyung taek Kim Et al. [29])

The next target of the researchers was the optimization of the brightness of the high harmonic spectra. This was achieved by Kim et al by using a self-guided femtosecond laser (H. T. Kim. et al. [30]). They achieved the optimization of the brightness of high-order harmonics from a long neon gas jet using self-guided and chirped laser pulses. Those self-guided and chirped laser pulses effectively reduced the ionization effects in space and time, producing bright high-order harmonics with narrow bandwidth. A proper selection of the target position resulted in the self-guiding of the laser pulse, which provided efficient high order harmonic generation. Since self-phase modulation induced a positive chirp at the leading edge of the laser pulse, wherein the harmonics are mainly generated, negatively chirped pulses generated sharp harmonic spectrum. This proposed method for control of the brightness of the high order harmonic is very important, because of the usefulness of bright high order harmonics with narrow spectrum on various applications.

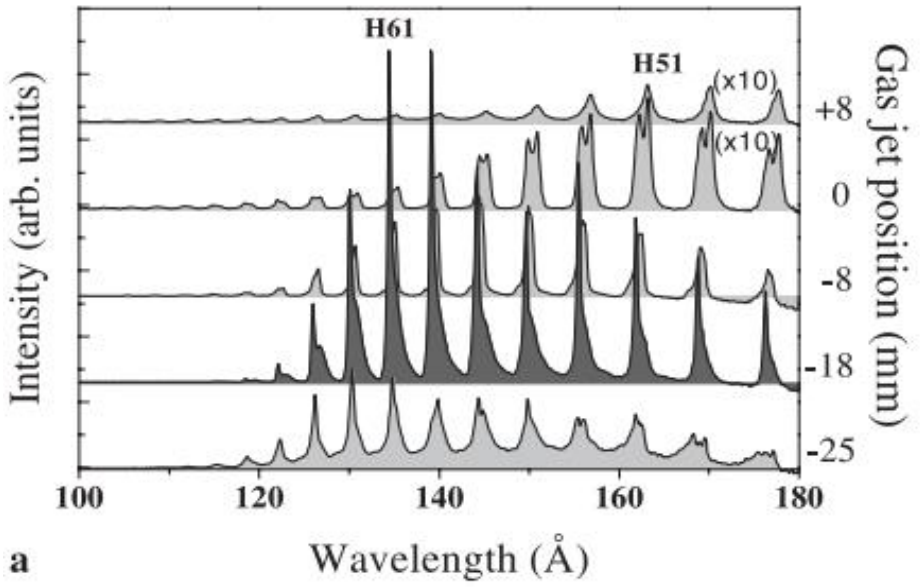

Figure 17: Optimizes the brightness of a single harmonic by laser gas jet position (picture taken from H. T. Kim. et al. [30])

The next step in the exploration was done by V. Tossa et al. in their article about the high order harmonic generation by chirped and self-guided femtosecond laser pulses (V. Tossa et al. [31]). They presented a time-dependent theoretical and experimental analysis of high-order harmonics generation by a self-guided femtosecond laser pulse propagating through a long gas jet. They also developed a three-dimensional model to calculate the harmonic fields generated by the laser pulses, which only differed by the sign of their initial chirp. Their experimental arrangement consisted of a Ti: sapphire laser, with variable duration and chirp pulses, those were focused using a spherical mirror on to a long neon gas jet produced from by a slit nozzle. The 3D adiabatic model they developed was based on the solution of the wave equation for ionized gases, by means of the Fourier transform and the crank-Nicolson scheme, which yields the space time evolution, finally the solution of the propagation equation using the strong field approximation yielded the harmonic field. Their results that consisted of the time-frequency distributions of the single atom response and of the high harmonic field demonstrated that only the cutoff trajectories survived to formulate the final harmonic spectrum. A follow up time-dependent phase-matching calculation that was done, considering the chirp and self-phase modulation of the driving field. The resulting phase-matching distributions for different time instants during dipole emission showed, that for the cutoff trajectories, phase-matched high harmonic generation was achieved only in a few laser optical cycles during a single-atom emission. Finally, they demonstrated that a small number of harmonics, those which exhibit the single atom response in the plateau but closer to the cutoff, proved to have the most favorable phase-matching conditions, and thus are powerfully generated.

$$\nabla^2 E_1(r,z,t) - \frac{1}{c^2}\frac{\partial^2 E_1(r,z,t)}{\partial t^2} = \frac{\omega_0^2}{c^2}(1-\eta_{eff}^2)E_1(r,z,t) \tag{44}$$

$$\nabla^2 E_h(r,z,t) - \frac{\eta^2}{c^2}\frac{\partial^2 E_h(r,z,t)}{\partial t^2} = \frac{\mu_0 \partial^2 P_{nl}(r,z,t)}{\partial t^2} \tag{45}$$

More work on the enhancement of a single harmonic via the control of the chirp of the driving laser pulse during high harmonic generation from gases was done by Ganeev et al in 2006 [32]). In their experimental research the plasma produced by a picosecond prepulse on the target surface of the gas target was used for the high harmonic generation (up to the 43rd order) using femtosecond pulses from a Ti: sapphire laser with different chirp. The high-order harmonics generated from the gas plume showed a plateau pattern. Further studies revealed that the high harmonic generation was caused by the interaction of the femtosecond pulses with the gas's ions. They achieved control of the chirp of the driving laser pulse, in order to tune the harmonic spectrum in the XUV range and achieved a significant enhancement of a single harmonic (27th). Their results also have shown that the chirp control of the fundamental laser leads to a significant variation of the harmonic intensity distribution in the plateau region for some specific ablated target. This new approach may pave a way for efficient single-harmonic enhancement in the XUV range using different plasma sources.

In 2011 Katalin Kova´cs [33], in which they numerically investigated the high-order harmonic generation in the presence of a chirped THz pulse, with a complete 3D nonadiabatic model. The assisting THz pulse illuminates the high-order harmonic generation gas cell laterally inducing quasi-phase-matching. The results demonstrated that it is possible to compensate the phase mismatch during propagation and extend the macroscopic cutoff of a propagated strong IR pulse to the single-dipole cutoff. They achieved 2 orders of magnitude increase in the harmonic efficiency of cutoff harmonics using a THz pulse of constant wavelength, and a further factor of 3 enhancement when a chirped THz pulse is used. Finally, by tuning the THz pulse parameters one can

select the spectral range in which harmonic radiation can be amplified, also by tuning the THz field one can finely shift the central frequency of the amplified spectral range toward lower harmonics.

Expanding this work, in 2014 Xu Wang, Cheng Jin, and C. D. Lin published a paper on the Coherent control of high-harmonic generation using waveform-synthesized chirped laser fields (Xu Wang, Cheng Jin [34]. They succeed in demonstrating that waveform-synthesized chirped laser fields are efficient tools for coherent harmonic control. They showed that a single harmonic order, or two harmonic orders, can be selectively enhanced by using a two-color field allowing a moderate linear chirp for each color. So different harmonic orders within a wide spectral range can be selectively enhanced by easily adjusting only the laser parameters. The authors proposed the combination of the two current techniques of coherent harmonic control, namely, single-color phase shaping and multicolor amplitude synthesis, in order to achieve better harmonic control for some purposes. They suggested a combination of two colors or three colors and allowed a linear chirp for each color. Their result showed that a single harmonic (or two harmonic orders) can be selectively enhanced by a many order of magnitudes by just using these simplest combinations. Thus, harmonic orders from a wide spectral range can be selectively enhanced by adjusting only a few parameters and the laser field maintains a simple analytical form. They applied two analyzing methods which provide consistent physical insights. One is time-frequency analysis and the other is half-cycle analysis. Finally, a properly chirped two color field is found to optimize the temporal coherence of different half cycles.

Finally, is important to be noted that a great amount of research has been done in the development of the semi-infinite cell scheme, which is very important for the efficient generation of high harmonic radiation.

Great work on the semi-infinite cell technology has been done from S.M. Teichmann et al. they studied high harmonic generation in a new target geometry, namely the semi-infinite gas cell. This type of target is generally characterized by high output fluxes. By obtaining far-field spatially resolved spectra, they observed structures which can related to the interference of long and short trajectories of the high harmonic radiation across the transverse plane of the generating electromagnetic field, modulated by the varying intensity profile of the fundamental field. High-order harmonic generation has been realized in a semi-infinite gas cell using a commercial, amplified Ti: sapphire system. Finally, by analyzing phase matching and absorption characteristics of our experiment, we show that longitudinal phase mismatch and absorption restrict the observed signal to the harmonics generated at the exit plane of the target chamber.

In 2014 J. R. Sutherland et all published an article (American optical society 2004 J. R. Sutherland, E. L. Christensen, N. D. Powers, S. E. Rhynard, J. C. Painter and J. Peatross) about High harmonic generation in a semi-infinite gas cell. Where they used Ten-millijoule 35-femtosecond laser pulses to interact with a semi-infinite cell of helium or neon that extended from a focusing lens to an exit foil near the laser focus. High harmonic orders in the range of 50 to 100 where generated and investigated as a function of focal position relative to the exit foil. An aperture was placed in front of the focusing lens which increased the brightness of observed harmonics by more than an order of magnitude. Counter-propagating light was used to directly probe where the high harmonics where generated within the laser focus. The results they obtained about high Harmonic generation in the two gases shows similar behavior, with small differences, the most pronounced of them being that helium exhibits stronger overall emission and more orders, up to the low 90s. In the case of helium, the optimal position of focus was 8mm further inside the foil compared to. Harmonics from both gases exhibited significant enhancement when the beam was restricted with an aperture at the focusing lens. Probing with counter-propagating light revealed that in neon the harmonics are produced in a 2mm region near the exit foil while in helium the harmonics are produced over a

much longer distance. These differences are explained by the fact that harmonics are generated in helium over an extended range relative to that in neon, which was consistent with differences in absorption rates of the two gases. The measurements suggested that the harmonics are phase matched over many millimeters, much longer than would be expected.

Further exploration of the physics of the semi-infinite sell was directed in its utilization in phase matching schemes. As was shown in the article of Daniel S. Steingrube et el. [36]. In this publication the phase matching of high-order harmonic generation is investigated experimentally for various parameters in a semi-infinite gas-cell geometry. The optimized harmonic yield is identified using two different noble gases Xe and He and its parameter dependence is also studied. Beside the straightforward setup of the semi-infinite gas cell, this geometry promises a high photon flux due to a large interaction region. Moreover, since the experimental parameters within this cell are known accurately, direct comparison to simulations were able to be performed. In the obtained results the Spectral splitting and blueshift of high-order harmonics was observed.

In their experiment Harmonic spectra were observed while focus position and gas pressure were let to be varied systematically. This way, experimental phase-matching maps were generated in helium and xenon for lenses with different focal lengths. Both experiment and simulation showed that optimal phase-matching conditions for the generation of high-order harmonics in helium and xenon were reached when placing the focus position within the gas cell. Spectral splitting of single harmonics and blueshift was found to depend on pressure, focus position, and pulse energy.

Finally, in 2015 Cuong Van Vuong et al in their article about the Phase-matched high-order harmonic generation in a semi-infinite gas cell with absorbing gaseous media [50] experimentally studied the pressure dependent high-order harmonic generation in a semi-infinite gas cell with different absorbing gaseous media in order to reveal the influence of absorption in the high harmonic generation (HHG) process. The study was performed by o measuring the absorption cross-section of the harmonic radiation and that allowed the investigation of the pressure independent phase mismatch. The harmonic source in this experiment was a by 800 nm multi-pass multi-stage chirped-pulse amplifier laser system. This laser produced fs pulses with an energy in the mJ regime. The laser pulses are focused into a long gas cell. The results of this experiment showed that it is easy to generate high-order harmonics with a high conversion efficiency and a narrow bandwidth as phase-matched and absorption-limited in the long gas cell.

In conclusion, it is obvious that in recent decades great research was done, by a lot of scientific teams around world, regarding the utilization of new geometrical schemes such as the semi-infinite cell for the generation of high harmonic radiation. As well as, the exploration of the ability of the chirp to manipulate the harmonic spectra and selectively enhance or shift a specific harmonic. This work was inspired by the versality of the application of the high harmonic generation in physics and technology. Thus, considering the many questions that remain unanswered we are set to continue moving forward. The direction we decided to take in forwarding our knowledge, is to combine the generation of high harmonic radiation in a semi-infinite cell and the study of the effects of the chirp on the intensity profiles of the high harmonic spectra.

2. THE EXPERIMENTAL SETUP

Exploring the effects of chirp on the spectrum in high harmonic generation we employ the probe pulse of IPPL/HMU 40TW laser system (ZEUS), which is a compact ultra-short (in the femtosecond regime) laser pulses source. The vacuum compressor of the ZEUS Laser provides ~1.1 J pulse energy at a 10 Hz repetition rate. The pulse length is about 25fs and leads to a peak power higher than 40TW. The probe laser of the ZEUS laser system provides also 10 Hz ultrafast laser pulses with maximum pulse energy at the output of a separate air-compressor of ~10 mJ and 26 fs pulse duration.

The system consists of a Titanium-Sapphire laser based on the Chirped Pulse Amplification (CPA) technique. The system amplifies pulses from a Ti: sapphire Oscillator and consists of a booster, a stretcher, a regenerative amplifier, and 10 Hz multi-pass amplifiers with respective pump lasers, vacuum and air compressors. The applied CPA technique consists of temporal stretching of the ultra-short laser pulse delivered by an oscillator (by a factor of 1000 up to 10000), in order to safely amplify the pulses in solid state materials. Stretching produces a chirped pulse. After amplification, the laser pulse is temporally compressed back to duration as close as possible to its initial value. After the compression stage, one should obtain in principle a high intensity ultra-short pulse free of chirp. Stretching and compression are usually achieved by means of dispersive systems such as gratings or prisms. The principle is to create different optical paths for each wavelength of the spectrum. It should be noted that the Blue path is longer than the Red one. Therefore, Blue wavelengths take more time to travel through the system than Red ones. Once stretched, the pulse can be amplified in several amplification stages, using regenerative and/or single-/multi-pass amplifiers. At the output of the amplifying system, the energy does not depend on the input pulse duration delivered by the oscillator. The limit comes from possible damage that could be caused to the amplifying material. The amplified pulse energy which can be reached without damage is higher if the stretched pulse is longer. After amplification the pulse must be compressed. A compressor device based on a wavelength dispersion system similar to the stretcher. This compressor is theoretically able to compensate for any stretching introduced into the pulse, but the gratings need to be perfectly aligned. Particularly, the incident angle onto the compressor has to be finely adjusted in order to compensate for the stretcher and the dispersion effects through the amplifier.

The femtosecond laser oscillator that we use to generate our pulses, has four major components: the gain material, the pump laser, the feedback mirrors that form an optical resonant cavity, and the dispersion compensation optics. Femtosecond pulses from the oscillator cavity are generated by a mechanism called mode locking. To generate 10 fs pulses, the phases of $N=10^6$ modes must be constant. In order to improve the contrast ratio, an optional module is currently available. This module consists of a compact multipass amplifier to amplify the oscillator output up to the micro joule level. The pulse is then cleaned by a saturable absorber that removes residual ASE (Amplified Spontaneous Emission) background of the oscillator pulses before generation. This module also contains an electro-optical device, the pulse picker, which creates a 10 Hz pulse train from the 80 MHz oscillator pulse train. The initial amplification stage consists of a regenerative amplifier producing around 1mJ stretched pulses at 10 Hz. It includes two Pockels cells: one is used to induce the stretched pulse into the regenerative cavity and the other ejects out the pulse at the maximum energy level. High power multipass amplifiers use only flat mirrors and do not affect the quality of the beam. An electronic module is installed to synchronize and switch the different Pockels cells involved in the system. The high-power amplification delivered by the system is delivered by multi-pass amplifiers. The Nd: YAG CFR200 laser produces the gain in the first multi-

pass amplifier (which is called Pre-amplifier). The second multi-pass amplifier is pumped by 1.2J, 532nm prepulse delivered by one Nd: YAG laser the main amplifier is pumped by 5J delivered by 2 prepulses and a Nd: YAG lasers. Due to the high average power of the pump beams a cryogenically cooled Ti: sapphire mount is used in the main multi-pass amplifier.

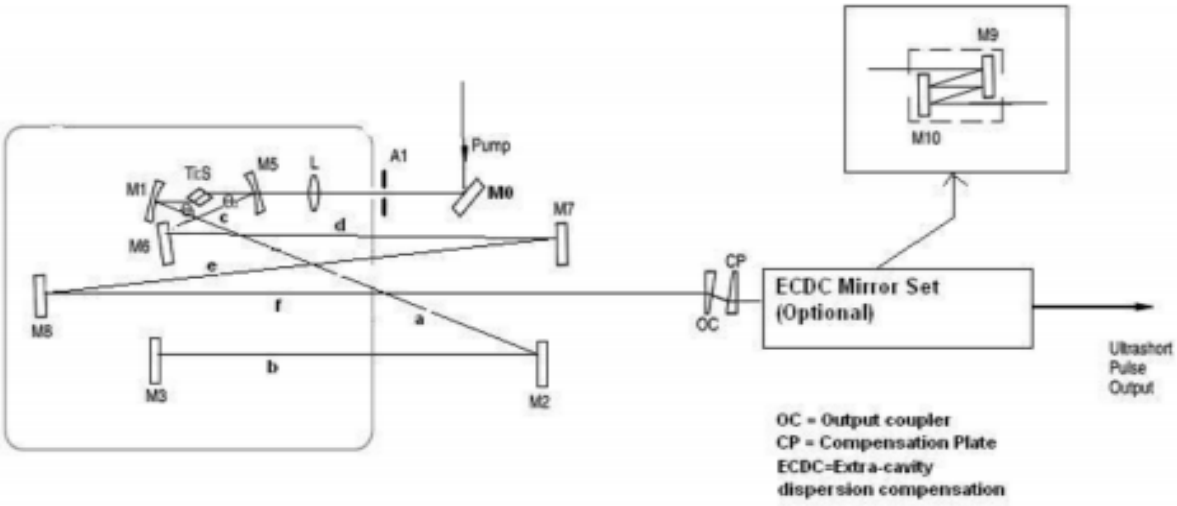

Shortcut	Description	Function
Pump Laser	DPSS 532nm pump source	Seeding the oscillator
M0	HR 532nm mirror	Beam steering mirror
L	lens	Focusing unit for 532nm beam
M1 & M5	Standard Input Coupler	Focus the red beam in the cavity
M6, M7, M8	Chirped mirror in the long arm	Dispersive mirror for steering the red beam in the cavity
M2 & M3	Chirped mirror in the short arm	Dispersive mirror for steering the red beam in the cavity (M3 = endmirror)
OC	Output coupler	Output coupler for the output beam
CP	Compensation plate	Direct the beam after the OC and adjust the dispersion for short pulses
ECDC	Extra cavity dispersion controle	To control the dispersion of the OC and CP to get the shortest pulse

Figure 18: schematic of the laser system, employed in the high harmonic generation experiments conducted in IPPL. (Zeus laser system manual)

A Faraday rotator is a polarization rotator based on the Faraday Effect, a magneto-optic effect involving transmission of light through a material when a longitudinal static magnetic field is present. The state of polarization (such as the axis of linear polarization or the orientation of elliptical polarization) is rotated as the wave traverses the device, which is explained by a slight difference in the phase velocity between the left and right circular polarizations. In a Faraday rotator, the passage of light in opposite directions experience a magnetic field in opposite direction relative to the propagation line, and since the rotation (relative to the direction of propagation) is determined by the magnetic field, then rotation is opposite between the two propagating directions. [38]

For Short pulse (< 30 fs) requirements, an optional AOPDF Acousto-Optic Programmable Dispersive Filter (or Dazzler) is added, right after the pulse stretcher. For standard laser systems, the *Dazzler* is used as a phase modulator to pre-compensate dispersion and phase distortions introduced throughout the laser system, but also as an amplitude modulator to optimize the laser output spectrum. The *Dazzler* would only be used for phase control, while another device, the *Mazzler*, would be used to optimize and enlarge the spectrum. This allows decreasing the pulse duration down to 20 fs.

Diffraction gratings are used for dispersing light that is for the spatial separation of light into different wavelengths. Their existence is essential in the production of a harmonic spectrum. This diffraction grating rests inside the vacuum chamber and its different set than that used for compression in the laser system. A typical diffraction grating comprises a substrate of an optical material with numerous parallel grooves ruled or reproduced on its surface. The substrate is coated with a reflecting material like aluminum. The quality and spacing of the grooves are significant to the performance of the grating. The basic grating equation can be obtained by assuming a section through the grating surface at right angle to the ruling direction as a saw tooth pattern.

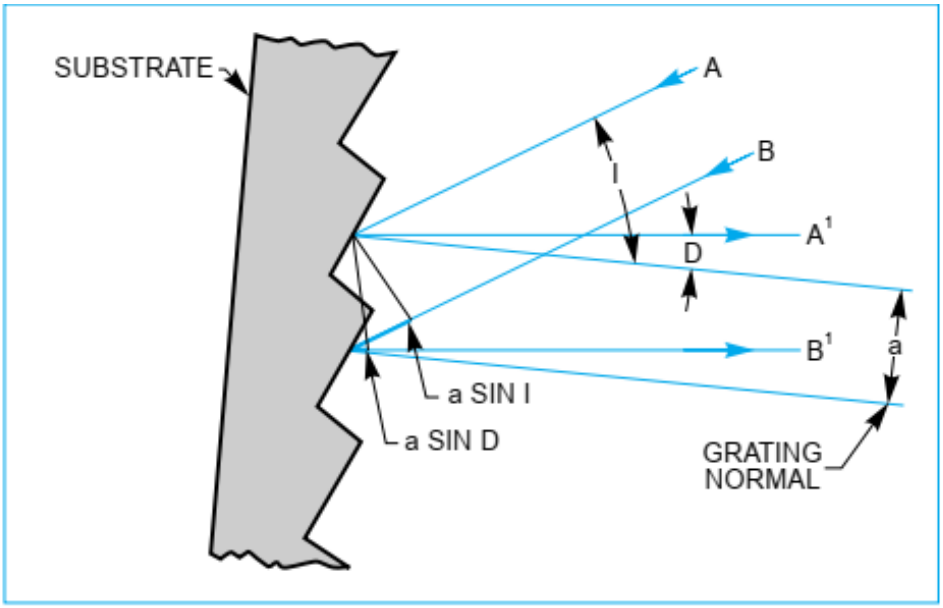

Figure 19: Figure shows the incident of light rays A and B with a wavelength of λ on adjacent grooves at angle I to the grating normal. If the incident light is considered at angle D to the grating normal, then it originates from the A and B rays when they hit the grating. Then the path difference between the A^1 and B^1 rays is a sin I + a sin D. Adding the A^1 and B^1 rays gives rise to constructive interference when the path difference is the same of any integer multiple of the wavelength λ. (Hitachi grating system manual)

Therefore, the grating equation is:

$$\alpha(\sin I + \sin D) = m\lambda \qquad (46)$$

When a parallel beam of multicolored light hits a diffraction grating then the light is scattered so that each wavelength satisfies the grating equation. When the incident beam falls into the grating

a part of it is diffracted in the corresponding order, this part of the incident beam is then defined as diffraction efficiency. This efficiency is not the same for every length wave, but we can affect it by changing the characteristics of grating like angles of the grooves, their shape and their depth. This process is called blazing and the wavelength for which I have maximum efficiency is called blaze wavelength. Typically, in high harmonic generation experiments we use flat field aberration corrected concave gratings. This kind of gratings are designed in such a way that, they efficiently focus the incident beam on a flat surface, and for that reason they are the optimum choice for nonlinear and 2D flat detectors.

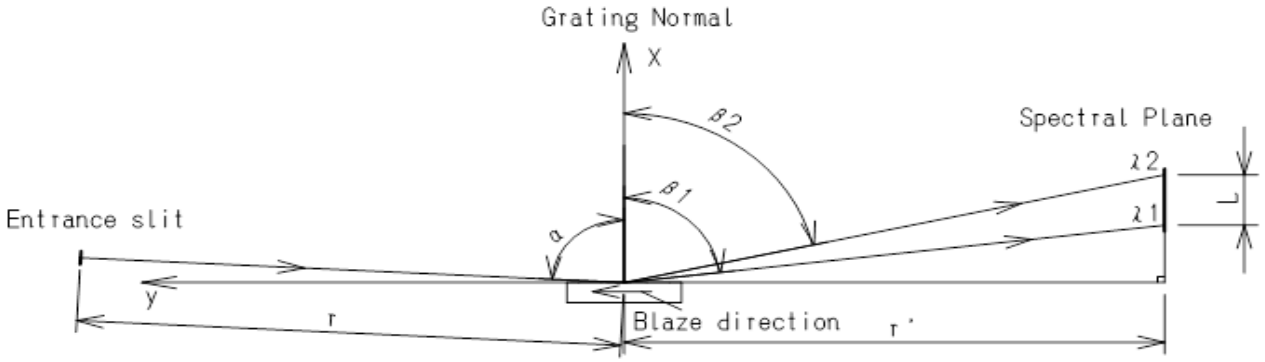

Figure 20: a schematic of a flat field XUV grating used in these work (picture taken from Hitachi-001-0639 grating system manual)

The Semi-Infinite Gas Cell (SIGC) is an experimental device used to produce high-order harmonics. Semi-Infinite mean that there is an area filled with gas and another area where is at high vacuum separated by a small laser driven pinhole. The geometry of the SIGC, allows the generation of laser harmonics in the region of the XUV part of the radiation spectrum in the exit pinhole of the gas-filled area. The gas (typically noble gas) pressure is controlled by a needle valve. The femtosecond laser beam enters the cell through an entrance window which is at Bruster angle for the 800 nm after passing through a converging lens (f=35 mm) in order to focus inside the cell (typically at the exit pinhole of the SIGC). The XUV harmonic radiation comes out the gas filled area along with the fundamental laser beam. After their production the harmonic radiation and the fundamental laser field propagate in the vacuum area. Note here that the laser beam is appropriately formed passing through a round diaphragm, the diameter of which can be controlled. Typically, apertures of 8 mm diameter shown the best phase matching focusing condition for the gas pressures and the focusing lens used in this experiment. The XUV light is filtered from the IR using a pair of Si wafers placed at Brewster angle for the IR. The remaining of the XUV comb of high harmonics is diffracted by grazing-incidence flat-field diffraction grating (Hitachi 001-0639) allowing for high angular dispersion efficiency for the harmonics from 22 nm –124 nm. The XUV light is detected at the focal plane of the harmonics in interest (15ω–23ω) using a high quantum efficiency 16-bit x-ray vacuum CCD camera (Raptor Photonics, Eagle XO) with a sensor having 2048 pixels (27.65 mm) at the grating diffraction axis and 548 pixels (6.90 mm) at the XUV divergence axis (perpendicular to the grading diffraction axis). The value and the sign of the chirp of the laser pulses are controlled by tuning the compressor gratings of the laser amplifier relative to the position that yields FTL laser pulses of 26 fs duration. For positive chirp values the lower frequencies appear at

the leading edge of the laser pulse, while for negative chirp values the lower frequencies appear at the trailing edge of the laser pulse (see Fig. 1a). Assuming only linear chirp, its value is experimentally measured in shot-to-shot basis via a femtosecond single shot intensity autocorrelator (Amplitude, Bonsai) just before the interaction cell. The distance of the gratings in the laser compressor can be tuned according to the measured pulse durations and thus the laser pulse chirp is fully controlled during the experiments.
The intensity autocorrelation method used is based on the registration of cross distribution of Second Harmonic (SH) energy produced in nonlinear crystal under non-collinear interaction of two beams with determined aperture.

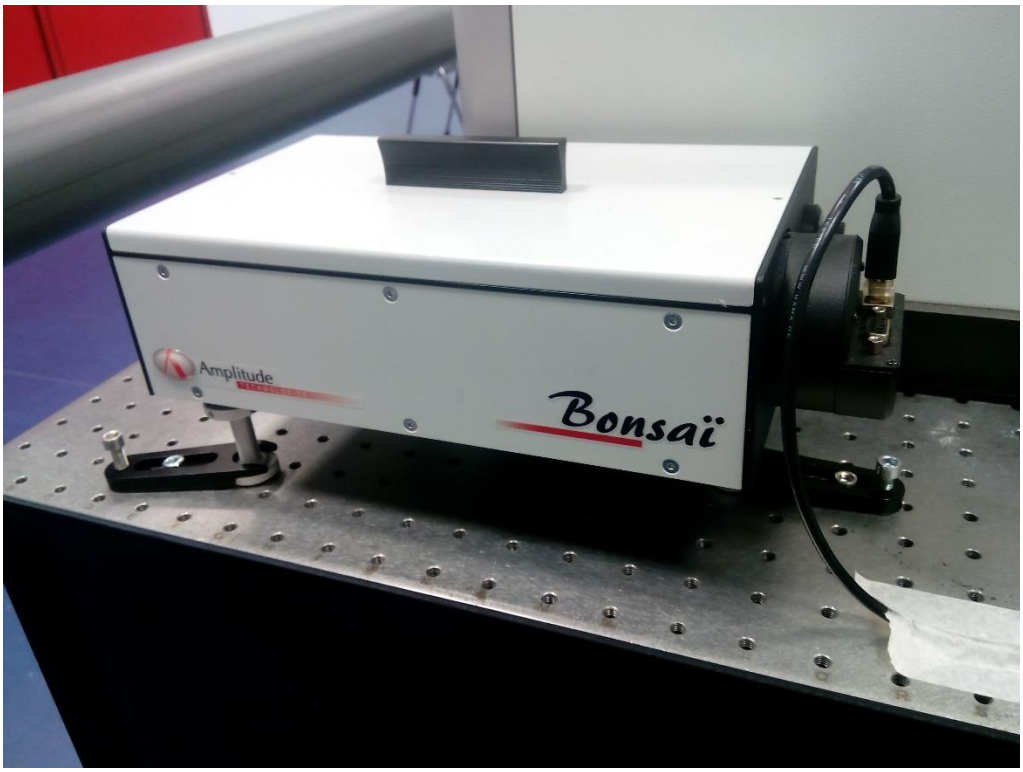

Figure 21: Bonsai® autocorrelation system image utilized in the HHG experiment

More specifically the experimental procedure we employed, using the instruments previously described, unfolded as follows: the femtosecond laser pulses, produced from our laser system with energy per pulse of ~1mJ and a duration of ~26 fs (FTL pulses), are propagated with the assistance of the appropriate optics (mirrors and irises). Then the initially 1.7 cm laser diameter is apertured down to 0.8 cm and focused at the exit pinhole of the semi-infinite cell at a spot with diameter estimated 60-100 μm depending of the nature of gas and its pressure. The focus lens is properly thin so that it does not broaden the duration of the laser pulse to the point that it affects our experiment and is located near the window (thin suitable window by Fused Silica) near the small chamber of the jet, in order not to create non-linear phenomena (e.g self-phase modulation), which may destroy the temporal characteristics of our laser pulse. The lens can also be moved to the three dimensions with the help of a three-dimensional micrometric system and thus we are able to focus the laser beam at the exact point we need inside the semi-infinite cell. The laser beam then crosses inside the chamber and interacts with the noble gas generating an observed plasma plume over the parallel plane (this plume is observable by both the eye and by a CCD camera) as well as the high harmonic radiation. The high harmonic light, showed in this thesis, is generated by the interaction

of the aforementioned laser pulses with Argon gas (Ar). The high harmonic field enter together with the laser radiation into a second vacuum chamber from a very small hole. Inside this chamber which exhibits a high-vacuum, the silicon reflectors (Si) are located, as well as the X-ray CCD camera. Initially the high harmonics, as well as the fundamental laser beam fall on the Silicon wafer, which is essentially a mirror made with semiconductor materials such as silicon and has a semiconducting surface on which the reflection occurs. In our experiment, the placement of Si-wafers was in Brewster angle in order to ensure the severe absorption of the infrared radiation (which corresponds to the laser field). Thus, the silicon wafers eliminated the laser radiation, and then reflected the harmonic radiation with acceptable percentage (~25%). So, it acts like an IR filter and XUV reflector. Then the harmonic radiation falls on an appropriate flat field concave grating and is diffracted on the XUV camera with its CCD located exactly at the flat-field plane for the measured wavelengths. The XUV camera is controlled by a computer through a commercial software, (in which we select the time frame in which the sensor will collect light generating an image which is then taken). Finally, the pictures of the harmonic spectrum as well as images of the plasma are collected from a computer system. The XUV camera is typically working in -40K degrees in order to snap pictures of the harmonic spectrum, by collecting the harmonic radiation (with high quantum efficiency) by averaging over certain number of (set through the computer software) laser pulses. The pictures of the harmonic spectrum collected by the XUV camera is then processed with the help of a computer program called IMAGEJ. Using this freeware program, we are able to analyze the pictures of our cameras for both the plasma radiation and the harmonic spectrum (file->open->image->stuck->analyze->tools->RO->multi plot). This way we can create the results, which we will present in the next chapter.

Finally, chirp is inserted in the propagating laser field pulses though the air compressor of our laser system. The procedure unfolds as follows: the compressor consists of a pair of gratings, by alternating the distance in between those gratings we are able to compress or decompress our pulses. Hence by employing the same principles of pulse compression we can regulate the chirp of the pulse via the change of the grating distance. (taking of course into account that the pulse exhibits some chirp from the laser field propagation which must be compensated appropriately). This way we are able to create pulses with different chirp values, as well as different chirp signs.

Figure 22: The ZEUS laser system part of it utilized in our experiments

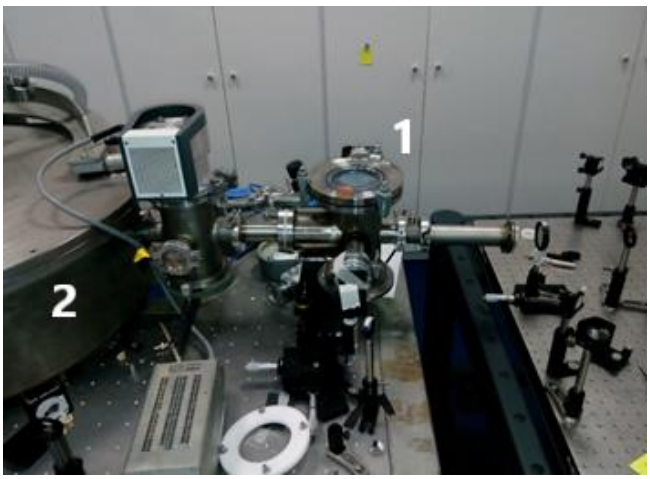

Figure 23: in the figure we see the small chamber (1) in which plasma is created through the interaction of the laser beam with the gas. In this cell the high harmonic radiation is generated, and then is directed inside the big chamber (2), where is diffracted from the grating and the collected by the XUV camera.

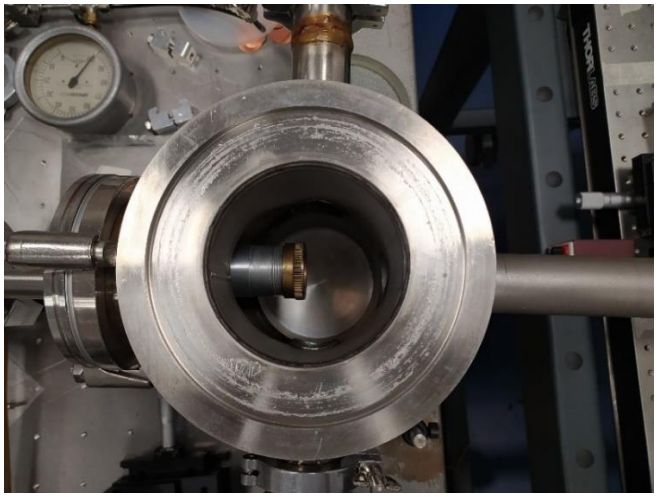

Figure 24: the inside of the first vacuum chamber, where the plasma is created.

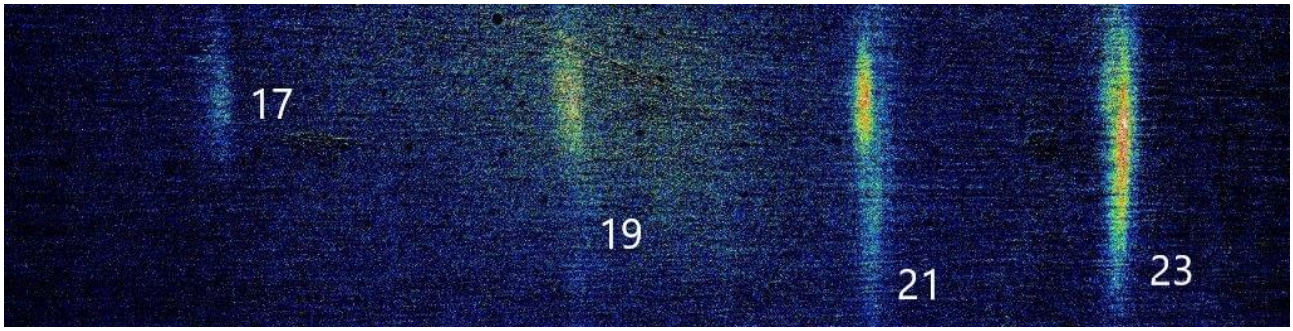

Figure 25: typical spectrum of high harmonics taken from the XUV camera after diffraction from Hitachi flat field grating using high intensity Ti:Sa laser, that ionized the Ar atomic target, the numbers indicate the different order harmonics

3. EXPERIMENTAL RESULTS AND ANALYSIS

4.1 INTRODUCTION TO DATA ANALYSIS

In this chapter we will present the data collected in our experiments for the generation of high harmonic radiation from Ar gas. The important parameter is the variation of the chirp of the femtosecond laser pulse and the systematic study of the consequences it has on the HHG spectrum and its characteristics. The data were collected from the XUV camera. Those data consisted of images of the plasma bubble created from the interaction of the intense laser electromagnetic field and neutral Ar gas plume. As well as images of the high harmonic radiation emitted from the nonlinear processes described by the three-step model. Those images were taken from the XUV camera with the assistance of a computer program. With this computer program we were able to control the imaging procedure, setting various parameters such us the exposure time and the delay. Images were taken for various chirp parameters ranging from -150 fs to +150 fs and different pressures ranging from 30 to 90 torr and for Ar gas. The chirp parameter was controlled via the grating system inside the compressor. The quantity of gas inside the chamber was maintained in the appropriate levels and in the appropriate pressure via a simple mechanism. Other parameters such as laser intensity and iris radius were optimized for maximum high harmonic generation efficiency. The chirp parameter was determined from the equation [51]:

$$b(t) = \pm \frac{4ln2}{t^2} \sqrt{\frac{t^2}{t_{ftl}^2} - 1} \tag{47}$$

Where t is the pulse duration and t_{ftl} is the Fourier limited pulse duration.

The high harmonic spectra presented in fig.36 and fig.37 were derived from the corresponding images taken with the XUV camera, via integration of a number of laser shots. The process was done in the program ImageJ and constituted of the calibration of brightness and smoothness of the images and then the execution of an intensity integration that lead to the plots presented at the first column of those figures. The vertical axis of those plots corresponds to intensity in A.U and the x axis is calibrated to show harmonic orders. The calibration of the x axis was done according to the relation:

$$1 \text{ pixel} = 14/512 \text{nm} \tag{48}$$

We also know that harmonic peaks in the spectrum are denser as the harmonic order increases. Also, the position in nm of each harmonic is derived from the formula:

$$q_{harmonic} = \frac{\lambda_{cw}}{\lambda_q} \tag{49}$$

Where the *q* harmonic order is determined by dividing the central wavelength (805nm) with the qth wavelength. From eq.49 we are able to determine the order of the harmonics, shown in the spectra.

Typical experimental spectra of HHG in the plateau harmonic region around 15-23 ω have been presented on Fig. 35 for various Ar pressures inside the Semi-infinite Cell. It is clear that the HHG spectra depends strongly on the variation of the chirp of the fundamental radiation and of course on the Ar-pressure. In the following chapter we will try to understand and analyze some of the main findings of this behavior.

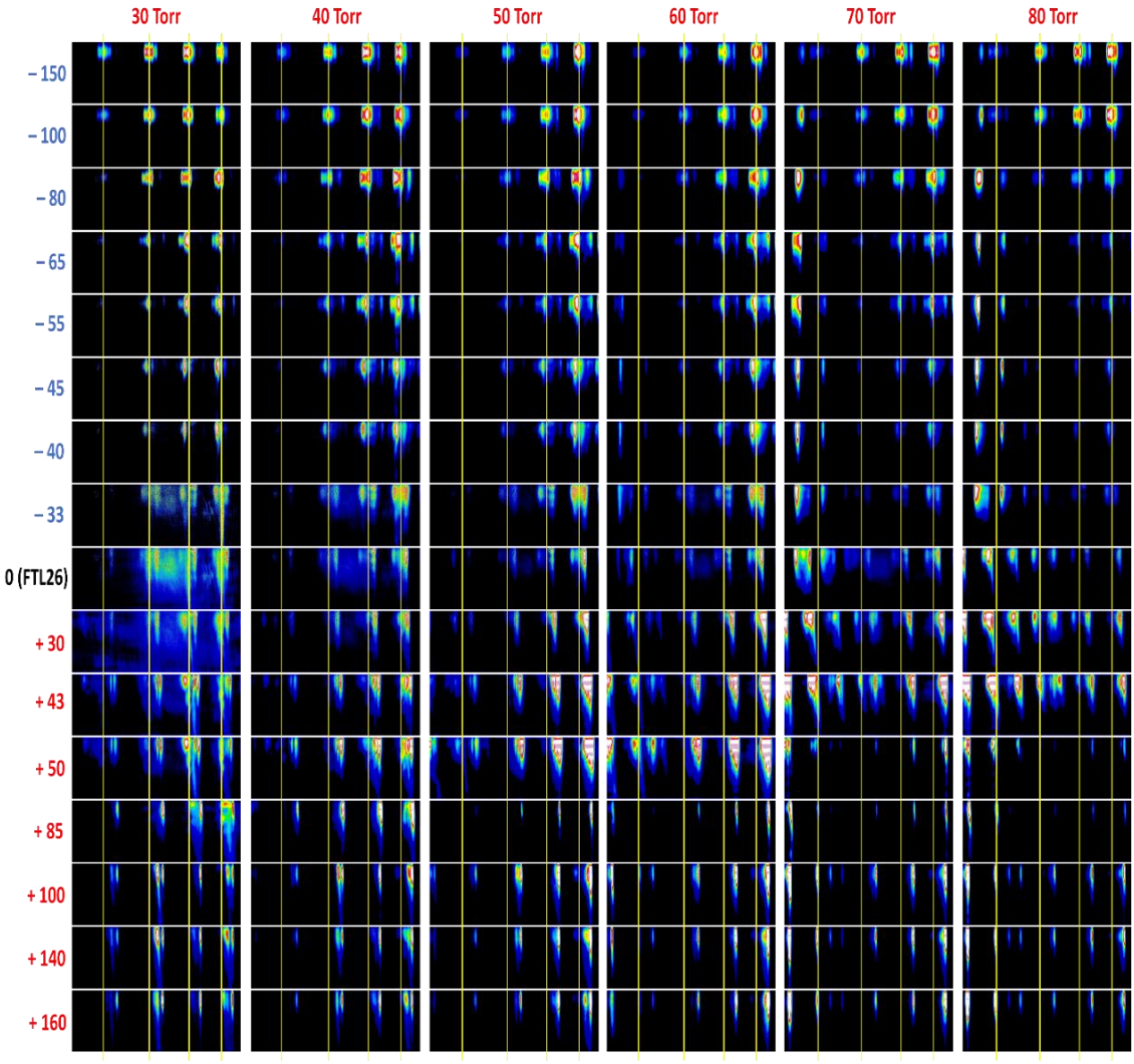

Figure 35: HHG spectra taken for different laser chirps at different Ar gas pressures in the semi-infinite cell. The 15th, 17th, 19th, 21st harmonic is shown.

In the second column of the fig.36, fig.37, fig.38 we present selected images of the harmonic spectra. The selection was done, considering which of the images taken with the XUV camera were the optimum. Additionally, the analysis was done for the 40,60,80 torr pressures, in order to demonstrate in a more robust way the effects of the chirp parameter on the high harmonic spectra.

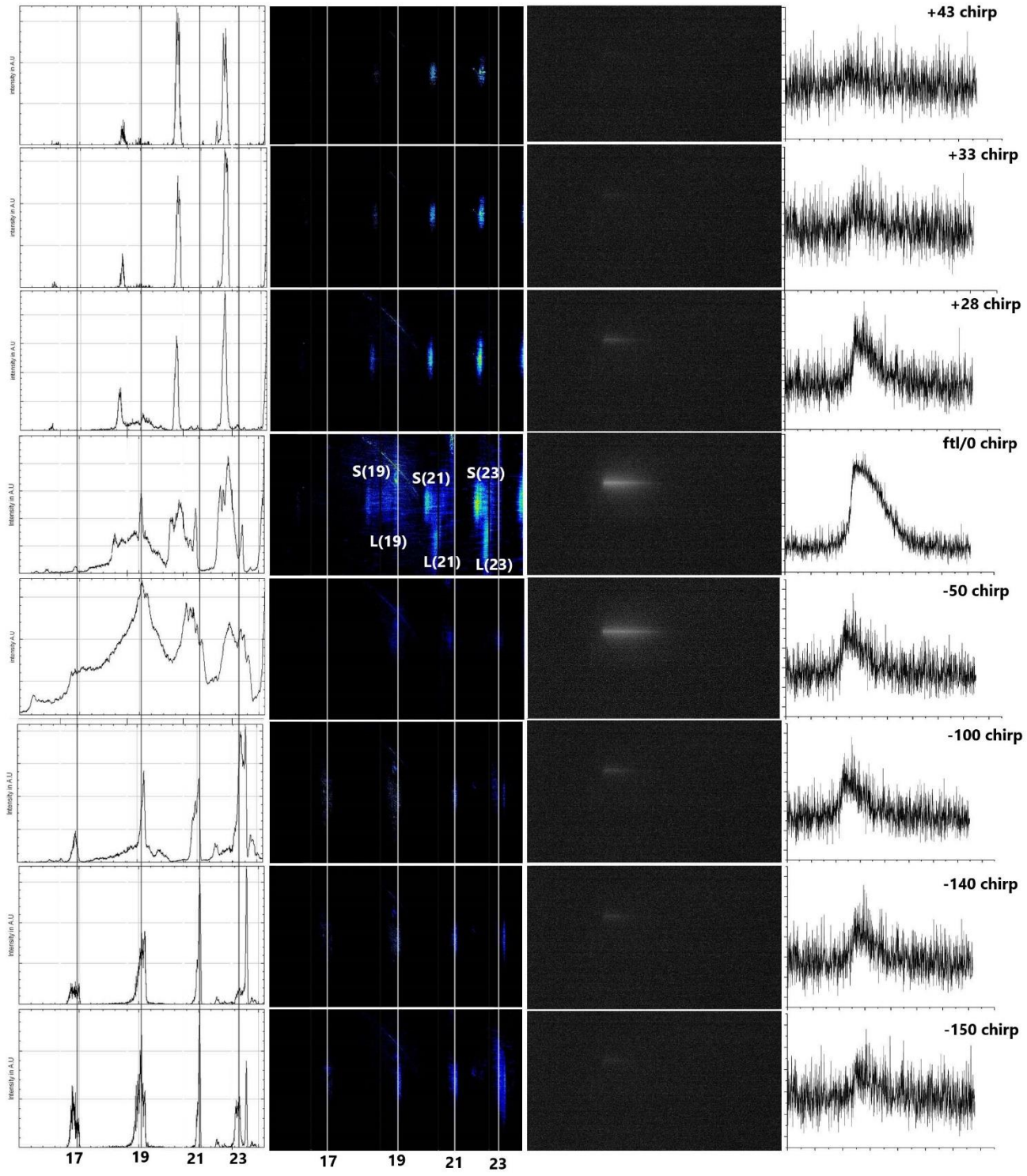

Figure 36: comparison of the different data collected from analysis for 40 torr Ar gas pressure. The first column represents the high harmonic spectrum, where the 17^{th}, 19^{th}, 21^{st}, 23^{rd} harmonic peaks are observed. In some cases, as in -50 fs chirp, a lot of spectral broadening is observed. The absence of clear peaks for the harmonic, is a result of quantum interference. The second column, represents the received images from the XUV camera (the images had undertaken some noise reduction and signal enhancement editing), where the same harmonics as in the first row are observed. Different absorption phenomena result in the loss of the long trajectory in most of the different chirp cases. The third column represents the pictures of the plasma luminescence taken with our XUV camera. Finally, the last row represents the integrated along the horizontal axis, plasma luminesce signal. Clearly, for zero chirp plasma luminesce is the highest.

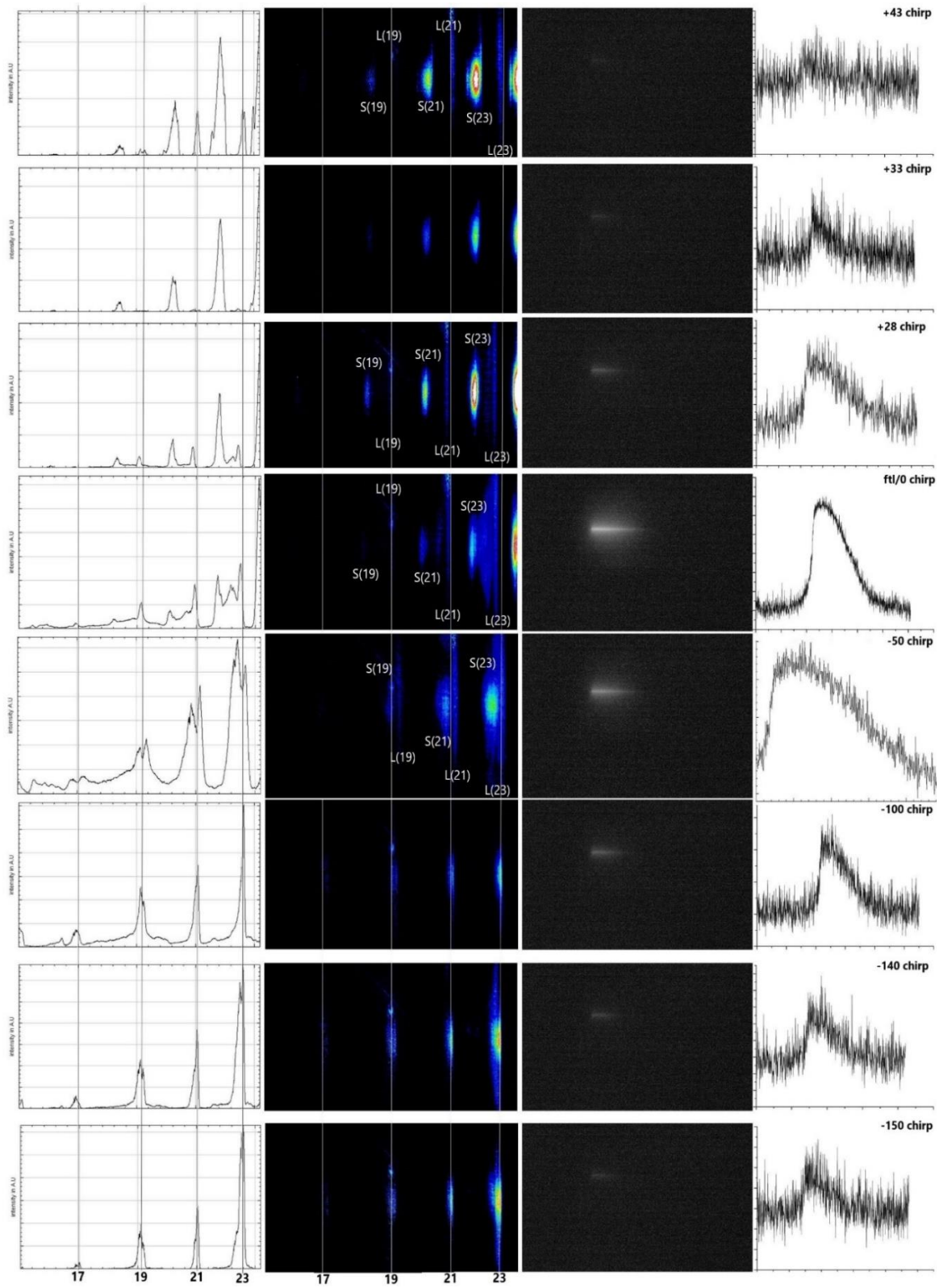

Figure 37: comparison of the different data collected from analysis for 60 torr Ar gas pressure. The first column represents the high harmonic spectrum, where the 17th, 19th, 21st, 23rd harmonic peaks are observed. In some cases, as in -50 fs (although less than in 40 torr data) chirp, a lot of spectral broadening is observed. The absence of clear peaks for the harmonic, is a result of quantum interference. The second column, represents the received images from the XUV camera (the images had undertaken some noise reduction and signal enhancement editing), where the same harmonics as in the first row are observed. Different absorption phenomena result in the loss of the long trajectory in some of the different chirp cases. The third column represents the pictures of the plasma luminescence taken with our XUV camera. Finally, the last row represents the integrated along the horizontal axis, plasma luminesce signal. Clearly, for zero chirp plasma luminesce is the highest, although in -50 and -100 fs pulses, the luminescence is comparatively high.

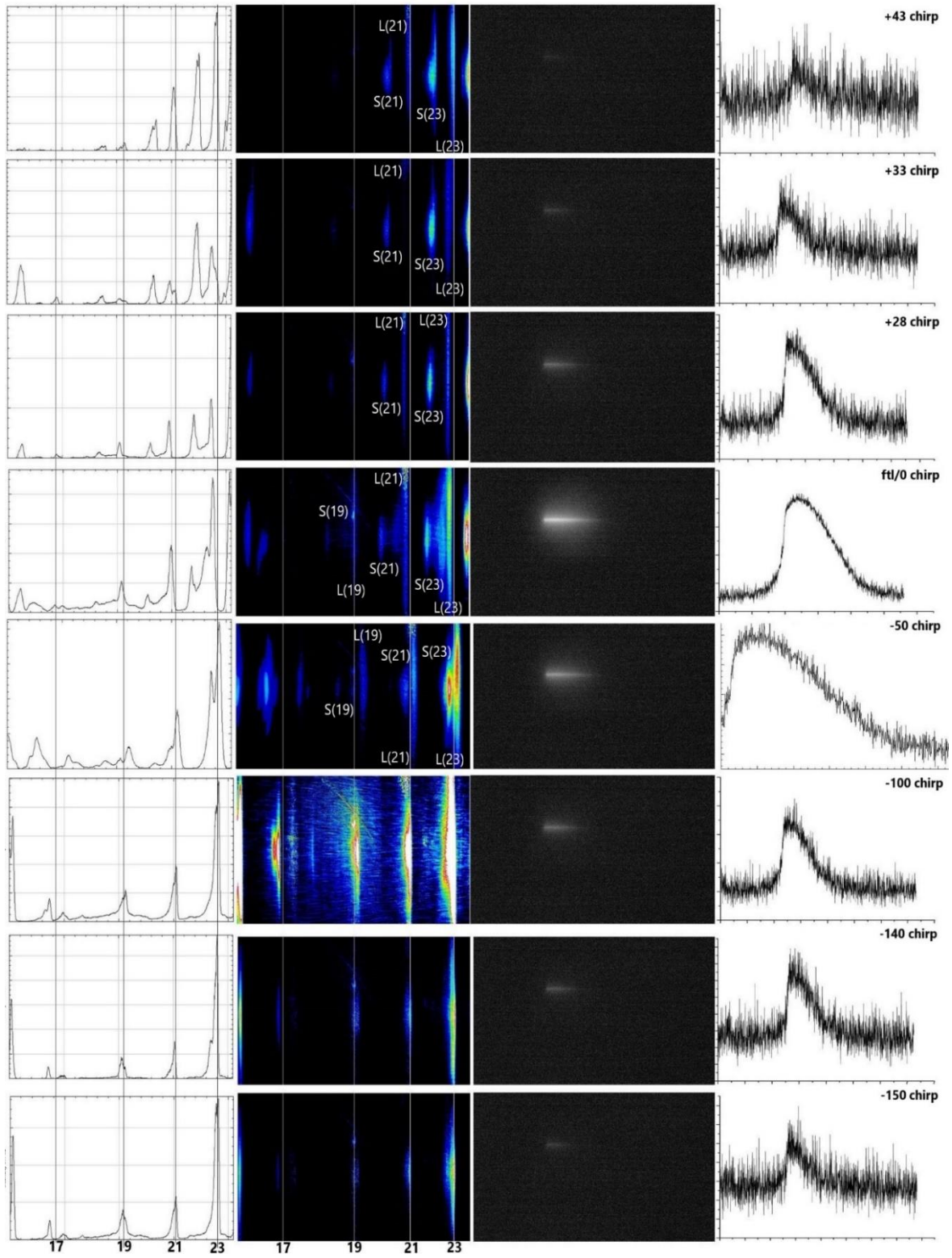

Figure 38: comparison of the different data collected from analysis for 80 torr Ar gas pressure. The first column represents the high harmonic spectrum, where the 17th, 19th, 21st, 23rd harmonic peaks are observed. In some cases, as in -50 fs (although less than in 40 torr data) chirp, a lot of spectral broadening is observed. The absence of clear peaks for the harmonic, is a result of quantum interference. The second column, represents the received images from the XUV camera (the images had undertaken some noise reduction and signal enhancement editing), where the same harmonics as in the first row are observed. Different absorption phenomena result in the loss of the long trajectory in some of the different chirp cases. The third column represents the pictures of the plasma luminescence taken with our XUV camera. Finally, the last row represents the integrated along the horizontal axis, plasma luminesce signal. Clearly, for zero chirp plasma luminesce is the highest, although in -50, -100 and +28 fs pulses, the luminescence is comparatively high.

The first column of fig.37, fig.37, fig. 36 represents the harmonic spectra derived from the images of the second column, in the corresponding figures. Each peak is generated from the coherent summation of the two quantum paths. Those quantum paths are the long and short trajectory. Eq.49 allows us to determine the order of each harmonic shown in the spectra, from the same equation we see that the harmonic order decreases as the wavelength increases. The peaks of the harmonic spectra are not clear, due to quantum interference phenomena, this is due to the different constructive and destructive interference patterns of the short and long trajectory. Additionally, we observe a broadening of the harmonic peaks for the cases that the plasma is denser (higher laser intensities, low chirp value), due to the contribution of various ionization processes, with different propability amplitudes.

The intensity of each peak is determined by the combination of the diffraction efficiency of the grating system and the transmission propability of the generated harmonic radiation. At the range of 48-34 nm (as shown in fig.42), the diffraction efficiency is high. This efficiency signifies that only a small fracture of the harmonic radiation intensity is absorbed, with the larger part being diffracted and consequently imaged. Maximum diffraction efficiency is at the blazing wavelength of 33nm. Additionally, for all the selected pressures (as shown fig.40, fig.41 and fig.39) the transmission propability rises as the wavelength decreases. That means that after the high harmonic radiation is generated, the higher the photon energy (higher harmonic order) of each harmonic, the most probable is to be efficiently transmitted through Ar gas. Specifically, for the 15th, 17th, 19th 21st and 23rd harmonics the transmission propability is high. Those two factors explain the decrease of the intensity of the harmonics as the wavelength increases, observed in the experimental spectra.

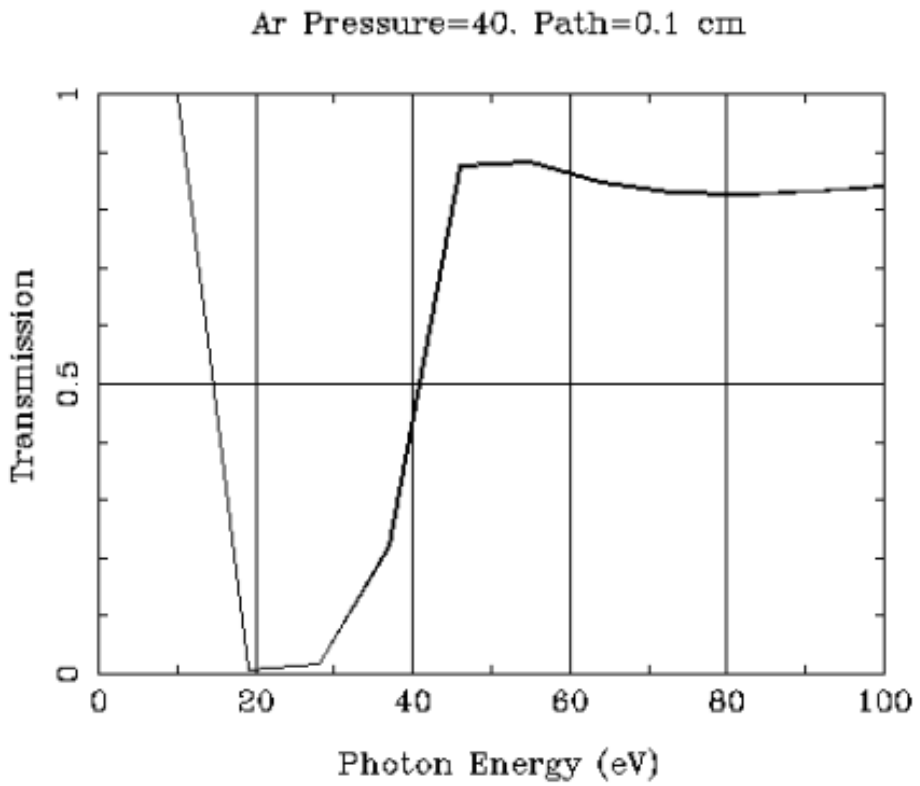

Figure 39: XUV Transmission probability vs photon energy for 40 Torr Argon gas calculated by HENKE (https://henke.lbl.gov/optical_constants/gastrn2.html). The graphs show that for photon energy lower that 18 eV the Argon gas is practically transparent. For around 18-30 eV argon absorbs the correspond photons with very high efficiency, for higher photon energies the transmission probability rises and stabilizes around 80%.

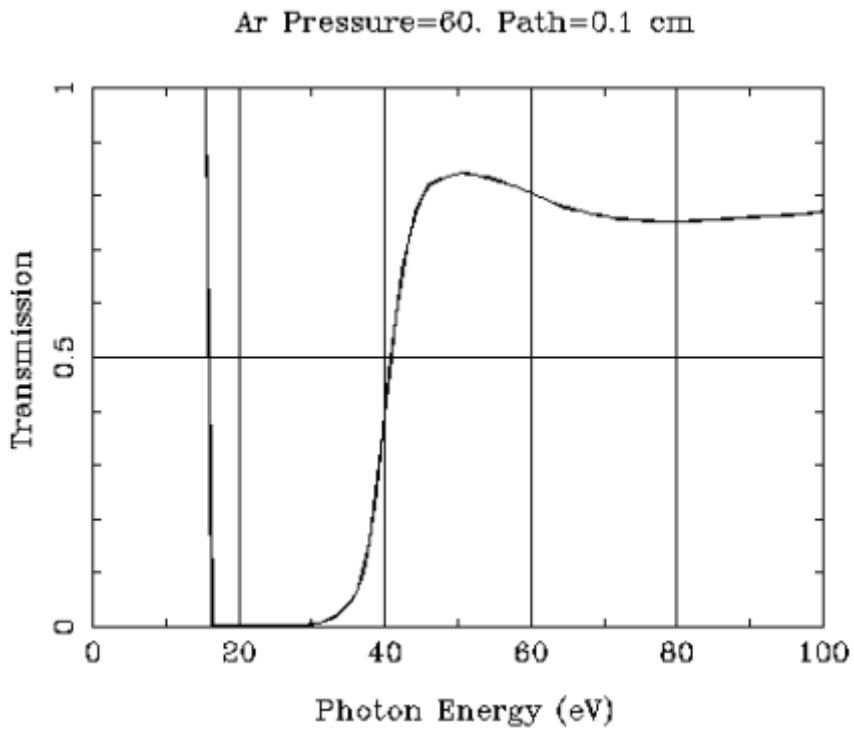

Figure 40: XUV Transmission probability vs photon energy for 60 Torr Argon gas calculated by HENKE (https://henke.lbl.gov/optical_constants/gastrn2.html). The graphs show that for photon energy lower that 18 eV the Argon gas is practically transparent. For around 18-30 eV argon absorbs the correspond photons with high efficiency, for higher photon energies the transmission probability rises and stabilizes around 80% and for 50 ev photons.

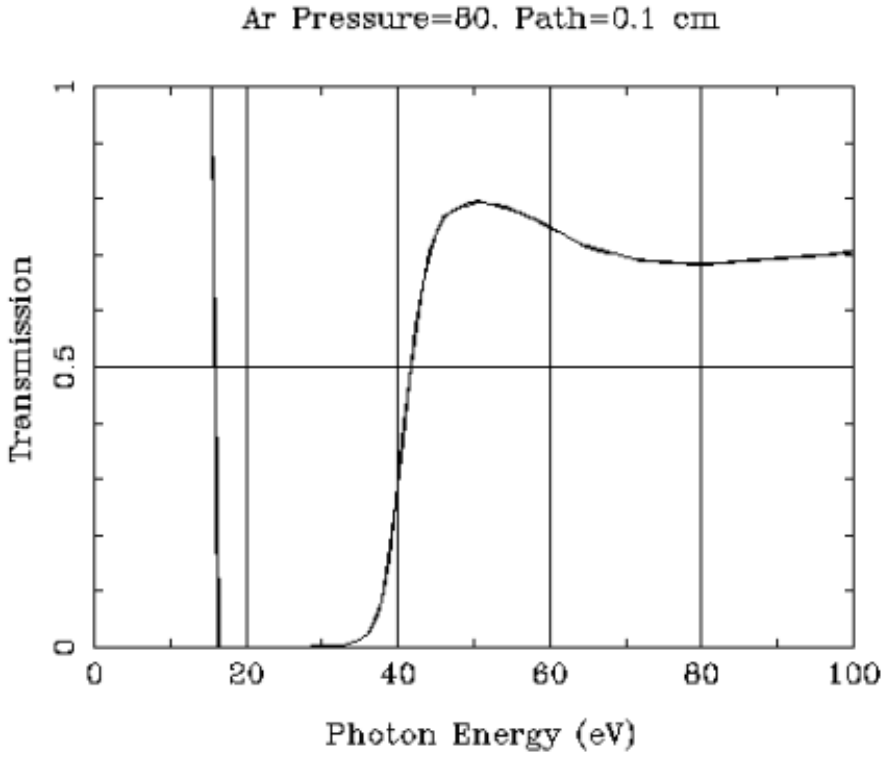

Figure 41: XUV Transmission probability vs photon energy for 80 Torr Argon gas calculated by HENKE (https://henke.lbl.gov/optical_constants/gastrn2.html). The graphs show that for photon energy lower that 18 eV the Argon gas is practically transparent. For around 18-30 eV argon absorbs the correspond photons with high efficiency, for higher photon energies the transmission probability rises and stabilizes around 70%, with a peak transmissibility at around 50 ev, with 80% propability.

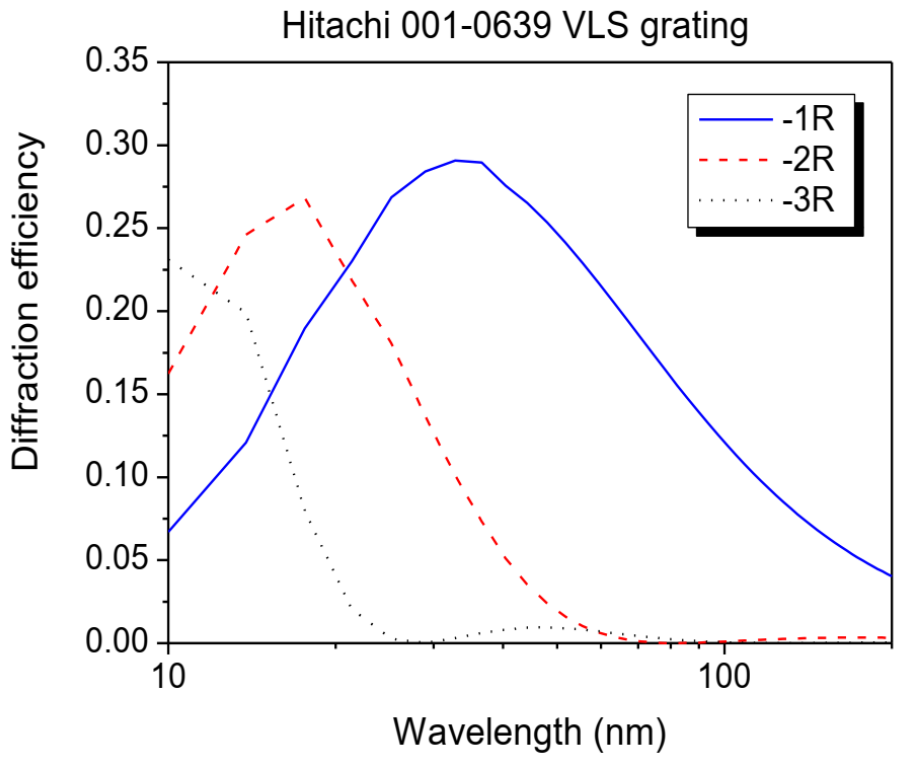

Figure 42: in the figure the grating diffraction efficiency for first (blue) second (red) and third (green) diffraction order is demonstrated, showing that the efficiency increases as the wavelength decreases until it reaches a maximum and then it falls as the wavelength goes up, as well as that the maximum efficiency is around 30 nm. (Hitachi grating manual)

In the third column of fig.36, fig.37 and fig.38 images of the plasma is presented. Plasma is created when the laser beam interacts with the Ar gas inside the infinite cell, resulting in the ionization of the gas. This ionization leads to the emittance of electrons from the parent Ar atoms to the continuum of the field. The recombination of those electrons with the parent atoms generate radiation, which demonstrates its self as luminescence in the images received with the XUV camera (this process is analytically explained with the three-step model). Plotting the plasma luminesce (in A.U) of this radiation as a function of the distance (in pixels) in the semi-infinite cell and then integrating the whole area inside the plot, we derive the total plasma luminescence in arbitrary units of radiation. These calculations were executed initially in the image j program, where the plots were created. Afterwards those plots were inserted into the origin program, had their background noise removed and finally were integrated yielding the total plasma luminescence.

Then by plotting the graphs of the calculated plasma luminescence as a function of the corresponding chirp values, we make some interesting and logical observations.

What we observe from those figures (fig.37 and fig.38 and fig 36) is that for the zero chirp (ftl) the plasma density (which is related linearly with the plasma luminescence) is the highest. This is due to the fact that the intensity of the laser beam is inversely related to the duration of the pulse. So, by increasing the duration of the pulse vie the insertions of chirp, we reduce the laser peak intensity. Therefore, the ionization rate of Ar gas is lower and the plasma electron density is also lower. This situation leads to lower electron recombination rate; thus, the high harmonic generation is less profound. Finally, it should be noted that the intensity is the same for negative and positive chirp

values. The following equation, mathematically quantifies the relation between the intensity and the pulse duration.

$$I(t) = I_0 e^{-(2\frac{t^2}{tg^2})} \quad (50)$$

Where, I(t) is the time dependant peak intensity, and t is the duration of the pulse.

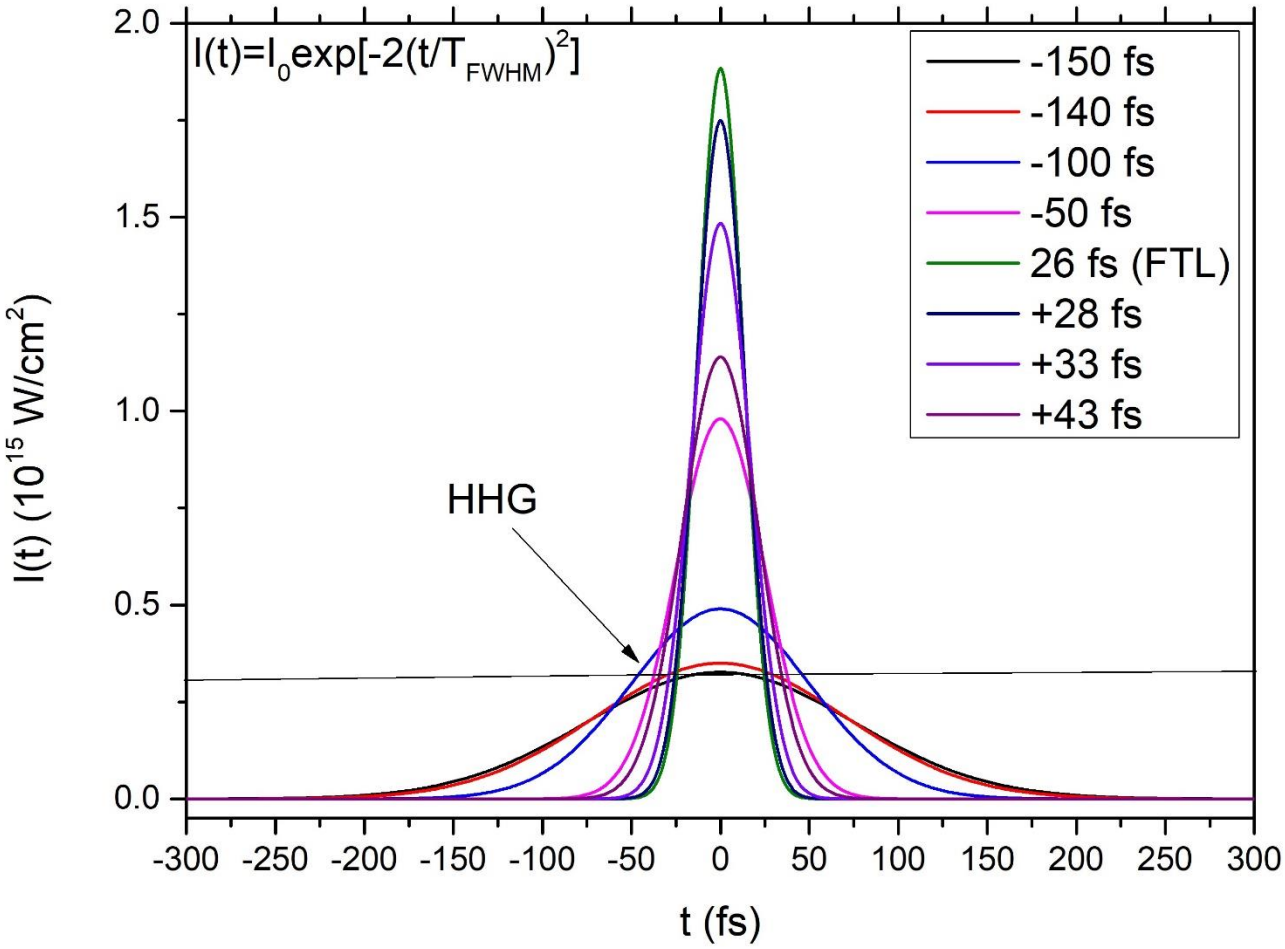

Figure 43: plot of the laser pulse intensity as a function of the laser pulse duration (t) for different chirp values (including the 0 chirp FTL). The black horizontal line indicates the position in laser intensity where the High harmonic generation takes place, which is the leading edge of the pulse.

High harmonic generation happens until the Ar gas is completely ionized. The maximum HHG efficiency is expected at intermediate laser intensities where the laser electric field is high enough but at the same time about 50% on the Argon atoms in the interaction region remain non-ionized. For the laser intensity estimated in our experiments the HHG took place mostly in the leading edge of the pulses and as shown in the Fig. 43. For higher energies the gas is fully ionized and does not generate high harmonic radiation and for lower energies, ionization cannot happen efficiently, although some ionization may happen through different ionization processes like multiphoton or even tunnelling. For the above analysis is clear why the chirp value of a laser pulses should play an important role on HHG spectrum and efficiency.

Several plots of the plasma luminescence as a function of the laser pulse duration and for different chirp values were created. Those plots were created in the origin lab computer program.

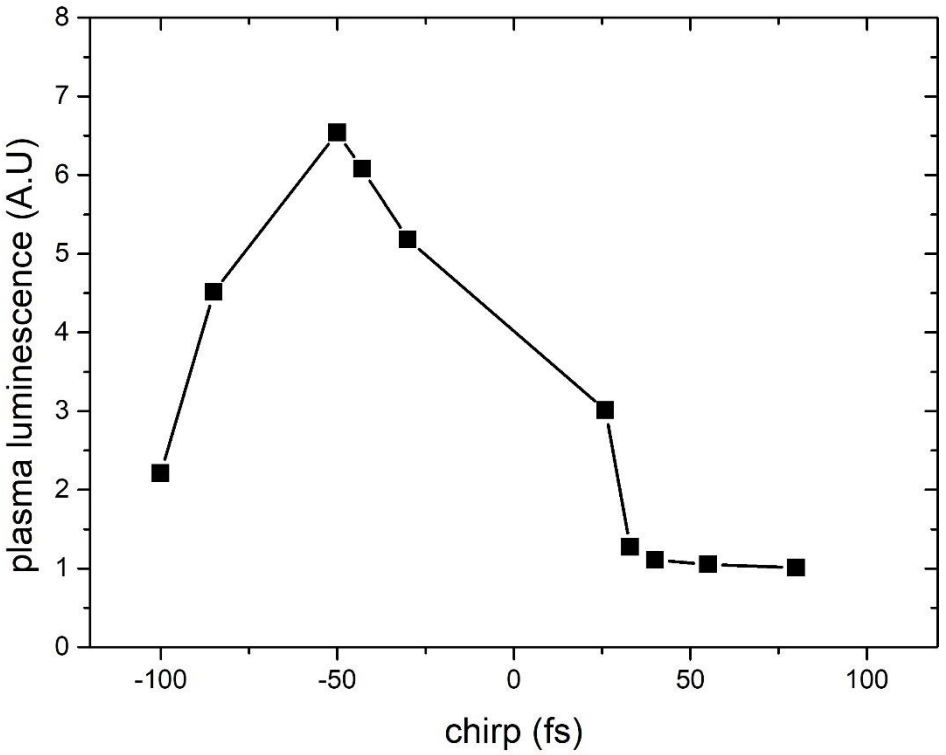

Figure 44: Integrated Plasma luminescence for 40 torr Ar pressure as a function of laser chirp, where the increase of the luminescence parameter as the chirp decreases is observed. Peak luminesce is reached for the -50 fs chirped pulse. For positive chirp we observe a rapid decrease of the plasma luminescence. For positive chirp plasma luminescence is generally lower than the negative chirp values.

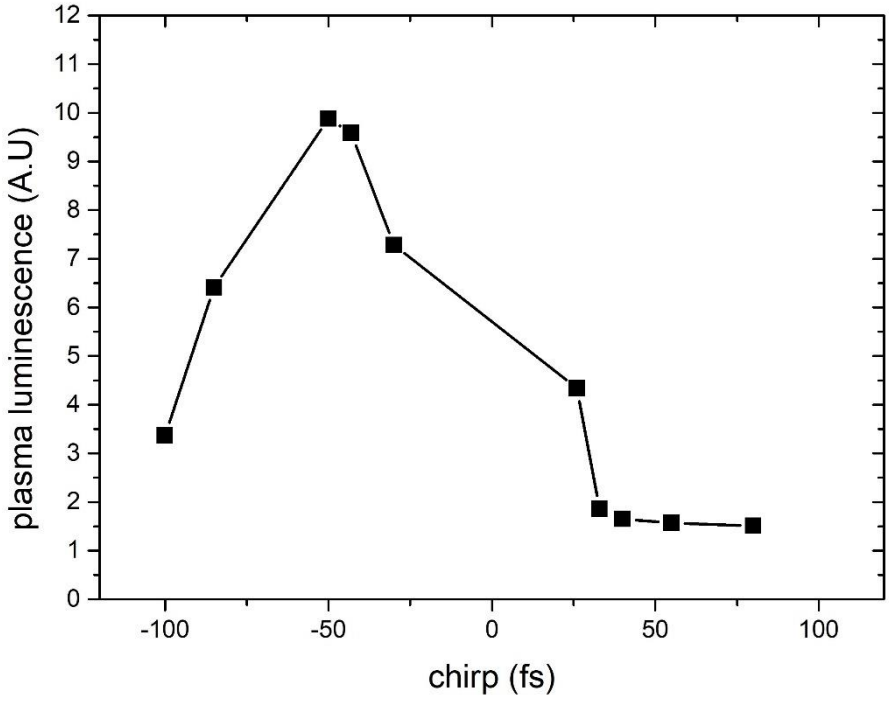

Figure 45: Integrated Plasma luminescence for 60 torr Ar pressure as a function of laser chirp, where the slow increase of the luminescence parameter as the chirp decreases is observed. Peak luminesce is reached for the -50 fs chirped pulse. For positive chirp we observe a rapid decrease of the plasma luminescence. For positive chirp plasma luminescence is generally lower than the negative chirp values.

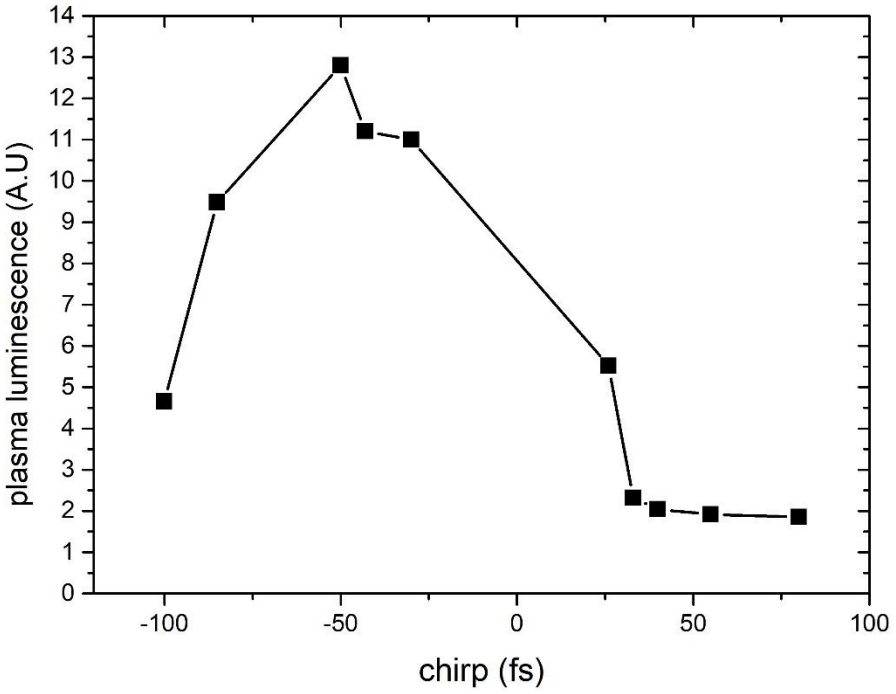

Figure 46*:* Integrated Plasma luminescence for 80 torr Ar pressure as a function of laser chirp, where the increase of the luminescence parameter as the chirp decreases is observed. Peak luminesce is reached for around -50 fs chirped pulse. For positive chirp we observe a rapid decrease of the plasma luminescence. For positive chirp plasma luminescence is generally lower than the negative chirp values.

The plots of plasma luminescence as a function of chirp (fig.46, fig.45, fig.44) clearly indicate that as we decrease the value of the negative chirp parameter, the plasma luminescence increases. This clear increase of the luminescence turns to a rapid increase as we approach the unchirped pulse and then it rapidly falls for the positive chirp values. Maximum plasma luminescence is always observed for the -50 fs pulse. In whole for positive chirp values plasma luminescence is lower. This behaviour seems to be independent of the Ar pressure, although as we increase the pressure the magnitude of plasma luminescence increases for the same chirp value.

The low plasma density observed for the negative and positive chirped parameters can be explained by the widened pulse (due to the induction of the chirp parameter), which implies low laser intensity and ionization rate. As we decrease the absolute value of the chirp parameter of the pulse, its intensity gets higher therefore plasma luminescence increases. Peak luminesce is achieved for the -50 fs and not for the expected FTL. This behaviour is explained by the fact that the SPM induced by propagation and the interaction with the neutral atoms induces a positive chirp to the pulse, so in order for this to be compensated and an FTL pulse to materialize, a small shift to the negative chirp values is needed.

Finally, the observed lower plasma density for positively chirped pulses, in comparison with negatively chirped pulses, can be explained from the fact that a negatively chirped pulse has the higher frequencies in the leading edge (where the harmonics are mostly generated) and therefore it ionizes the medium (creating plasma) more powerfully, than the positively chirp values (we assume that the trailing part of the pulse plays no role in the HHG process.

4.2 ANALYSIS OF SPECTRAL SPLITING

In this chapter we will discuss some interesting phenomena that appear in the HH spectra for the various laser chirp values. One of them is the spectral splitting of the harmonic spectrum due to different factors. Specifically, we will analyse the splitting of the 21 and 23 harmonics, which were imaged the clearest in our data, for40, 60 and 80 Torr Argon pressures. The data for those pressures where the most proper for our analysis in terms of quality.

The splitting of the harmonics was attributed to the different quantum paths corresponding to each harmonic order. Those different quantum paths coherent addition generates the harmonic. So, if for some reason this coherence is disturbed or a path is suppressed, a split in the harmonic is observed [47]. This is due to the fact that each path experiences different interaction length inside the ionized medium, and therefore acquire different phase. As shown by Salieres et al [45], Papadogiannis et al [paper with Balcou], Wilner et al (PRL and NJP) and Antoine et al [46] the phase matching conditions for those different quantum paths are different (based on the different focusing geometry) resulting in the suppression of the one path and the other to be amplified. [41]

In the second row of the fig.36, fig.37 and fig.38 we present the images (taken with the XUV camera) of the harmonic spectra, from which our analysis on the splitting will derive. We calculated from the known position of the camera on the perpendicular plane, the order of those harmonics. Specifically, by knowing the exact positions of each harmonic on the vertical axis after the diffraction from the grating and the position of the camera on this vertical axis we determine the harmonic order we see (23-17 harmonic). The images were edited in ImageJ program in order to eliminate the background noise. After that we were able to observe the harmonic splitting, and determine the short and long trajectory of each harmonic order. In the images we were able to determine the long and short trajectory for each harmonic order, although some times the long trajectory was vanished, as a result of destructive interference. Finally, the trajectory for the 15^{th} and 17^{th} order harmonic was not used in our analysis as a result of the strong absorption from Ar gas, which lead to their insufficiently good imaging.

After selecting the appropriate harmonic order (specifically the 21^{st} and 23^{rd}), we measured the distance between the long and short trajectory for each harmonic order and the harmonic position respectively. The unperturbed harmonic position was chosen to be the position of the harmonics for -150 chirp, due to the fact that in reality this is the correct position of the unsplitted harmonics because the negative chirp, we introduced, was able to compensate the positive chirp induced by our apparatus and the propagation of the laser beam inside the plasma. Additionally, the laser intensity is relatively low so no significant plasma blue shifting is appeared. Furthermore, the position of the harmonic for each chirp is taken to be the short trajectory position, because of the fact that the long trajectories (long quantum paths) are the most sensitive in spectral shifting due to the longer interaction with the plasma.

Single atom response induces a blue shift in the harmonic, related to the phase and intensity as shown in (eq.52) and (eq.53). [48] This blueshift induced to the harmonic spectrum from atoms in a rapidly increasing laser field can be calculated using a semiclassical model theory based on the SFA model. [4] [49] In general, the harmonic blueshift Δω increases as the pulse width decreases. [47]

$$\Delta\omega = \frac{\partial \Phi}{\partial I}\frac{\partial I}{\partial t} \tag{51}$$

$$\varphi_L = -a_L I(t) \tag{52}$$

$$\varphi_s = -a_s I(t) \tag{53}$$

Eq.52 and eq.53 relate the phase accumulated through propagation of each trajectory inside the medium, because $a_L >> a_s$ (L is for the long and S for the short trajectory) the long trajectories are more strongly dependant on the laser intensity, therefore they are generally blue shifted from the atomic dipole phase.

It should be noted that the rapid ionization of the medium, induces strongly time dependent refractive indices imparting a strong chirp to the propagating harmonics. [41] furthermore, during the pulse evolution, the laser chirp structure is modified by self-phase modulation. This phenomenon forces the initial negative chirped pulse to be transformed into a positive chirped one. [44]

In general, we can consider the short trajectories to be the correct position of the harmonic for each corresponding chirp. That's because they are almost immune to the effects of intensity variations, although they experience some limited blue shifting effects. On the other hand, the long trajectories display strong phase variations with intensity, translating into a blue shift. This phenomenon is evident from eq.52 and eq.53 that clearly show the strong relation of phase with intensity (with al>>as is evident that the long trajectory is more sensitive to the phase). [41] [47]

The spectral shifting of the harmonics can be described by equation: [41]

$$\Delta\omega = -2\alpha \frac{t}{T^2} e^{-(\frac{t}{T})^2} \quad \text{, with a=}\{^{a_l}_{a_s} \tag{54}$$

Where $\Delta\omega$ is the spectral shifting, a_s and a_l correspond to the short and long trajectory respectively, and T is the pulse duration. Eq.55 demonstrates the relation of frequency shift to the wavelength shift of the plots:

$$\Delta\omega = \frac{2\pi}{\Delta\lambda} \tag{55}$$

So, when the harmonics are generated near or at the peak t=0, thus the shifting is zero regardless of the trajectory and this is the reason precisely that we have selected the harmonics for those chirps, specifically the -150 as the non-shifted one. This argument is also supported by the fact that the apparatus and the propagation effects induce positive chirp, so in order to compensate for this positive chirp we must induce a negative chirp, therefore the real unchirped pulse is for the -150.

Eq. 54 yields different results (different shifts) for the long and short trajectories for high harmonic generation away from the peak in the leading edge of the pulse, which means t<0. As shown in Carlstorm et al. [43] the sign of the a_s for the short trajectory is negative for the 21 and 23 harmonic order, in contrast the sign of a_l is positive. This results to $\Delta\omega>0$ for the long trajectory and $\Delta\omega<0$ for

the short trajectory (by correctly substituting the signs into eq.54). [43] This result into an overall redshift of the short trajectory and a blue shift for the long. [43] [41] finally from the values of the parameters a_s and a_l, as they are demonstrated in the fig.47 we deduce the spectral shifting will be greater for the same chirp but different harmonic order for the long trajectory and less for the short trajectory. ($\Delta\omega_{l23}>\Delta\omega_{l21}$, $\Delta\omega_{s23}<\Delta\omega_{s21}$). [41] [43]

q	11	13	15	17	19	21	23	25	27	29	31	33	35	37
$\alpha_s/(10^{-14}\ \mathrm{cm^2\ W^{-1}})$	−10	−11	−10	−10	−10	−9	−7	−5	5	15	15	18	20	24
$\alpha_l/(10^{-14}\ \mathrm{cm^2\ W^{-1}})$	50	50	51	50	43	43	40	38	35	35	33	31	28	24
n	6	8	7	7	6	6	6	6	7	10	10	11	14	17
$C_l^2 : C_s^2$	2	2	100	100	100	100	100	100	100	100	100	30	50	5

Figure 47 : in this we see different parameters for the calculation of the shift, such a_l a_s, as are calculated by carlstorm et al

The following equations mathematically describes the effects of the SPM from neutral atoms (Kerr effect) and the SPM from the plasma on the laser frequency:

$$\omega(t) = \omega_0 - \frac{n_2\omega_0 L}{c}\frac{dI(t)}{dt} + \frac{\omega_0 L}{2n_0\rho_c}\frac{d\rho(r,t)}{dt} \tag{56}$$

Where $\omega(t)$ is the laser frequency, n_2 is the nonlinear refractive index, c is the speed of light, L is the propagation length, $\rho(r,t)$ is the plasma density and ρ_c is the critical plasma density.

I(t) is given by the equation:

$$I(t) = I_0(\tau)e^{-\frac{4\ln 2\, t^2}{\tau^2}} \tag{57}$$

Where, $I_0(\tau) = I_0\frac{\tau_{FTL}}{\tau}$) is the peak intensity of the chirped pulse with FWHM duration τ.

Clearly, eq.56 shows that the SPM induced by the neutral atoms induces a redshift to the laser beam. Moreover, the SPM induced by the plasma density creates a blueshift to the laser beam. This SPM induced by the plasma density is generally larger than the Kerr effect induced SPM. This result to the blue shifting of the HHG due to propagation inside the plasma.

Finally, plots of the wavelength difference as a function of chirp parameter, were created in origin lab computer program. In these plots a comparison of the effects of the propagation and single atom response on the short and long trajectories was done.

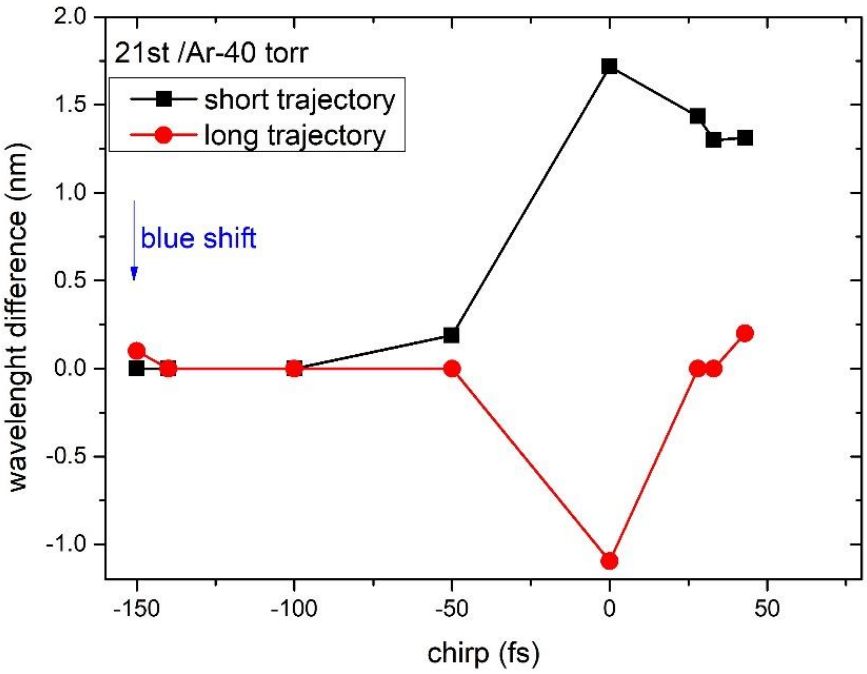

Figure 48: comparison of the effects of the chirp parameter on the long and short trajectory, for the 21st harmonic and for 40 torr Ar gas. It is evident that the long trajectory is affected the least from the chirped pulses. Although a sharp blue shift for the unchirped pulse is observed. The short trajectory, is greatly redshifted for the positive chirped pulses, although it remains unaffected for the corresponding negative values. The unchirped pulse induces the largest redshift to the short trajectory. The different effects of the chirped pulses on the trajectories, lead to their splitting as it is evident from the data.

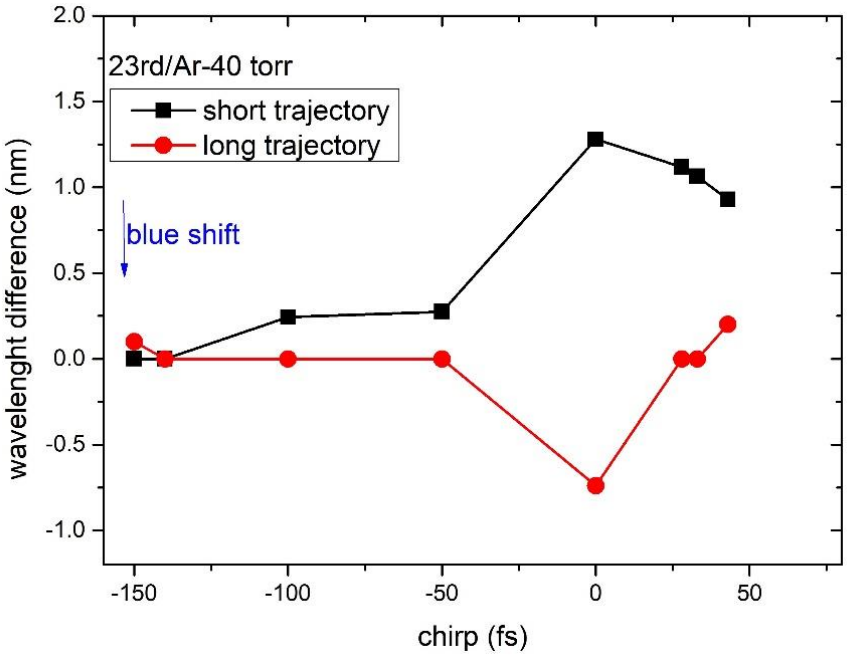

Figure 49: comparison of the effects of the chirp parameter on the long and short trajectory, for the 23rd harmonic and for 40 torr Ar gas. It is evident that the long trajectory is affected the least from the chirped pulses. Although a sharp blue shift for the unchirped pulse is observed. The short trajectory, is greatly redshifted for the positive chirped pulses, although it remains unaffected for the corresponding negative values. The unchirped pulse induces the largest redshift to the short trajectory. The different effects of the chirped pulses on the trajectories, lead to their splitting as it is evident from the data.

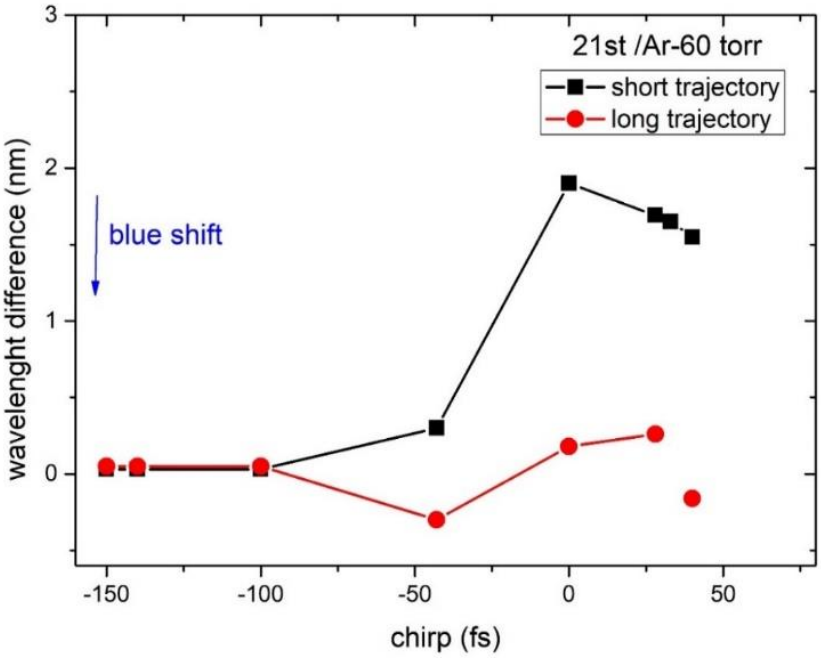

Figure 50: comparison of the effects of the chirp parameter on the long and short trajectory, for the 21st harmonic and for 60 torr Ar gas. It is evident that the long trajectory is affected the least from the chirped pulses. Although a sharp blue shift, in comparison to the other chirped pulses, for the -50 fs chirped pulse is observed. The short trajectory, is greatly redshifted for the positive chirped pulses, although it remains unaffected for the corresponding negative values. The unchirped pulse induces the largest redshift to the short trajectory. The different effects of the chirped pulses on the trajectories, lead to their splitting as it is evident from the data. Finally, the value of the wavelength difference for the 43 fs chirped pulse is probably incorrect due to signal absorption processes, which are difficult to be calculated.

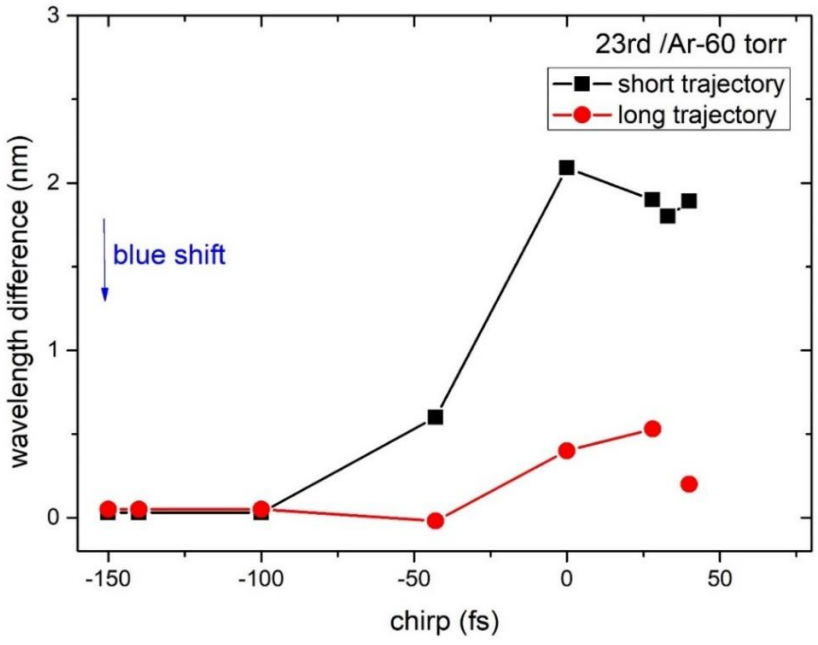

Figure 51: comparison of the effects of the chirp parameter on the long and short trajectory, for the 23rd harmonic and for 60 torr Ar gas. It is evident that the long trajectory is affected the least from the chirped pulses. Although a blue shift, in comparison to the other chirped pulses, for the -50 fs chirped pulse is observed. Additionally, a small redshift at the long trajectory is observed for positive values. The short trajectory, is greatly redshifted for the positive chirped pulses, although it remains unaffected for the corresponding negative values. The unchirped pulse induces the largest redshift to the short trajectory. The different effects of the chirped pulses on the trajectories, lead to their splitting as it is evident from the data. Finally, the value of the wavelength difference for the 43 fs chirped pulse is probably incorrect due to signal absorption processes, which are difficult to be calculated.

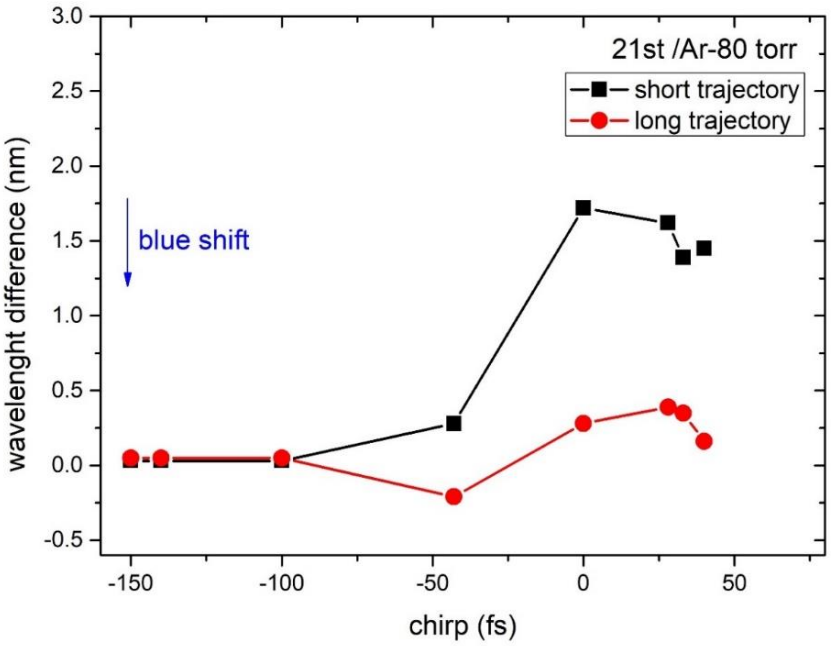

Figure 52: comparison of the effects of the chirp parameter on the long and short trajectory, for the 21st harmonic and for 80 torr Ar gas. It is evident that the long trajectory is affected the least from the chirped pulses. Although a blue shift, in comparison to the other chirped pulses, for the -50 fs chirped pulse is observed. Additionally, a small redshift at the long trajectory is observed for positive values. The short trajectory, is greatly redshifted for the positive chirped pulses, although it remains unaffected for the corresponding negative values. The unchirped pulse induces the largest redshift to the short trajectory. The different effects of the chirped pulses on the trajectories, lead to their splitting as it is evident from the data.

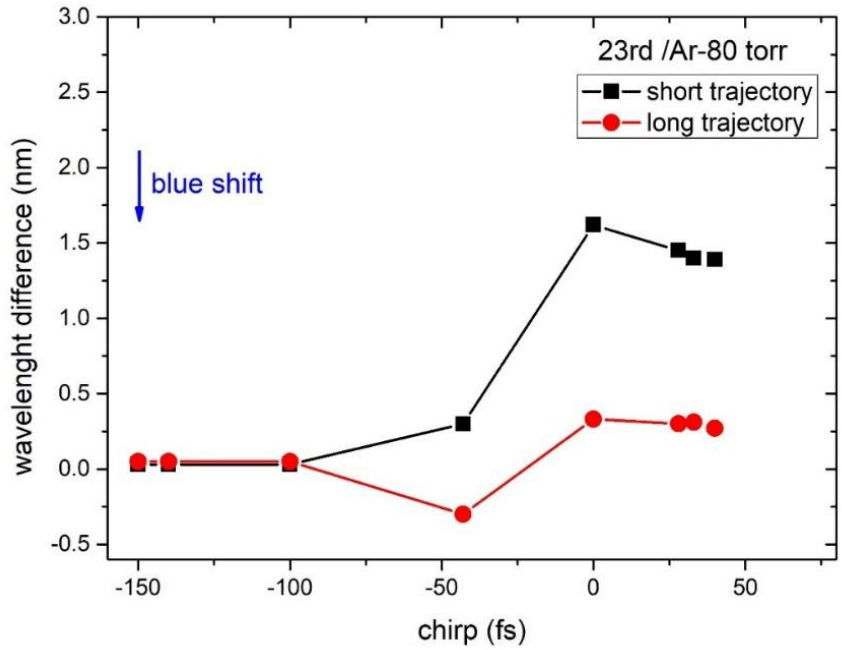

Figure 53 : comparison of the effects of the chirp parameter on the long and short trajectory, for the 23rd harmonic and for 80 torr Ar gas. It is evident that the long trajectory is affected the least from the chirped pulses. Although a blue shift, in comparison to the other chirped pulses, for the -50 fs chirped pulse is observed. Additionally, a small redshift at the long trajectory is observed for positive values. The short trajectory, is greatly redshifted for the positive chirped pulses, although it remains unaffected for the corresponding negative values. The unchirped pulse induces the largest redshift to the short trajectory. The different effects of the chirped pulses on the trajectories, lead to their splitting as it is evident from the data.

For the high negative chirp parameters (-150, -140, -100 fs) a very small splitting (or no splitting), between short and long trajectory HHG, is observed. For FTL pulses and positive chirp clear splitting is observed for all pressure range, which is maximized for zero chirp

Long trajectory HHG is observed to be blue shifted in comparison with short trajectory HHG, which is redshifted relative to the expected spectral position of each harmonic (which is the position of -150 fs because very low intensity and plasma creation)

For the -150, -140 and -100 chirp, the density of plasma is very low. Moreover, the pulse is highly chirped and the laser intensity is low, therefore high harmonic generation takes place at the peak of the pulse or at least very near of, thus we observe a very small or even zero harmonic splitting.

For the small positive chirp values of +28, +33, +43 fs, the whole harmonic gets an overall redshift, because of the generation of high harmonics in the leading edge of the pulse, where the red frequencies dominate, this redshift greatly affects the short trajectory as it is observed on the graphs, although both trajectories should be redshifted, as a result of High harmonic generation from red frequencies. Furthermore, eq.54 and eq. 56 yields a blue shift, which is more greatly experienced by the long trajectory. Therefore, this redshift affecting the short trajectory and blueshift affecting the long trajectory result in the harmonic splitting observed in our data. It should be noted that for the +33-value quantum phase interference result in the completely loss of the long trajectory. [41] [43] [44]

For the 0 chirp, the pulse intensity is expected to be maximum, therefore plasma density is should be maximum. This would maximize the effect of the propagation of the beam inside the plasma. This propagation induces a large SPM, which blue shifts the long trajectory (due to its sensibility to propagation effects and on the peak intensity). It should be noted that the short trajectory appears to be redshifted due to the fact that the SPM (from the kerr effect) induced a small positive chirp to the pulse (which also lowers the intensity and the plasma density, reducing the blue shift of the pulse) and therefore the generated harmonics are redshifted (as they are born from the red frequencies in the leading edge of the pulse) Thus, harmonic splitting is observed. *[41] [43] [44]*

Generally, as the values of the chirp turn to negative an overall blue shift is expected, due to the domination of blue frequencies in the leading edge of the pulse.

For the -50 fs chirp we observe that the whole harmonic gets redshifted, this is due to the fact that the propagation of laser field leads to the transformation of the initial negative chirp into positive chirp, due to SPM effects from neutral atoms (see Fig 53 calculation by Kim et al) [44]. This results into an overall redshift which manifest each self only to the short trajectory, because the long trajectory gets blue shifted as shown in eq.54 and eq.56.This difference in shifting leads to the splitting of the harmonic, as shown in the graphs. [41] [43] [44]

Getting to more negative values the blue shift induced by the distribution of frequencies begins to affect the splitting patterns, by powerfully compensating the SPM effects, therefore the nominal position of the harmonic is blue shifted. Thus, no splitting is observed.

The effects of the SPM on the distribution of frequencies in the pulse, is clearly shown in fig.53. where it is demonstrated that an initially negatively chirped pulse is transformed into a positively chirped one due to propagation effects.

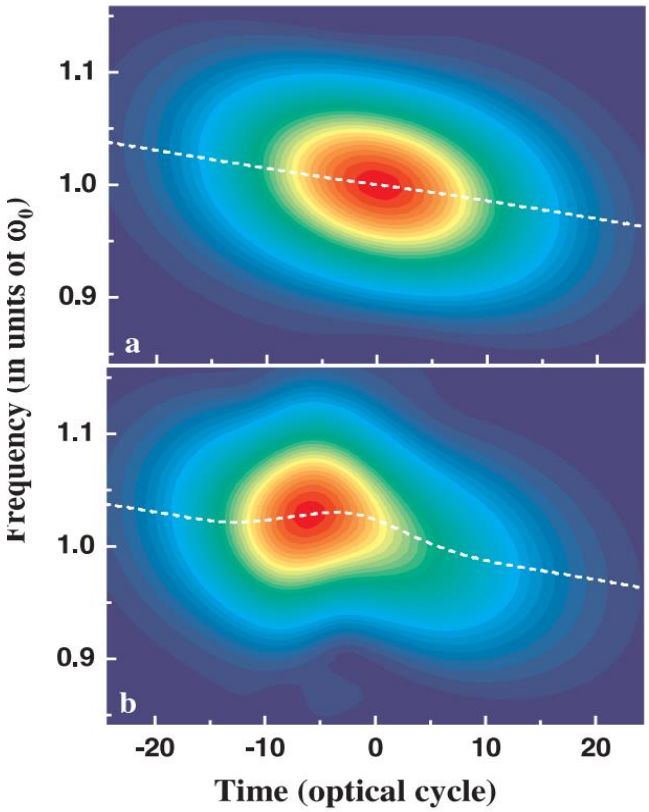

Figure 53: change of the chirp structure under the effects of the propagation of initially negatively chirped laser pulse [44], Kim et al.

Plasma density is maximum, for the -50 fs pulse, but greater splitting is observed for the FTL pulse. This phenomenon is explained by the fact that the -50 fs is generated from the blue frequencies in the leading edge of the pulse, therefore the positive chirp induced from the SPM (from the Kerr effect) is somewhat compensated, although the blue shift experienced by the long trajectory is maximum (as expected from its sensibility to intensity).

Summing up, the spectral position of HHG from the short and long trajectory can be mathematically, estimated by the equation:

$$\omega_{s,l}^{q} = q\omega(t = generation\ time) - 2\alpha_{s,l}\ \frac{t}{T^2} e^{-(\frac{t}{T})^2} \quad t < 0\ for HHG \tag{58}$$

Finally, it should be noted that when harmonic splitting is observed, tends to be more pronounced as we increase the harmonic order, additionally pressure does not seem to affect the splitting patterns.

The obtained experimental results and the theoretical analysis clearly show that the insertion of chirp to the laser pulses is a crucial procedure for the control of the electron quantum paths in the HHG from atomic gases. As a consequence, this control affects the HHG spectra, by separating the short and long trajectories and under favourable circumstances, may allow a selective suppression of one of them.

4.3 DIVERGENCE OF LONG AND SHORT TRAJECTORIES

In the final chapter of our data analysis we will discuss the divergence of the high harmonic radiation generated by the separated electron trajectories.

The origin of divergence in HHG has been understood to be the corresponding radial variation of the laser field intensity I(r), which introduces a curvature to the phase front which, for large intensities such as those involved in the generation of high harmonics, will make the beam strongly divergent. [4] [50] [51] This divergence of the beam leads to the divergence of the harmonic field, because the curvature of the harmonic field is equal to that of the fundamental plus that induced by the dipole phase [52] . The divergence of each trajectory is expected to be different, because of the different sources of those quantum paths, corresponding to the short and long trajectories and because of the different quantity of phase that each trajectory accumulates (with the long accumulating more). Those quantum paths correspond to same photon energies. [51] The main distinction between the two trajectories in each harmonic is the difference between their divergence. The long trajectory has a larger divergence than the short, due to the fact that the electron travels longer distances in the ionised medium [52].

We measured the divergence by measuring the width of the harmonic and then and we calibrated with the correct pixel to mrad ratio, thus creating plots of HH divergence as a function of laser chirp (fig.58, fig.59, fig.60, fig.61). Divergence is related to the distance from the harmonic generation spot (L) and the width of the harmonic on the xuv camera (y) via the relation:

$$\theta(\text{mrad}) = \frac{y}{L} \tag{59}$$

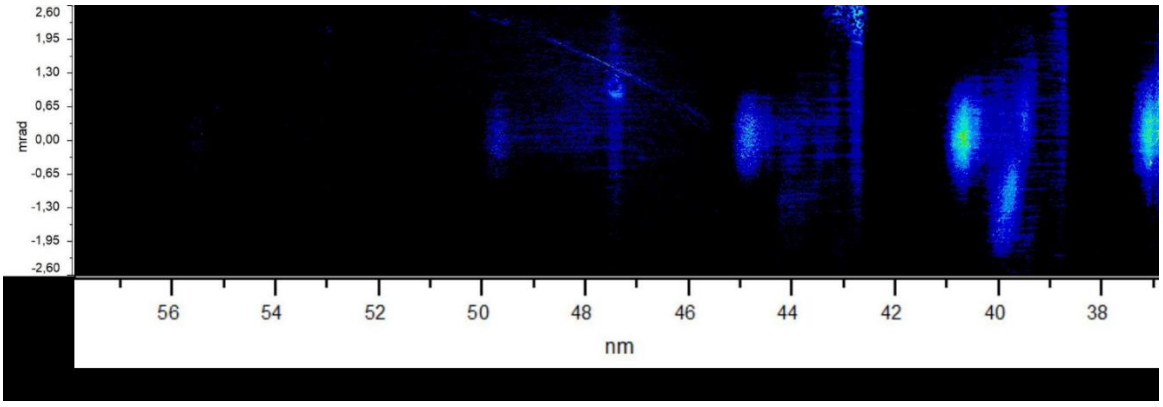

Figure 55: calibration of the image in order to calculate the divergence in the correct manner.

We created graphs for the 21st and 23rd harmonic for40, 60 and 80 torr Argon. In those graphs only the corresponding divergence to the chirp values of -50,0,28,43 fs was determined, because for the -150, -140 and -100 fs chirp values, we cannot distinguish the difference of the divergence of the short and long trajectories because it gets spectrally overlapped due to the low density of plasma and the resulting absence of splitting.

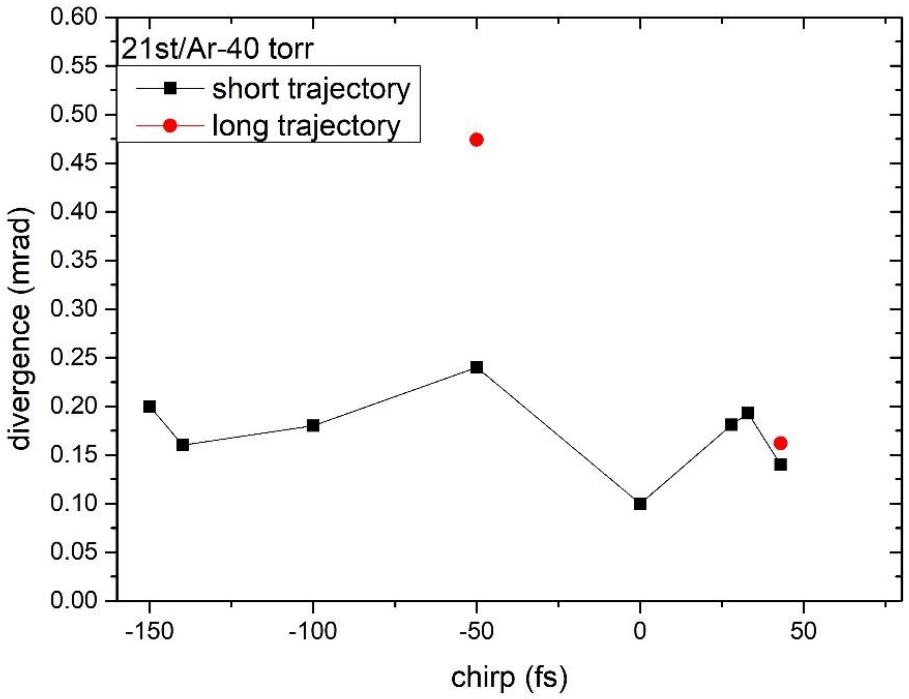

Figure 56: a comparison of the effects of the chirp parameter on the divergence of each of the long and short trajectory for the 21st harmonic and for 40 torr Ar gas. The short trajectory is the least affected by chirped pulses, although a small o variation of each value is observed. The long trajectory most of the time is not observed, due to destructive interference phenomena, which lead to bad phase matching and the loss of the trajectory. Although, the values for -50 fs and for 43 fs chirped pulse allows us to observe a sharp divergence of the long trajectory.

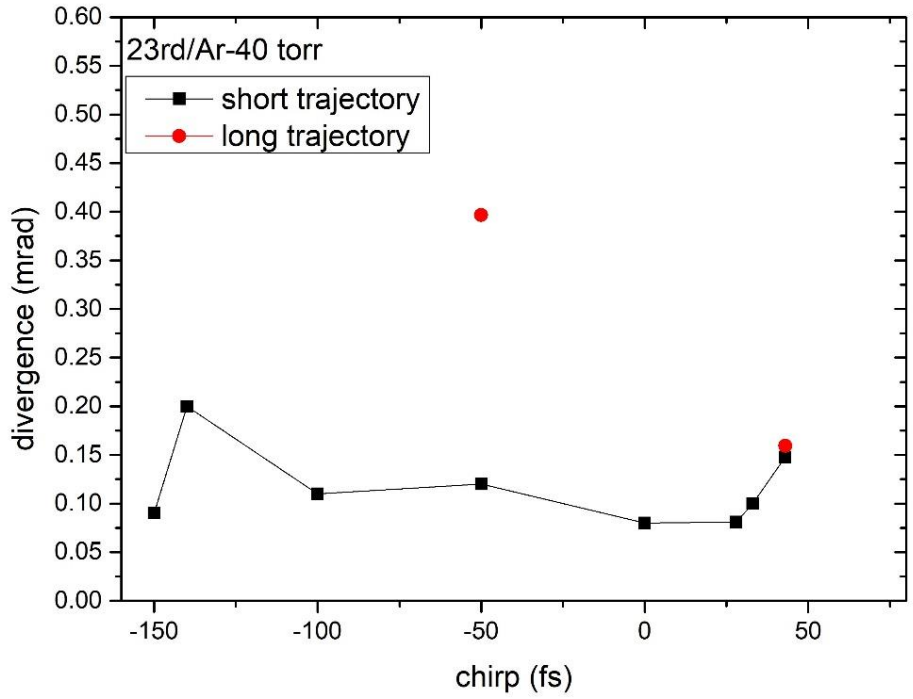

Figure 57: a comparison of the effects of the chirp parameter on the divergence of each of the long and short trajectory for the 23rd harmonic and for 40 torr Ar gas. The short trajectory is the least affected by chirped pulses, although a small o variation of each value is observed. The long trajectory most of the time is not observed, due to destructive interference phenomena, which lead to bad phase matching and the loss of the trajectory. Although, the values for -50 fs and for 43 fs chirped pulse allows us to observe a sharp divergence of the long trajectory.

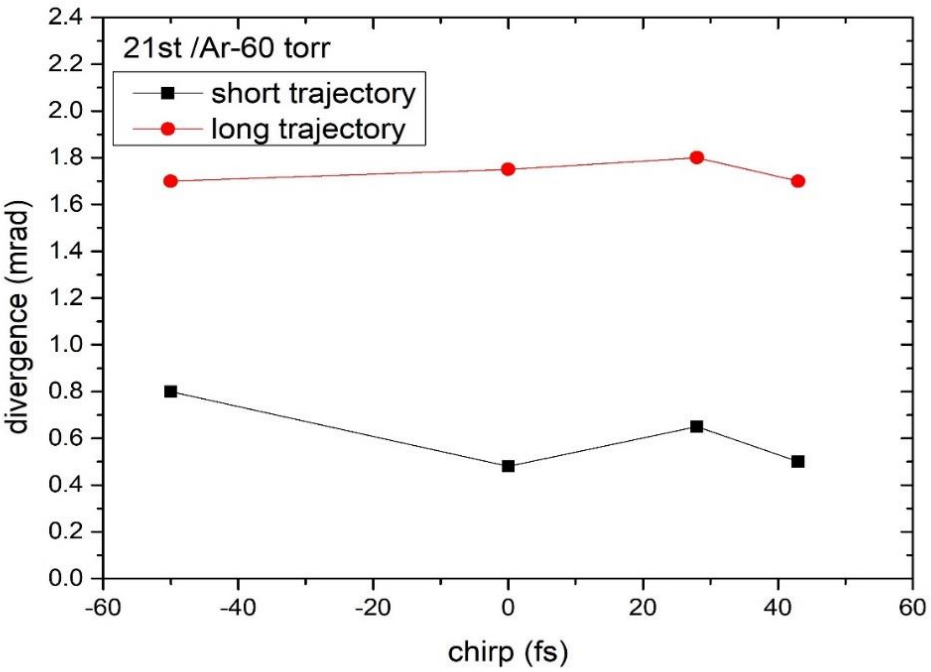

Figure 58: a comparison of the effects of the chirp parameter on the divergence of each of the long and short trajectory for the 21st harmonic and for 60 torr Ar gas. The short trajectory is the least affected by chirped pulses, although a small o variation of the value of its divergence is observed. The long trajectory is greatly affected by the chirped values and evidently has the largest divergence.

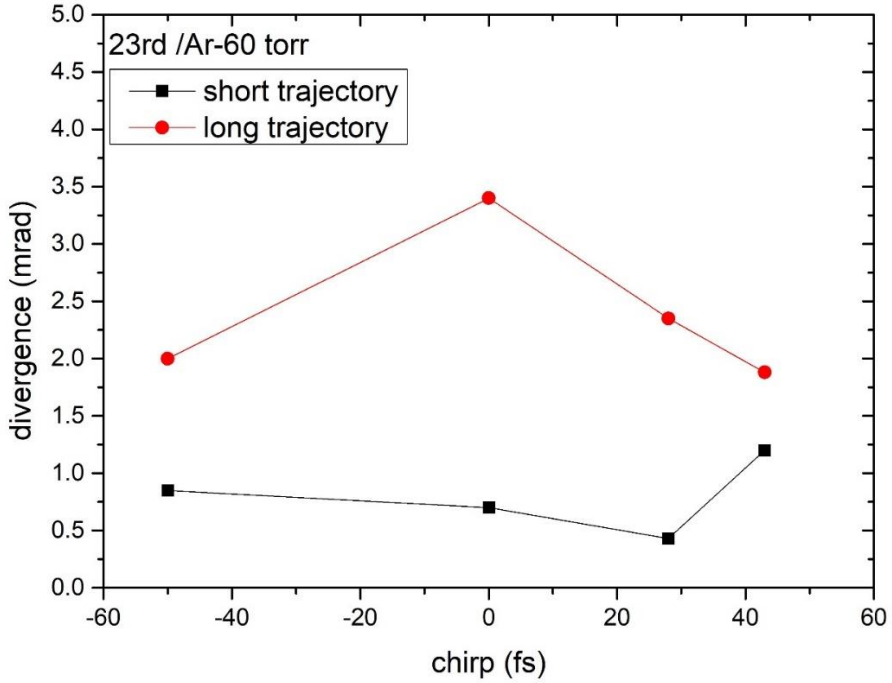

Figure 59: a comparison of the effects of the chirp parameter on the divergence of each of the long and short trajectory for the 23rd harmonic and for 60 torr Ar gas. The short trajectory is the least affected by chirped pulses, although a small o variation of the value of its divergence is observed. The long trajectory is greatly affected by the chirped values and evidently has the largest divergence, with the largest one observed for the unchirped pulse. Finally, we observe a rapid coalescence of the divergence of the short and long trajectory as we increase the value of the positive chirp.

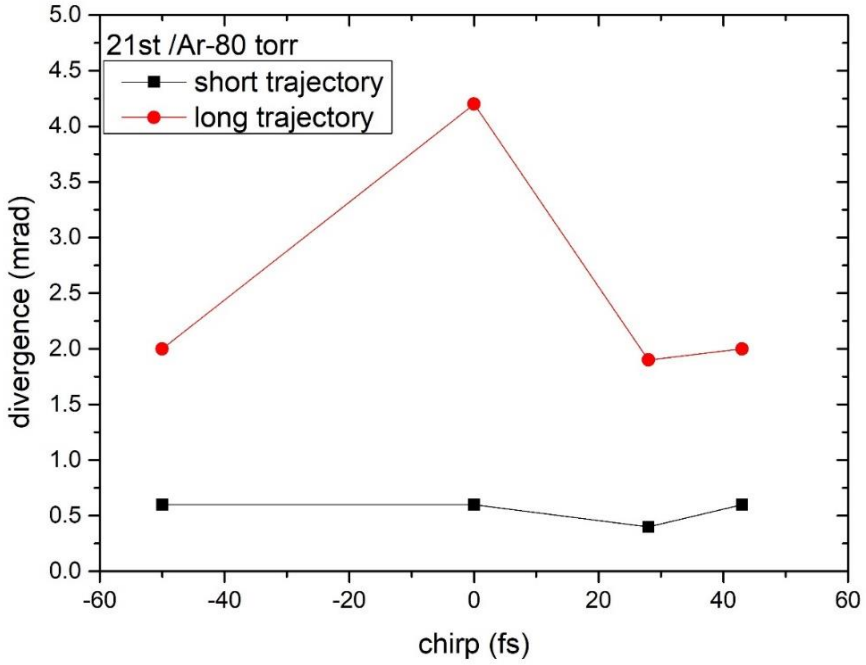

Figure 60: a comparison of the effects of the chirp parameter on the divergence of each of the long and short trajectory for the 21st harmonic and for 80 torr Ar gas. The short trajectory is the least affected by chirped pulses, although a small o variation of the value of its divergence is observed. The long trajectory is greatly affected by the chirped values and evidently has the largest divergence. Finally, a rapid increase of the divergence of the long trajectory, as we decrease the value of the negative chirp is observed. For an increasing positive value of the chirp parameter the divergence (which decreases sharply from the highest value it had at zero chirp) is less sharp and somewhat stabilized.

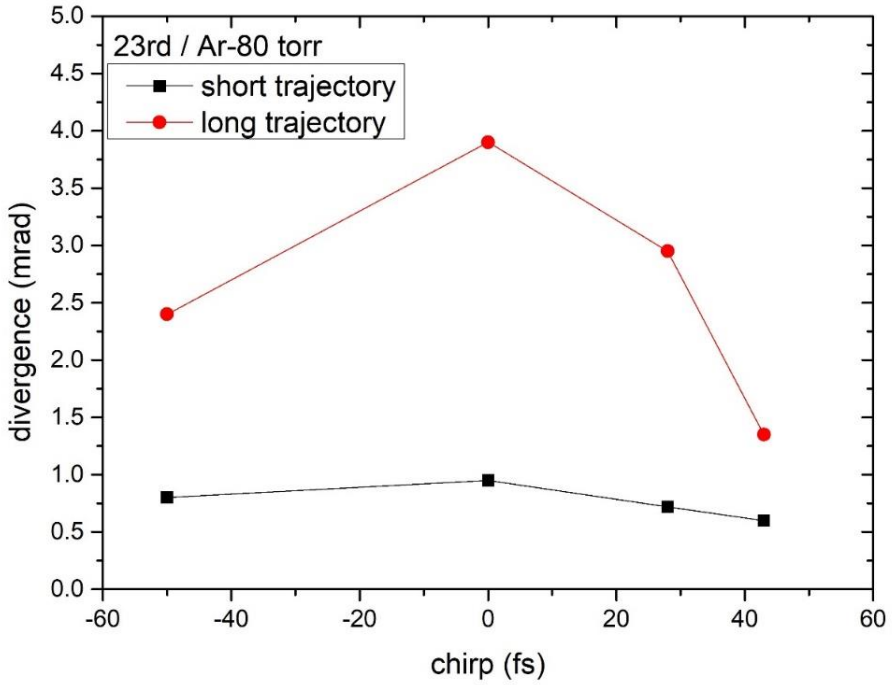

Figure 61: a comparison of the effects of the chirp parameter on the divergence of each of the long and short trajectory for the 23rd harmonic and for 80 torr Ar gas. The short trajectory is the least affected by chirped pulses, although a small o variation of the value of its divergence is observed. The long trajectory is greatly affected by the chirped values and evidently has the largest divergence. A rapid decrease of the value of divergence from its highest value (at zero chirp) is observed for increasing positive chirp values.

From the figures 56,57,58,59 we observe that the long trajectory manifests greater divergence than the short trajectory, confirming the theoretical predictions. This holds true for the whole pressures range, as well as for both harmonic orders. Although an increase in the pressure leads to a small increase in the divergence of the long trajectory, as the denser plasma magnifies the accumulated phase of both trajectories, which leads to an intensification of the effects of the propagation and therefore to a larger divergence for the long trajectory.

For the 40 torr we observe a clear lower magnitude for the divergence of both trajectories and for both harmonic orders, as it is expected by the fact that for the lower pressure, the corresponding plasma density is low. Therefore, the accumulated from, the propagation phase, is consequently lower for both trajectories.

Additionally, the phase each trajectory accumulates is also dependant on the intensity (eq.54), the larger the intensity is, the larger the phase becomes magnifying the effects of the propagation and consequently increasing the divergence different between the two trajectories. Consequently, the divergence of both trajectories is larger for the unchirped pulse and especially for the long trajectory is maximum. This statement is supported by the experimental observation, that the peak divergent difference manifests for the unchirped pulse. Finally, it is observed that the sign of the chirp values does not play a role in the

Finally, it is evident that we have greater divergence for the highest order harmonic for both pressure because of the greater dipole phase the higher harmonic accumulates, which is mostly evident in the long trajectory, which is greatly affected from the dipole phase, for having the longest interaction time with the electromagnetic field. [51] [43]

4. CONCLUSIONS

In this thesis, we examined the effects of different chirp values and signs to the splitting of the harmonics and its relation to the divergence of the long and short trajectory. This examination was done by utilizing the properties of noble gases, such as argon to generate efficiently high harmonic radiation. Our apparatus, centered around a gas jet, gave us the opportunity το control the chirp values we were interested in through the grating system inside the compressor. Therefore, we proved, that the splitting patterns were consistent with the expected ones. We showed the dependence of the splitting patterns on the density of plasma and the effects of the propagation phenomena, such as SPM on the intensity of the beam. A study of the plasma density from its luminescence, as well as a comprehensive report of the dependence of the intensity profile to the pulse width (which is dependent on the chirp value) was done, in order to support the previous findings. Hence, we were able to show that the propagation effects, induced positive chirp in the pulse, and the plasma density as well as the atomic response lead to the redshift of the pulse. The different magnitudes, all those phenomena affected each trajectory lead to the aforementioned splitting. We also observed different interference patterns, which were generated by the fact that each trajectory was affected in a different way by the intensity profile and the plasma density, leading to different divergence patterns for each one of them. Finally, by correctly correlating each divergence pattern to the correct emission mechanism, we can show why each trajectory is affected the way it is. Thus, by alternating the values of chirp we are able to spectrally control the shift of both the long and short trajectories and in some circumstances by utilizing the interference patterns exhibit by the different quantum paths we are able to vanish the long trajectory.

In the future, by utilizing this efficient control of the spectral shift and its interference patterns, we will be able to efficiently select and efficiently tune and enhance a specific harmonic, this could be done by improving our understanding on the quantum phenomena affecting the generation of high harmonic radiation and its propagation through dense plasma. Improved control of the mechanism of emission of each harmonic trajectory and its relation to the interference patterns will allow us to selectively vanish or enhance a specific harmonic. Additionally, the necessity to efficiently control the plasma production and therefore its density, generates the need to further our knowledge on the mechanisms of atomic ionization and the mechanisms of field atom interactions. These studies can lead us to better understand the physics of radiation matter interactions and lead to new findings in big spectrum of physics, such us atomic physics and plasma physics. Finally, it should be noted that the efficient control of plasma leads us to better understand its instabilities, therefore we can create better ways to acquire stable plasma, thus generate new technologies, which are very important for the applications of plasma, such us nuclear fusion, in the same way the need for a coherent control of the laser beam profile, in the hall duration of our study, may lead to further advances in the control and enhancement of a laser beam and lead to great advances in the corresponding technology. This technology with its innumerable applications, not only in physics but also in medicine can be greatly improved by those aforementioned advances.

5. BIBLIOGRAPHY

1. Aaron von Conta, An Introduction to High-Harmonic Generation: Towards High-Harmonic Spectroscopy, Physical Chemistry V, 10 April 2013

2. Krause, Jeffrey L., Kenneth J. Schafer, and Kenneth C. Kulander. “High-Order Harmonic Generation from Atoms and Ions in the High Intensity Regime.” Physical Review Letters 68, no. 24 (1992): 3535–38. https://doi.org/10.1103/physrevlett.68.3535.

3. https://ufox.cfel.de/sites/sites_cfelgroups/site_cfel-ufox/content/e16281/e86791/e86828/e86829/e86835/UFSIMPRS_HHGsection.pdf

4. Lewenstein, M., Ph. Balcou, M. Yu. Ivanov, Anne L’Huillier, and P. B. Corkum. “Theory of High-Harmonic Generation by Low-Frequency Laser Fields.” Physical Review A 49, no. 3 (1994): 2117–32. https://doi.org/10.1103/physreva.49.2117.

5. N. Papadogiannis lectures on laser matter interaction, Msc, department of electronic engineering H.M.U.), chapter 1.

6. https://en.wikipedia.org/wiki/Quasistatic_approximation

7. Ammosov, M. V., V. P. Krainov, V. M. Ristic, P. A. Golovinsky, and I. Yu. Kiyan. “Tunneling Ionization of Atoms and Atomic Ions in an Intense Laser Field with a Nonhomogeneous Space–Time Distribution.” Journal of the Optical Society of America B 9, no. 8 (1992): 1225. https://doi.org/10.1364/josab.9.001225.

8. Dachraoui, H, T Auguste, A Helmstedt, P Bartz, M Michelswirth, N Mueller, W Pfeiffer, P Salieres, and U Heinzmann. “Interplay between Absorption, Dispersion and Refraction in High-Order Harmonic Generation.” Journal of Physics B: Atomic, Molecular and Optical Physics 42, no. 17 (2009): 175402. https://doi.org/10.1088/0953-4075/42/17/175402.

9. Pfeifer, T, C Spielmann, and G Gerber. “Femtosecond x-Ray Science.” Reports on Progress in Physics 69, no. 2 (2006): 443–505. https://doi.org/10.1088/0034-4885/69/2/r04.

10. https://www.rp-photonics.com/gouy_phase_shift.html

11. Cheng jin, theory of nonlinear propagation in HHG in gaseous medium, springer

12. https://www.rp-photonics.com/phase_matching.html

13. Tenio Popmintcheva, Ming-Chang Chena, Alon Bahabada, Michael Gerritya, Pavel Sidorenkob, Oren Cohenb, Ivan P. Christovc, Margaret M. Murnanea,1, and Henry C. Kapteyn, PNAS, vol. 106, no. 26, 10521, (June 30, 2009)

14. Francis E Chen, introduction to plasma physics and controlled fusion, second edition, Volume 1: Plasma Physics

15. [14]W. L. a. A. P. H.J. LEHMEIER, "NONRESONANT THIRD ORDER HYPERPOLARIZABILITY OF RARE GASES AND N 2 DETERMINED BY THIRD HARMONIC GENERATION," *OPTICS COMMUNICATIONS Volume 56, number 1,* 1985

16. Balogh, Emeric, and Katalin Varjú. “Field Strength Scaling in Quasi-Phase-Matching of High-Order Harmonic Generation by Low-Intensity Assisting Fields.” Journal of the Optical Society of America B 33, no. 2 (2016): 230. https://doi.org/10.1364/josab.33.000230.

17. https://en.wikipedia.org/wiki/Kerr_effect

18. https://en.wikipedia.org/wiki/Self-phase_modulation

19. https://www.rp-photonics.com/self_phase_modulation.html

20. https://en.wikipedia.org/wiki/Ultrashort_pulse

21. strong field laser physics, springer

22. https://www.rp-photonics.com/chirp.html

23. p. maine, d. strickland, p. bado, m. pessot, a n d g . mourou, Generation of Ultrahigh Peak Power Pulses by Chirped Pulse Amplification, journal of quantum electronics, VOL. 24. NO. 2 , (FEBRUARY 1088)

24. P.Gibbon, short pulse laser interactions with matter, imperial college press, 57 Shelton Street.

25. French, P M. "The Generation of Ultrashort Laser Pulses." Reports on Progress in Physics 58, no. 2 (1995): 169–262. https://doi.org/10.1088/0034-4885/58/2/001.

26. https://www.rp-photonics.com/autocorrelators.html

27. J. Zhou, J. Peatross, M. M. Murnane, and H. C. Kapteyn, Enhanced High-Harmonic Generation Using 25 fs Laser Pulses, p h y s i c a l r e v i e w l e t t e r s, volume 76, number 5, (29 january 1996)

28. Chang, Z., A. Rundquist, H. Wang, I. Christov, H. C. Kapteyn, and M. M. Murnane. "Temporal Phase Control of Soft-x-Ray Harmonic Emission." Physical Review A 58, no. 1 (1998). https://doi.org/10.1103/physreva.58.r30.

29. Kim, Hyung Taek, Dong Gun Lee, Kyung-Han Hong, Jung-Hoon Kim, Il Woo Choi, and Chang Hee Nam. "Continuously Tunable High-Order Harmonics from Atoms in an Intense Femtosecond Laser Field." Physical Review A 67, no. 5 (2003). https://doi.org/10.1103/physreva.67.051801.

30. Kim, H.T., I.J. Kim, V. Tosa, Y.S. Lee, and C.H. Nam. "High Brightness Harmonic Generation at 13 Nm Using Self-Guided and Chirped Femtosecond Laser Pulses." Applied Physics B: Lasers and Optics 78, no. 7-8 (2004): 863–67. https://doi.org/10.1007/s00340-004-1456-z.

31. Tosa, V., H. T. Kim, I. J. Kim, and C. H. Nam. "High-Order Harmonic Generation by Chirped and Self-Guided Femtosecond Laser Pulses. II. Time-Frequency Analysis." Physical Review A 71, no. 6 (2005). https://doi.org/10.1103/physreva.71.063808.

32. Rashid A. Ganeev, Single-harmonic enhancement by controlling the chirp of the driving laser pulse during high-order harmonic generation from GaAs plasma, Vol. 23, No. 12, 2535, (December 2006)

33. Katalin Kova, Emeric Balogh, Janos Hebling, Valer Tosa and Katalin Varju, PRL 108, 193903 (11 MAY 2012)

34. Wang, Xu, Cheng Jin, and C. D. Lin. "Coherent Control of High-Harmonic Generation Using Waveform-Synthesized Chirped Laser Fields." Physical Review A 90, no. 2 (2014). https://doi.org/10.1103/physreva.90.023416.

35. American optical society 2004 J. R. Sutherland, E. L. Christensen, N. D. Powers, S. E. Rhynard, J. C. Painter and J. Peatross

36. Daniel S. Steingrube, Phase matching of high-order harmonics in a semi-infinite gas cell, PHYSICAL REVIEW A 80, 043819 (2009).

37. Journal of Nonlinear Optical Physics & Materials Vol. 24, No. 3, 1550031, (2015).

38. https://en.wikipedia.org/wiki/Faraday_rotator

39. JOSEPH LADISLAS WIZA, MICROCHANNEL PLATE DETECTORS, Vol. 162

40. Yakovlev, Vladislav S., and Armin Scrinzi. "High Harmonic Imaging of Few-Cycle Laser Pulses." Physical Review Letters 91, no. 15 (2003). https://doi.org/10.1103/physrevlett.91.153901.

41. Papadogiannis, N.A., C. Kalpouzos, E. Goulielmakis, G. Nersisyan, D. Charalambidis, F. Augé, F. Weihe, and Ph. Balcou. "Kilohertz Extreme-Ultraviolet Light Source Based on Femtosecond High-Order Harmonic Generation from Noble Gases." Applied Physics B: Lasers and Optics 73, no. 7 (2001): 687–92. https://doi.org/10.1007/s003400100734.

42. C.-G. Wahlstrom, J. Larsson, A. Persson, T. Starczewski, and S. Svanberg physical review a, volume 48, number (6 december 1993)

43. Carlström, Stefanos, Jana Preclíková, Eleonora Lorek, Esben Witting Larsen, Christoph M Heyl, David Paleček, Donatas Zigmantas, Kenneth J Schafer, Mette B Gaarde, and Johan Mauritsson. "Spatially and Spectrally Resolved Quantum Path Interference with Chirped Driving Pulses." New Journal of Physics 18, no. 12 (2016): 123032. https://doi.org/10.1088/1367-2630/aa511f.

44. Kim, H.T., I.J. Kim, V. Tosa, Y.S. Lee, and C.H. Nam. "High Brightness Harmonic Generation at 13 Nm Using Self-Guided and Chirped Femtosecond Laser Pulses." Applied Physics B: Lasers and Optics 78, no. 7-8 (2004): 863–67. https://doi.org/10.1007/s00340-004-1456-z.

45. Salieres, P. "Feynman's Path-Integral Approach for Intense-Laser-Atom Interactions." Science 292, no. 5518 (2001): 902–5. https://doi.org/10.1126/science.108836.

46. Antoine, Philippe, Anne L'Huillier, and Maciej Lewenstein. "Attosecond Pulse Trains Using High–Order Harmonics." Physical Review Letters 77, no. 7 (1996): 1234–37. https://doi.org/10.1103/physrevlett.77.1234.

47. Kim, Jung-Hoon, Hyun Joon Shin, Dong Gun Lee, and Chang Hee Nam. "Enhanced Spectral Resolution of High-Order Harmonics by the Coherent Sum of Dipole Spectra." Physical Review A 62, no. 5 (2000). https://doi.org/10.1103/physreva.62.055402.

48. Kan, C., C. E. Capjack, R. Rankin, and N. H. Burnett. "Spectral and Temporal Structure in High Harmonic Emission from Ionizing Atomic Gases." Physical Review A 52, no. 6 (1995). https://doi.org/10.1103/physreva.52.r4336.

49. Hyun Joon Shin, Dong Gun Lee, Yong Ho Cha, Kyung Han Hong, and Chang Hee Nam '' Generation of Nonadiabatic Blueshift of High Harmonics in an Intense Femtosecond Laser Field'' p h y s i c a l r e v i e w l e t t e r S, volume 83, number 13, (27 september 1999).

50. Vuong, Cuong Van, Khuong Ba Dinh, Peter Hannaford, and Lap Van Dao. "Phase-Matched High-Order Harmonic Generation in a Semi-Infinite Gas Cell with Absorbing Gaseous Media."

Journal of Nonlinear Optical Physics & Materials 24, no. 03 (2015): 1550031. https://doi.org/10.1142/s0218863515500319.

51. N. Papadogiannis lectures on laser matter interaction, Msc, department of electronic engineering H.M.U.), chapter 2

52. Petrakis, Stylianos, Makis Bakarezos, Michael Tatarakis, Emmanouil Benis, and Nektarios Papadogiannis. "Electron Quantum Path Control in High Harmonic Generation via Chirp Variation of Strong Laser Pulses," 2021. https://doi.org/10.21203/rs.3.rs-764431/v1.

53. Papadogiannis, N.A., C. Kalpouzos, E. Goulielmakis, G. Nersisyan, D. Charalambidis, F. Augé, F. Weihe, and Ph. Balcou. "Kilohertz Extreme-Ultraviolet Light Source Based on Femtosecond High-Order Harmonic Generation from Noble Gases." *Applied Physics B: Lasers and Optics* 73, no. 7 (2001): 687–92. https://doi.org/10.1007/s003400100734.